Cu-CHA-a model system for applied selective redox catalysis

(Article begins on next page)

02 July 2024

iris-AperTO

University of Turin's Institutional Research Information System and Open Access Institutional Repository

Cu-CHA – A Model system for Applied Selective Redox Catalysis

Elisa Borfecchia,[a,†] Pablo Beato,[*,a] Stian Svelle,[*,b] Unni Olsbye,[b] Carlo Lamberti[c,d] and Silvia Bordiga,[*,b,e]

[a] Haldor Topsøe A/S, Haldor Topsøes Allé 1, 2800 Kongens Lyngby, Denmark. E-mail: PABB@topsoe.com
[b] Center for Materials Science and Nanotechnology (SMN), Department of Chemistry, University of Oslo, P.O. Box 1033 Blindern, N-0315 Oslo, Norway. E-mail: stian.svelle@kjemi.uio.no
[c] The Smart Materials Research Center, Southern Federal University, Sladkova 174/28, 344090 Rostov-on-Don, Russia
[d] Department of Physics, INSTM Reference Center and CrisDi Interdepartmental Centre for Crystallography, University of Turin, Via P. Giuria 1, 10125 Turin Italy
[e] Department of Chemistry, INSTM Reference Center and NIS Interdepartmental Centre, University of Turin, Via Quarello 15, I-10135, Turin, Italy. E-mail: silvia.bordiga@unito.it
[†] Present address: SMN, Department of Chemistry, University of Oslo, P.O. Box 1033 Blindern, N-0315 Oslo, Norway.

We review the structural chemistry and reactivity of copper-exchanged molecular sieves with chabazite (CHA) topology, as industrially applied catalyst in ammonia mediated reduction of harmful nitrogen oxides (NH_3-SCR) and as a general model system for red-ox active materials (also the recent results in the direct conversion of methane to methanol are considered). Notwithstanding the apparent structural simplicity of the material, a crystalline zeolite with only one crystallographically independent T site, the Cu-SSZ-13 catalyst reveals a high degree of complexity that has been decrypted by state of the art characterization tools. From the reviewed data, the following important aspects in the understanding of the Cu-SSZ-13 catalyst clearly emerged: (i) the structural dynamics of the Cu-species require precise control of the environmental conditions during activation and characterization; (ii) the availability of a large library of well-defined catalysts with different Si/Al and Cu/Al compositional ratios is key in unravelling the red-ox property of the active Cu sites; (iii) a multi-technique approach is required, combining complementary techniques able to provide independent structural, electronic and vibrational information; (iv) synchrotron radiation based techniques (EXAFS, XANES, XES and time-resolved powder XRD) played a relevant role; (v) *operando* methodology (possibly supported by advanced chemometric approaches) is essential in obtaining structure-reactivity relations; (vi) the support of theoretical studies has been indispensable for the interpretation of the experimental output from characterization and for a critical assessment of mechanistic models.

The old literature, that classified Cu-exchanged zeolites in the category of *single-site* catalysts, has been partially disproved by the recent advanced studies where it has been shown that the active site in low temperature NH_3-SCR catalyst is a mobile Cu-molecular entity that "lives in symbiosis" with an inorganic solid framework. Only in the high temperature NH_3-SCR regime, the mobile Cu-species lose their ligands and find docking sites at the internal walls of the zeolite framework thus reflecting the idea of a *single-site* catalysts.

After a brief introduction, the review is divided into three main parts devoted to characterization (Section 2), reactivity (Section 3), and industrial applications (Section 4), followed by some concluding remarks and providing a perspective of the field.

1. Introduction

Natural chabazite is a tectosilicate mineral of the zeolite group, with a high aluminum content, that crystalize in the trigonal R-3m space group.[1-3] Its synthetic counterpart can be obtained, by the use of a sophisticated template, with Si/Al ratio higher than 10 and is known as SSZ-13.[4] Finally, the same topology can be obtained also as silicon aluminum phosphate, known as SAPO-34.[5] The chabazite topology is identified by layers of double six-membered rings (*d6r*) that are interconnected by units of four-membered rings (*4r*). The double six-membered-ring layers are stacked in an ABC sequence, leading to a framework with a regular array of barrel-shaped cages interconnected by eight-membered-ring windows (*8r*) (Fig. 1a). The chabazite framework is characterized by a high symmetry, as the asymmetric unit contains just one T site[1-3, 6] and four non-equivalent oxygens, which give origin to two families of Brønsted sites.[7, 8] The first family include Brønsted sites associated with O_1, O_2 and O_4, that point inside the big cage and are easily accessible to reactants. The Brønsted sites associated with O_3 are instead less accessible, pointing inside the six-membered ring (*6r*) (Fig. 1b).
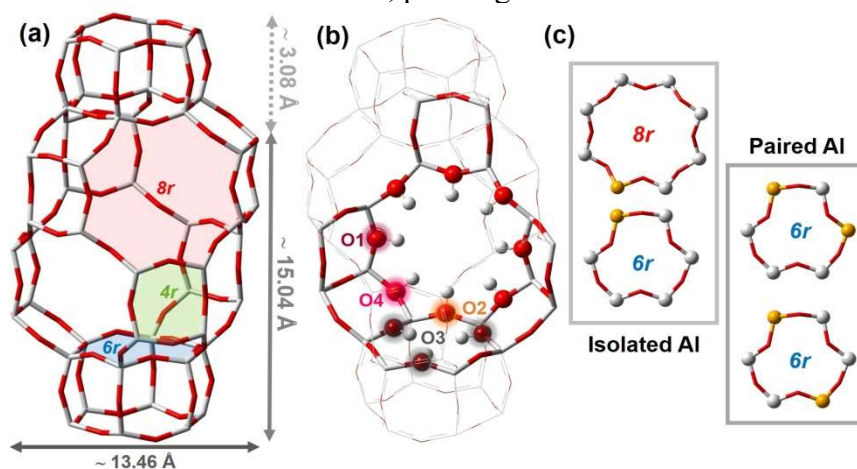

Fig. 1. Part (a): schematic representation of CHA topology, underlying the presence of *4r*, *6r* and *8r* rings and the major dimension of the cages. Part (b): illustration of the four different oxygens available in the framework. Part (c): possibilities of isolated and paired Al sites, considered in the literature as most probable locations for Cu cations. Colour code: O red; Si grey; Al orange in case of zeolites (CHA or SSZ-13). A similar picture can be used to describe SAPO-34, where Al is replaced by Si and Si by alternating Al and P atoms. Previously unpublished figure.

A further element of complexity, in case of the CHA or the SSZ-13 zeolites, is represented by the Al loading, that implies a variability in the presence of one or two Al atoms in the zeolite rings. In particular, the different possibilities of isolated and paired Al sites are illustrated in Fig. 1c. Equivalent structures can be used to describe the SAPO-34 case,[9] where the Al is replaced by Si and Si by alternating Al and P atoms.

Apart from the interest in the acidic form of chabazites (H-CHA, H-SSZ-13 and H-SAPO-34),[7, 8] mostly associated to the catalytic conversion of methanol into light olefins (MTO reaction),[10, 11] and in the H_2-storage abilities,[12, 13] chabazites shows some interest in catalytic properties engendered by isomorphous substitution.[14, 15] However, the major reason for the high research interest in inn the system raised around 2008-2009, when the Cu-CHA redox catalyst was commercialized for NO_x reduction in lean-burn diesel engine aftertreatment. Moreover, the structural simplicity of the material attracted a great interest in Cu-CHA as a model system to resolve fundamental questions of structure-performance relationships in the general context of metal-exchanged zeolite catalysis.

In particular two relevant redox processes, where copper interconverts between Cu(I) and Cu(II) have been the subject of important research efforts in the last years: (i) the reduction of environmentally harmful NO_x by NH_3, *i.e.* selective catalytic reduction (SCR)[16-27] and (ii) the direct conversion of methane to methanol (MTM, sometime indicated in the literature as partial methane oxidation PMO).[28-35]

In order to shed light on the structural dynamics of the Cu-CHA system, it has been mandatory to apply advanced *in situ/operando* characterization approaches on a well-defined set of samples, by varying, in a controlled way, the measuring conditions.[22, 36-40] Additional insights were provided by the use of probe molecules, by performing ab-initio calculations on clusters and on periodic models, and by combining appropriate analytic tools, specifically developed to manage complex spectroscopic datasets. Fig. 2 illustrates the large variety of approaches employed in the literature to tackle the complexity of the problem, as will be exemplified by the studies discussed in this review.
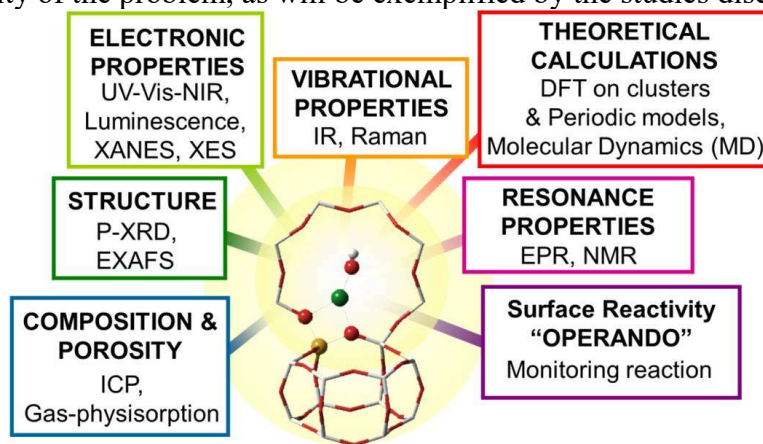

Fig. 2. Scheme reporting the main experimental and theoretical tools used to shed light on the structure of the active Cu sites in CHA frameworks and their reactivity in the context of NH_3 SCR and MTM reactions. Previously unpublished figure.

Starting from the bottom left, we can mention the use of: analytical tools such as ICP and gas-physisorption to define the sample composition and surface area. With respect to gas-physisorption,[41] the most used methods include N_2- and Ar-physisorption, where the latter is often employed to characterize the pore structure of CHA zeolites because of the incomplete packing of N_2 in this zeolite topology. Powder X-ray diffraction (PXRD) results in the phases identification needed to verify the purity of the crystalline phase. Moreover, if highly 2θ-resolved pattern (with a high signal-to-noise in the high-q-region) are available, PXRD can also be used to track the positions of the cations, thanks to a structure refinement procedure.[6, 18, 42] Conversely, the short range order is mostly described by extended X-ray absorption fine structure (EXAFS),[37, 43-53] while spectroscopies involving electron transitions (UV-Vis-NIR, luminescence, XANES and XES)[27, 35, 45, 53-60] are able to discriminate between Cu(I) and Cu(II) and to give insight on the local symmetry and coordinative state and the nature of coordinating ligands. Infrared spectroscopy[61-63] provides a clear picture about the number and the different families of Brønsted sites and, when used in combination with probe molecules,[64-67] can provide insight about the oxidation state and accessible coordinative environment of the Cu species. Raman spectroscopy, mostly exploiting the resonance conditions,[31, 68-74] allows the identification of even very diluted surface species in controlled atmosphere. Theoretical calculations performed on both clusters and periodic models using DFT,[24, 36, 53, 75-79] provide a relevant contribution in the understanding of the local geometries and reactions paths. Molecular Dynamics (MD) enables a deeper mechanistic understanding under reaction conditions yielding adsorbate-mobilized Cu active-species (primary, low-temperature NH_3-SCR, see Section 3.1.1), acting in a pseudo-homogenous manner within the confined space of the zeolite cages.[77, 79, 80]

As Cu(II) is paramagnetic, EPR spectroscopy is widely used to characterize Cu(II) sites in exchanged zeolites.[26, 81-88] or Cu(I) sites accessible to paramagnetic molecules such as NO.[89] Solid state NMR has been mostly used to give insight on ^{27}Al local structure and in particular to identify extra lattice aluminium sites.[90, 91] In addition, ^{29}Si was used to determine the distribution of Si(2Al), Si(1Al) and Si(0Al) in SSZ-13[25] and ^{15}N-MAS NMR provided insight on the adducts formed upon

NH$_3$ dosage.[92] Last but not least, *operando* facilities, starting from reaction tests, are more and more frequently combined with spectroscopies, providing insight on the surface species formed and evolving under reaction conditions.[22, 36-40]

The present review is focused on Cu-SSZ-13 zeolites, as these are the materials on which the most abundant literature is available. The manuscript is divided into three main parts devoted to characterization (Section 2), reactivity (Section 3), and industrial applications (Section 4), that are finally followed by a section where conclusions and perspectives are drawn.

2. Structural complexity in the activated material

The coincidence of the structural simplicity of the CHA topology,[1-3] together with the outstanding performance of Cu-SSZ-13 in NH$_3$-SCR, provoked a real boom of academic and industrial research groups using Cu-SSZ-13 materials as model systems to address long-standing questions in metal-exchanged zeolite catalysis. Nonetheless, the vast literature accumulated in almost a decade of extensive research, reshaped the initial premise of a simple model material, progressively unveiling the complexity associated with metal speciation in the CHA framework.

Early reports[18, 52, 93] described Cu-SSZ-13 as a 'single-site' catalyst, indicating an extra-framework site in the plane of the *6r* as the sole position for Cu ions in the dehydrated material. However, in the following years, it has become clear that the CHA topology offers multiple docking sites for Cu(II) and Cu(I) ions.[6, 42, 53, 59, 75] Today it is well established that the chemical identity (oxidation state, coordination geometry, nuclearity) and the framework location of Cu-species are determined by (i) physico-chemical environment (*i.e.* temperature, gas composition and gas flow rate) and (ii) sample composition (*i.e.* Si/Al ratio in the parent framework and Cu/Al ratio in the exchanged zeolite).[53, 59, 75, 76, 94]

This section addresses the current understanding of Cu-species formation and transformation in Cu-CHA materials as a function of two key factors: activation procedure (Section 2.1) and starting chemical composition (Section 2.2). Additional complexity is connected to the non-random distribution of Al in the zeolite framework and the playing room created by the possibility of on purpose modifying the Al distribution in the CHA framework (e.g. abundance of 6r hosting a pair of neighbouring Al atoms in −Al−Si−Al− or −Al−Si−Si−Al− coordination motifs)[95] by tuning the synthesis methods and parameters. Such a non-random distribution of framework Al has been known and described with some detail for ZSM-5[96] and other zeolites.[97] However, the means by which to selectively influence or even direct the Al distribution leaves something to be desired. Dedecek et al.[96] varied the overall Al content, the sequence of mixing of reagents, the Si and Al source, as well as the concentration of alkali cations and inorganic anions to prepare sets of ZSM-5 zeolites with different distributions of Al in the framework. It may be noted that ion exchange with [Co(II)(H$_2$O)$_6$] followed by dehydration and analysis by UV spectroscopy provide a means to detect different Al arrangements.[98] Dehydrated, bare Co(II) ions balanced by two close Al framework atoms give rise to distinct d-d transitions, whereas various Co(II)-oxo species balanced by Al atoms further apart give rise to absorptions related to charge transfer transitions in the UV spectrum. Co(II) can also be used quantitatively as a titrant to determine the fraction of paired framework Al.[99]

A more systematic method to control the Al distribution has been reported for CHA. Di Iorio and Gounder[95] demonstrated that SSZ-13 crystallized using the very phase selective trimethyladamantyl ammonium cation from hydroxide resulted in only isolated Al atoms in the framework (Si/Al = 15-30). The addition of increasing concentrations of Na$^+$ to the synthesis gel led to a linearly correlated density of paired (separated by one or two Si units) framework Al. Moreover, it was demonstrated that at equimolar concentrations of SDA and Na$^+$ it was possible to prepare a series of materials with varying Al content for which the density of Al pairs was governed solely by a random distribution and Löwenstein's rule.[100] In a follow up contribution, the same team[99] was able to show that two neighboring Brønsted sites arising from paired Al were 10 times more active than isolated protons for the dehydration of methanol to DME.

However, the vast majority of contributions discussed here deal only with a limited number (one) of samples of zeolite supports, or do not characterize the Al distribution in detail (using the approaches based on the introduction of Co(II) mentioned above. Thus, it is in most cases not possible to discriminate between effects arising from the kinetics of the Cu exchange or by the density of paired Al. Further details on the synthesis influence on Cu-speciation can be found by the interested reader in the excellent chapter by Paolucci *et al.*,[76] which exhaustively discusses this matter for Cu-SSZ-13 and Cu-SAPO-34 catalysts.

In the following subsections 2.1 and 2.2, our focus here will be on the dehydrated (or 'activated') state of the material, which represents generally the starting point before catalysis. Herein we will demonstrate how *in situ/operando* multi-technique characterization guided by computational modelling has now enabled a renewed understanding of metal speciation and redox chemistry in these fascinating materials. The impact of the Cu-speciation in the activated material on the performance, as well as its reaction-induced modifications, will be then examined in Section 3 for two selected processes, namely NH_3-SCR and MTM conversion.

2.1. Activation-dependent Cu-speciation

Activation of zeolites, that are microporous materials, is a key step for both catalysis and sorption purposes, because the evacuation of water and other molecules adsorbed in the channels and cavities is necessary to make the active sites accessible to reactants. Incomplete activation can result in residual H_2O or hydrocarbon molecules, which may block and/or modify the activity of a fraction of the sites.[63, 101] The same holds when activation precedes a volumetric, calorimetric or spectroscopic investigation with a specific probe molecule; the simultaneous presence of water may prevent adsorption of the probe and/or may result in misleading results because of competition for the adsorption at the same site.

Since the discovery in the nineties that Cu-ZSM-5 zeolites are active in the direct decomposition of NO_x into N_2 and O_2,[102-108] the activation of Cu-exchanged zeolites has been followed by several spectroscopic studies. Besides isolated cases where copper was inserted in the zeolite as Cu(I) species via gas-phase[46, 48-50, 109-113] or solid phase[114-116] exchanges with CuCl, in the vast majority of the literature the cation exchange was performed via aqueous phase ion-exchange using different cupric salts.

The nature of copper in as-prepared ion-exchanged zeolites from aqueous preparation conditions, is generally agreed to be hydrated Cu(II) species. It was also immediately recognized that hydrated Cu(II) species in copper-exchanged zeolites undergo a progressive reduction to Cu(I) upon activation under vacuum or inert atmosphere (He or N_2) at increasing temperatures.[82-84, 117-122] The phenomenon has been described as "self-reduction" or "auto-reduction", owing to the fact that even though several different reduction processes were proposed, no direct proof or identification of the species that has to become oxidized in the process was found.

On the other hand, already in the middle of the nineties it became evident that an activation performed in presence of O_2 resulted in samples characterized by very different copper species,[123, 124] as compared to an inert or vacuum activation. This evidence was confirmed in successive works.[53, 59, 65, 72, 73, 125] This was actually an important finding, since in a catalytic redox process both states, the reduced and oxidized metal state, should be addressed. In this regard, the collaboration between Haldor Topsøe and different academic partners provided a systematic investigation of three batches of Cu-SSZ-13 samples prepared in the same way with comparable chemical composition ($13.1 \leq$ Si/Al ≤ 15.5 and $0.44 \leq$ Cu/Al ≤ 0.48) subjected to both inert- and O_2-activation using an impressive number of complementary characterization techniques: IR,[53, 65] IR of adsorbed probe molecules,[58, 65] UV-Vis,[65] EPR,[65, 86] XANES,[53, 58, 59] EXAFS,[53, 59] XES,[53, 58] synchrotron radiation PXRD[6] and simultaneous synchrotron radiation PXRD/XANES.[42] The picture was then also supported by quantum mechanical modelling using DFT.[6, 53, 59] Hereafter we will mainly summarize the results of those combined studies as they represent a set of self-consistent data sets coming from independent spectroscopic and scattering techniques, providing a complete structural, electronic and vibrational

picture on the evolution of the population of Cu sites along the two different activation procedures.[6, 42, 53, 58, 59, 65, 86]

2.1.1. IR spectroscopy: revealing the presence of Cu(I) and Cu(II) sites and of [CuOH]+ species.
Starting form IR spectroscopy, Fig. 3a reports the FTIR spectra of dehydrated Cu-SSZ-13 zeolite collected after O_2-activation and vacuum-activation, red and black curves, respectively. The main features in the ν(O–H) stretching region, left part, are the bands due to external silanols (3737 cm^{-1})[126-128] and to internal Brønsted sites (3611 cm^{-1}, 3584 cm^{-1}),[7, 65] that are similarly present after both activations. In the low wavenumber region (right part of Fig. 3a), the main feature in the 840-770 cm^{-1} region, which is due to the total symmetric stretching of the [SiO$_4$] units,[68] dominates both spectra. However, the spectrum of the O_2-activated sample exhibits two minor, but distinct, features at 3656 and 905 cm^{-1} which are not observed for the vacuum activated sample. Giordanino *et al.*[65] were the first to assign those bands to the stretching and bending fingerprints of [CuOH]+ species stabilized in the SSZ-13 matrix,[53, 65] assignment successively confirmed by authoritative groups active in the field,[35, 75, 129] vide infra Fig. 5a for a pictorial representation of this Cu(II) species hosted in the large cage of the CHA framework. The absence of both bands in the vacuum-activated sample allowed Borfecchia *et al.* to conclude that the stabilization of the OH extra-ligand on Cu(I) does not occur.[53]
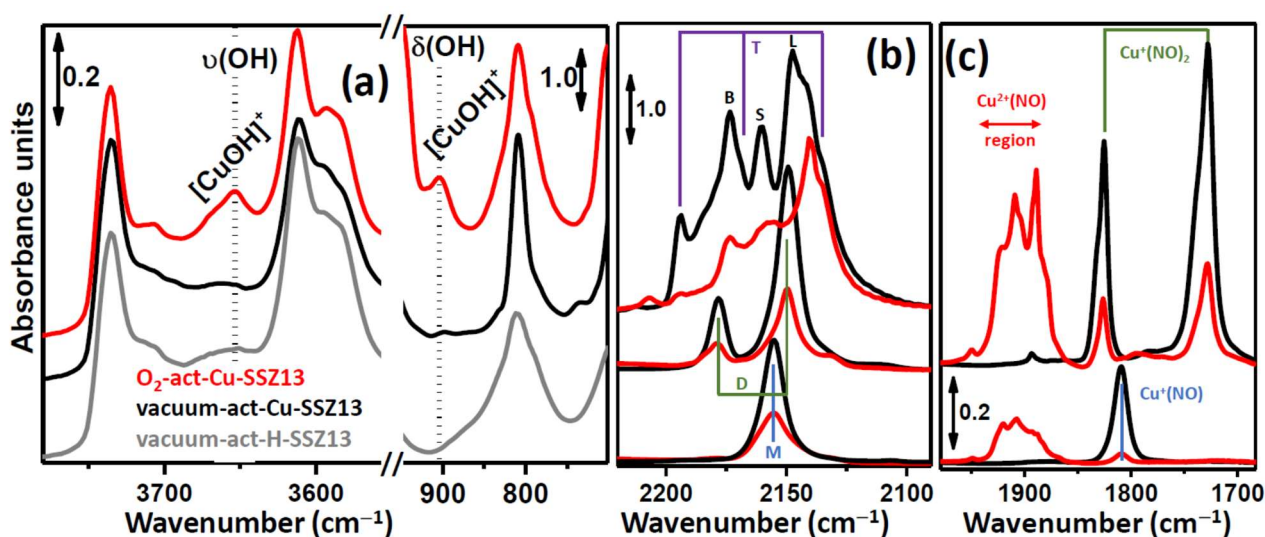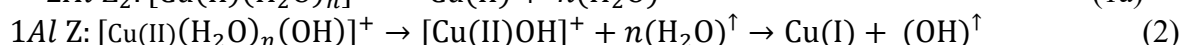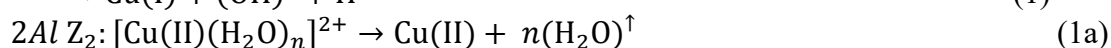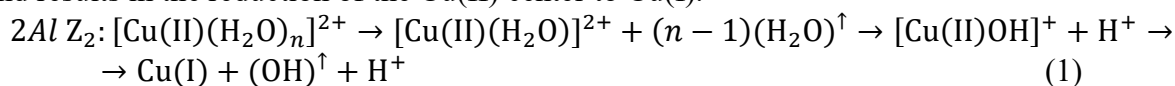

Fig. 3. Low temperature (~100 K) IR spectra of O_2-activated (red) and vacuum-activated (black) Cu-SSZ-13 zeolite (Si/Al = 13.1 and Cu/Al = 0.444). Part (a): effect of activation at 400 °C in the ν(OH) and δ(OH) stretching regions, left and right parts, respectively. For comparison, also the spectrum of the vacuum-activated H-SSZ-13 material (gray) is reported. The O_2-activated zeolites presents the fingerprint bands of [CuOH]+ species at 3655 and 905 cm^{-1}. Part (b): IR spectra of CO adsorption at low, intermediate and high P_{CO}, bottom, middle and top curves respectively, approximately corresponding to the saturation of mono- (M band), di- (D doublet) and tri-carbonyl (T triplet) complexes. At the highest P_{CO}, also the bands of CO adsorbed on Brønsted (B), silanols (S) and the band of liquid-like CO are present after both activation. Part c: IR spectra of NO adsorption at low and high P_{NO}, bottom and top curves respectively, approximately corresponding to the saturation of mono- and di-nitrosyl complexes on Cu(I) sites. In all parts some spectra have been vertically shifted for clarity. Unpublished figure reporting spectra previously published in Ref.[53] for part (a) and in Ref.[65] for parts (b) and (c).

The comparison with the spectrum collected on the non-exchanged parent H-SSZ-13 material (gray curves in Fig. 3a) highlighted that the intensities of the 3611 and 3584 cm^{-1} bands related to Brønsted sites are only slightly lower in the Cu exchanged sample (red or black spectra). This spectroscopic observation was particularly relevant because it could explain why a sample which has been theoretically almost fully ion-exchanged (Cu/Al ratio of 0.444) can still preserve plenty of free Brønsted acid sites. The formation of [CuOH]+ species was explained according to two possible mechanisms.[53]

In case two framework Al atoms are in a close proximity (*2Al* Z$_2$ sites), the stabilization of divalent [Cu(II)(H$_2$O)$_n$]$^{2+}$ complexes is favored and their progressive dehydration leads to H_2O dissociation into [Cu(II)OH]+ and H+ species, Eq. (1a); the two cationic species will balance the charge of the two

7

adjacent framework Al atoms. The FTIR study of Borfeccia et al.[53] proved that, at 250 °C, copper sites are fully dehydrated and for higher temperatures $[Cu(II)OH]^+$ species can only be stabilized in an oxidative atmosphere only, otherwise they undergo "self-reduction" as a consequence of OH^- extra-ligand loss. Alternatively, dehydration of $[Cu(II)(H_2O)_n]^{2+}$ complexes could lead to bare Cu(II) cations, Eq. (1b). Conversely, in those sites characterized by only one Al in the proximity (*1Al Z* sites), the hydrated state upon aqueous ion exchange is a monovalent $[Cu(II)(H_2O)_n(OH)]^+$ complex, that does not require any water dissociation to be transformed into $[Cu(II)OH]^+$ upon dehydration, see Eq. (2), and the concentration of Brønsted sites in the dehydrated material is the one predicted from a total exchange level of $[Cu(II)OH]^+/Al^{3+} = 1$. In all these cases, the loss of the OH^- extra-ligand results in the reduction of the Cu(II) center to Cu(I).[53]

$$2Al\ Z_2: [Cu(II)(H_2O)_n]^{2+} \rightarrow [Cu(II)(H_2O)]^{2+} + (n-1)(H_2O)^\uparrow \rightarrow [Cu(II)OH]^+ + H^+ \rightarrow$$
$$\rightarrow Cu(I) + (OH)^\uparrow + H^+ \qquad (1)$$
$$2Al\ Z_2: [Cu(II)(H_2O)_n]^{2+} \rightarrow Cu(II) + n(H_2O)^\uparrow \qquad (1a)$$
$$1Al\ Z: [Cu(II)(H_2O)_n(OH)]^+ \rightarrow [Cu(II)OH]^+ + n(H_2O)^\uparrow \rightarrow Cu(I) + (OH)^\uparrow \qquad (2)$$

The reversibility of the OH^- extra-ligand loss has been confirmed by XAS and FTIR, demonstrating that Cu(I) sites rapidly undergo re-oxidation with consequent restoration of $[Cu(II)OH]^+$ species if they are exposed to a gas mixture of O_2/H_2O.[53]

IR spectroscopy of adsorbed probe molecules is a powerful technique in the characterization of surface sites of porous, high surface area, materials.[61-64, 130, 131] The choice of probe molecule is a crucial point in this approach; different probe molecules may be able to reveal different aspects of the investigated surface, and often the combined use of markedly different probes is the key to reach a comprehensive understanding of the surface.[64] In this regard, Giordanino et al. reported an extensive characterization of Cu-SSZ-13 activated under oxidative and reductive (vacuum) conditions and tested by N_2, CO and NO probes.[65]

CO is the ideal molecule to probe Cu(I) sites because of both the high extinction coefficient and the strong adsorption energy.[111, 132] The high coordinative unsaturation of Cu(I) cations hosted in vacuum-activated zeolites was already demonstrated in the 1990's by the observation that multiple carbonyl complexes form, *i.e.* $Cu(I)(CO)_n$ (n =1,2,3), depending on CO equilibrium pressure (P_{CO}) and temperature.[45, 46, 49, 50, 84, 110, 133, 134] At low P_{CO} (bottom spectra in Fig. 3b) the typical band (M) at 2155 cm^{-1} due to Cu(I)(CO) monocarbonyl complexes is observed. By increasing P_{CO} the doublet at 2178 and 2148 cm^{-1}, due to the symmetric and asymmetric stretching modes of the $Cu(I)(CO)_2$ complexes,[45, 46, 49, 50, 84, 109, 110, 133, 134] (D-bands, in the middle spectra of Fig. 3b) start to appear at the expense of the monocarbonyls (M-band). M- and D-bands appear independently on the activation treatment but are significantly more intense (by a factor 4) in case of *inert*-activated sample (black curves), confirming the higher concentration of Cu(I) ions relative to the O_2 activated one (red curves). In addition, a more heterogeneous distribution of the Cu(I) sites after oxidative pretreatment compared to inert-activation is recognized by comparing the FWHM of the M bands, which are 14 and 9 cm^{-1}, respectively.

Higher P_{CO} leads to the formation $Cu(I)(CO)_3$ tri-carbonyl complexes (triplet T at 2134, 2169 and 2194 cm^{-1}, in the top spectra in Fig. 3b), that are however less clearly visible because of an increased complexity in the IR spectra. Indeed, at such P_{CO} values, CO starts to be coordinated also on sites characterized by lower adsorption enthalpies such as Brønsted and silanols, bands at 2173 cm^{-1} (B) and 2160 cm^{-1} (S), respectively[126, 135]. The band at 2138 cm^{-1} is due to liquid-like CO physisorbed in the zeolite channels.[135-137] Giordanino et al.[65] noticed that the intensity of the Brønsted acid sites related bands is not enhanced in the *vacuum* activated sample compared to the O_2 activation. This indicates that for a Cu-CHA sample with Si/Al~15 and Cu/Al~0.5 the self-reduction of Cu(II) into Cu(I) during the *vacuum* activation process does not generate new H$^+$ sites to compensate the loss of one positive charge for all copper atoms. This observation rules out the presence of a significant fraction of Cu(II) able to balance the negative framework charge induced by two adjacent Al atoms

and implies that most of the cupric sites are inserted in form of monovalent complexes such as [Cu(II)OH]$^+$.[65]

Due to the weaker interaction between Cu(II) and CO the corresponding Cu(II)(CO) complexes are very unstable and difficult to detect even at low temperature,[131, 138] particularly when they co-exist with even just a minority of Cu(I) sites. This is the reason why the IR band of Cu(II)(CO) complexes, expected around 2194 cm^{-1}, is not appreciable, even in the O$_2$-activated sample, where Cu(II) surface species are the most abundant ones. Cupric species can be monitored by NO as a probe, with the advantage that NO is able to form complexes with both Cu(I) and Cu(II) sites.[45, 61, 64, 67, 112, 139, 140] At low P$_{NO}$, *vacuum* activated Cu-SSZ-13 (black curve in the bottom of Fig. 3c) shows a band centered at 1810 cm^{-1} due to Cu(I)(NO) mononitrosyl complexes;[45, 61, 64, 109, 112, 139] At high P$_{NO}$ (top black curve), the 1810 cm^{-1} band evolves in two main components at 1826 and 1728 cm^{-1} due to the symmetric and asymmetric stretching of Cu(I)(NO)$_2$ dinitrosyl complexes, respectively.[45, 61, 64, 112, 139, 140] The absence of any significant band in the 1950-1870 cm^{-1} range, where Cu(II)(NO) complexes are expected, implies that almost all cupric ions in accessible positions have been reduced to cuprous ions during the thermal activation in vacuo. The situation is different for the O$_2$-activated sample (red curves in Fig. 3c), where bands due to Cu(I)(NO) and Cu(I)(NO)$_2$ complexes are present as a minority, and the spectra are dominated, at both low and high P$_{NO}$, by a complex and structured absorption in the 1970-1850 cm^{-1} range due to Cu(II)(NO) adducts. The complexity of the absorption features of Cu(II)(NO) adducts indicates the presence of different Cu(II) cationic sites, that are not present in the reduced cuprous sites.[65] The heterogeneity of Cu(II) sites was also confirmed by the combined H$_2$-TPR/IR study of Kwak *et al.*[141] and by the EPR study of Godiksen *et al.*,[86] who found two EPR active sites in the *6r*. In the same work the authors also addressed the long-standing question of the EPR silent monomeric Cu(II) species in Cu-zeolites[82-84] in terms of [Cu(II)OH]$^+$ species coordinated to two framework oxygen atoms bonded to an isolated Al atom, namely *1Al* Z[Cu(II)OH] according to the nomenclature introduced above.[86] CO and NO molecules are coordinated too strongly to Cu(I) to be suitable probes to discriminate among small cuprous site inhomogeneities; weakly interacting molecules such as N$_2$ are required for this porpoise. Giordanino *et al.*[65] followed the evolution of IR spectra of when dosing N$_2$ at around 100 K on vacuum activated Cu-SSZ-13, observing two components at 2293 and 2300 cm^{-1}. The two bands were assigned to N$_2$ molecules adsorbed on Cu(I) sites in the *8r* and *6r* respectively,[59, 65] the former being a stronger adsorption site, because the 2300 cm^{-1} band is the only one observed at low P$_{N2}$, and because it is characterized by a larger red-shift of the ν(N≡O) stretching mode. The observation that the relative intensity of the IR components of the two Cu(I)···N$_2$ complexes changes in Cu-SSZ-13 samples characterized by different Cu/Al and Si/Al ratios clearly indicated a dependence of Cu(I) site distribution on the catalyst composition and will be commented in Section 2.2, vide infra Fig. 13b.

2.1.2. UV-Vis and Raman spectroscopies: insights on Cu(II) active-oxygen species. Very peculiar are the d-d transitions of Cu(II) species in O$_2$-activated Cu-SSZ-13, see the UV-Vis-NIR spectrum in Fig. 4a (blue curve). Giordanino *et al.*[65] highlighted the presence of a very intense and very well defined quadruplet with maxima at 19700, 16500, 13600 and 11000 cm^{-1}, that is responsible for the deep blue color of the O$_2$-activated sample, see inset in Fig. 4a. Still under debate is the precise assignment of this quadruplet either to different Cu(II) species/sites, reflecting the Cu(II) heterogeneity discussed above, or to a single site subjected to a very specific ligand field.[86] Support from advanced DFT calculations is needed here. The sample is also characterized by a complex charge-transfer band extending down to 25000 cm^{-1}. Oord *et al.*[35] reported *operando* UV-Vis-NIR spectra following the sample activation, both in O$_2$- and He-flow conditions, see Fig. 4b and c, respectively. Upon activation the typical d-d component of hydrated Cu(II) species around 12000 cm^{-1} (green spectra in Fig. 4a,b,c) progressively evolves into the structured quadruplet discussed above, which intensity however does not show a monotonic increase with activation temperature as it reaches a maximum at 320 °C and then partially loses intensity (see arrows in Fig. 4b,c). This observation is in line with the *in situ* FTIR study by Pappas *et al.*,[33] who observed that the finger print band of cupric [Cu(II)OH]$^+$ species was depleted by increasing the O$_2$-activation temperature form

250 °C (Fig. 4d). The activation experiments by Oord *et al.* were successively followed by methane addition during temperature ramp from 60 to 200 °C (vide infra section 3.2.4, in particular Fig. 22e); the authors concluded their *operando* UV-Vis-NIR study observing that an oxidizing agent is needed to create the active site for methane to methanol activation in Cu-SSZ-13 as no methanol production was measured after He-activation.[35]
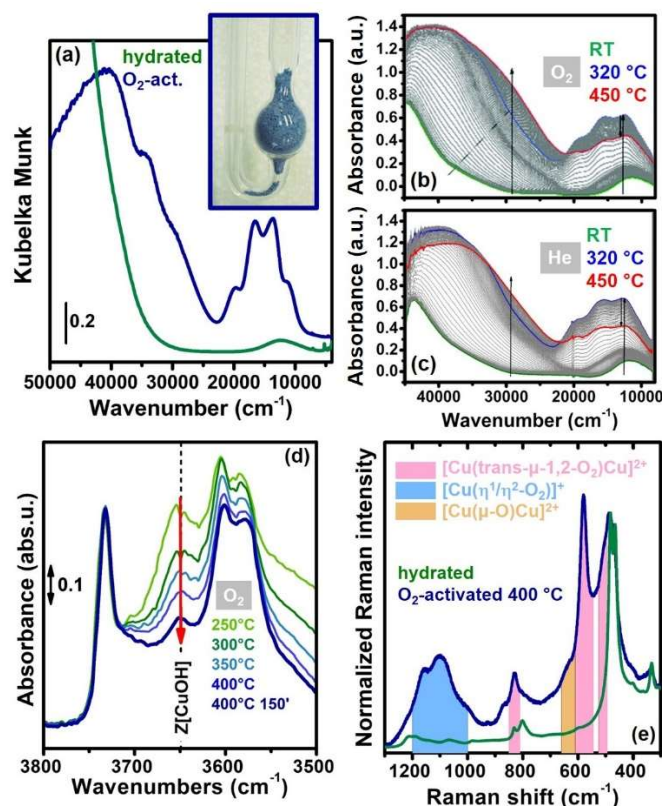

Fig. 4. Part (a): Comparison between in situ UV-Vis-NIR spectra of hydrated (green curve) and O$_2$-activated (blue curve) Cu-SSZ-13 zeolite (Si/Al = 13.1 and Cu/Al = 0.444). Adapted by permission of the Royal Chemical Society (copyright 2013) from ref. [65] Part (b): *operando* UV-vis spectra of the Cu-1.21-Na-Cu-SSZ-13 zeolite (Si/Al = 20 and 1.21 Cu wt %) during O$_2$-activation from RT (green spectrum) to 450 °C (red spectrum). The arrows indicate the time evolution, the green spectrum is the starting point of the experiment, the d-d quadruplet reaches maximum intensity at 320 °C, blue spectrum. Part (c): as part (b) during He-activation. Parts (b,c) adapted with permission of the Royal Chemical Society (copyright 2018) from ref.[35]. Part (d): FTIR spectroscopy in the ν(OH) stretching region as monitored in situ along O$_2$-activation of Cu-SSZ-13 (Si/Al = 14.8 and Cu/Al = 0.53) catalyst in the 250 – 300 °C range. The red arrow highlights the progressive decrease in the intensity of the band at ca. 3650 cm^{-1} fingerprint band of cupric [CuOH]$^+$ species upon increasing the activation temperature from 250 °C. Part (e): Raman spectra (λ$_{ex}$ = 488 nm) of Cu-SSZ-13 (Si/Al = 14.8 and Cu/Al = 0.53) catalyst in its hydrated (green line) and O$_2$-activated (blue line) forms. The spectral contributions from the observed Cu(II)$_x$O$_y$ moieties are highlighted: [Cu(*trans-μ*-1,2-O$_2$)Cu]$^{2+}$ (pink shading); [Cu-(*μ*-O)-Cu]$^{2+}$ (orange shading); and [Cu(II)O$_2$$^\bullet$]$^+$ (light-blue shading). Parts (d,e): adapted by permission of the American Chemical Society (copyright 2017) from ref.[33]

Raman spectroscopy is particularly suited to detect multinuclear Cu(II)$_x$O$_y$, it has been widely used to characterize active copper sites in biological systems[57, 142] and in O$_2$-activated zeolites.[31, 33, 72-74, 143] Fig. 4e reports the evolution of the Raman spectrum of Cu-SSZ-13 catalyst before (green line) and after (blue line) O$_2$-activation.[33]

Several new vibrational features, related to oxygen-activated Cu(II) species appear after O$_2$-activation: [Cu(II)O$_2$$^\bullet$]$^+$ end-on superoxo species (strong and complex light-blue shaded components in the 1000 - 1200 cm^{-1} interval, with two maxima at 1100 and 1155 cm^{-1})[33, 72] in equilibrium with the corresponding side-on species, pictorially represented in Fig. 5b;[33] [Cu(*trans-μ*-1,2-O$_2$)Cu]$^{2+}$ complex (orange shaded components at 510, 580, and 830 cm^{-1}), see Fig. 5c for a pictorial representation;[31, 33] and [Cu-(*μ*-O)-Cu]$^{2+}$ complexes (pink shaded shoulder around 620 cm^{-1}).
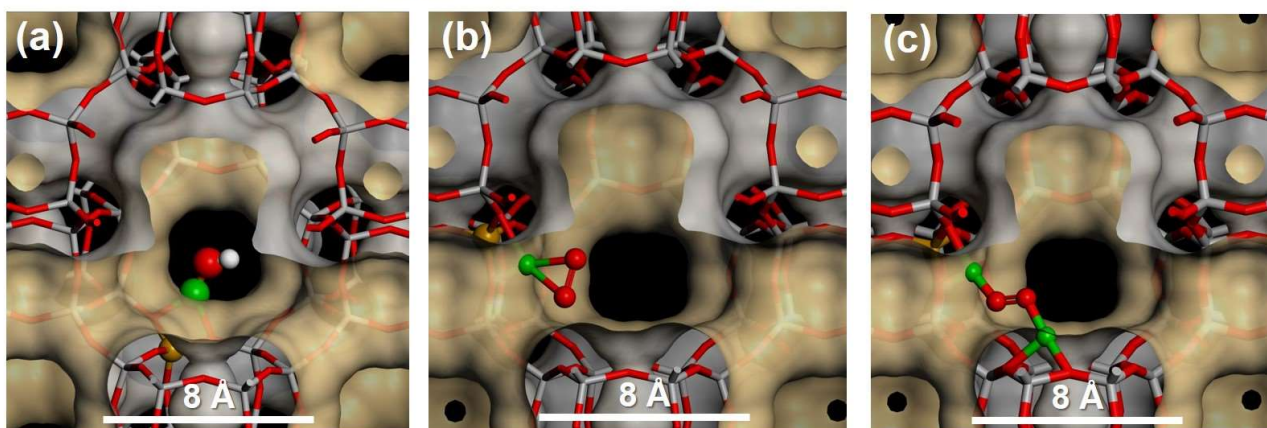
Cu-CHA (SSZ-13 and SAPO-34)

Fig. 5. Pictorial representation of some proposed local structures of the copper species formed in the large cage of the CHA frameworks under oxygen treatment at high temperature. (a): [CuOH]$^+$ species. (b): [Cu(II)O$_2$']$^+$ side on superoxo species. (c): [Cu(*trans-μ*-1,2-O$_2$)Cu]$^{2+}$. Colour code: Si grey, O, red, Al gold, Cu green, H, white. By courtesy of K. P. Lillerud (Department of Chemistry, University of Oslo), previously unpublished Figure.

2.1.3. DFT supported XAS and XES investigation: understanding the structure of the Cu(II) and Cu(I) species inn activated samples. Borfecchia *et al.*[53] followed the activation in temperature up to 400 °C in both O$_2$/He and pure He flows with XANES, EXAFS and valence-to-core XES spectroscopies. The EXAFS-optimized experimental setup and rather high copper content in the sample allowed a very good data quality paving the way to a detailed quantitative analysis. XANES, EXAFS and valence-to-core XES spectra, together with the optimized DFT models and corresponding XANES and XES simulations are reported in Fig. 6 and Fig. 7 for O$_2$- and He-activated samples, respectively. Borfecchia *et al.*,[53] tested several DFT models for Cu(II) and Cu(I) sites in the *8r* or in the *6r*, obtained inserting either one or two Al atoms in the T positions of the rings. Structures reported in Fig. 6c and Fig. 7c,d are only those that are compatible with the experimental results.

Fig. 6. Part (a): XANES spectra following the activation from room temperature (blue curve, hydrated material) to 400 °C (red curve, activated material) of Cu-SSZ-13 (Cu/Al=0.444, Si/Al=13.1) in 50% O$_2$/He flow. The inset shows a magnification of the 1s→3d transition, typical of Cu(II) species. Part (b) as part (a) for the k^2-weighted FT of the EXAFS spectra. Part (c): DFT model of the dominant Cu-site in the O$_2$-activated material. Part (d): best EXAFS fit and related main individual components obtained using the model reported in part (c). Part (e): experimental HERFD XANES spectrum (black curve) and computed XANES spectra (colored curves) for the different optimized possible sites. Part (f):

Upon activation in O_2/He flux, Cu(II) centers undergo progressive dehydration, while interacting more closely with the framework, maintaining the +2 oxidation state. Features typical for Cu(II) in low-symmetry environment were observed in XANES (Fig. 6a), while EXAFS witnesses the marked decrease of the first shell intensity due to the loss of the coordinated water molecules (Fig. 6b). Comparable evolution of the XANES spectra upon similar activation in oxidative environment was observed also by Kwak *et al.*[38] Conversely, as already observed by IR spectroscopy studies (see Section 2.1.1), upon activation in vacuum or in inert atmosphere the Cu oxidation state changes to +1, as evidenced for the Cu(II)-SSZ-13 system by the disappearance of 1s→3d transition and by the additional redshift of the edge, see Fig. 7a. Most interestingly, the EXAFS data reveal that the coordination of Cu upon He-activation was further decreased compared to the activation in O_2. Coupled with the observation that the reduction in He flow appears only at high temperature (T > 250 °C), while at lower T the evolution of the spectra is identical to the O_2-activation case, it indicates that a charged extra-ligand is still coordinated to Cu even at high temperature in case of O_2-activation. This evidence supports the hypothesis of the presence of an OH⁻ ligand in the first coordination shell of Cu(II) as advanced in the IR study of Giordanino *et al.*[65] to assign the ν(OH) stretching mode at 3657 cm⁻¹ and discussed in the previous section.
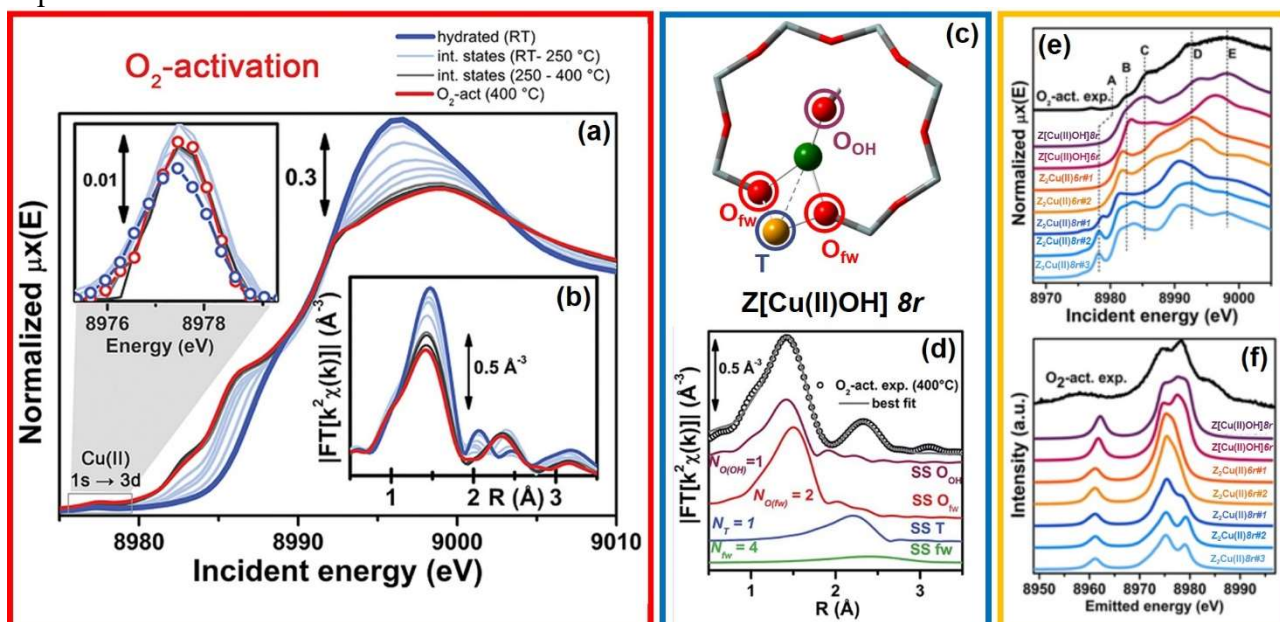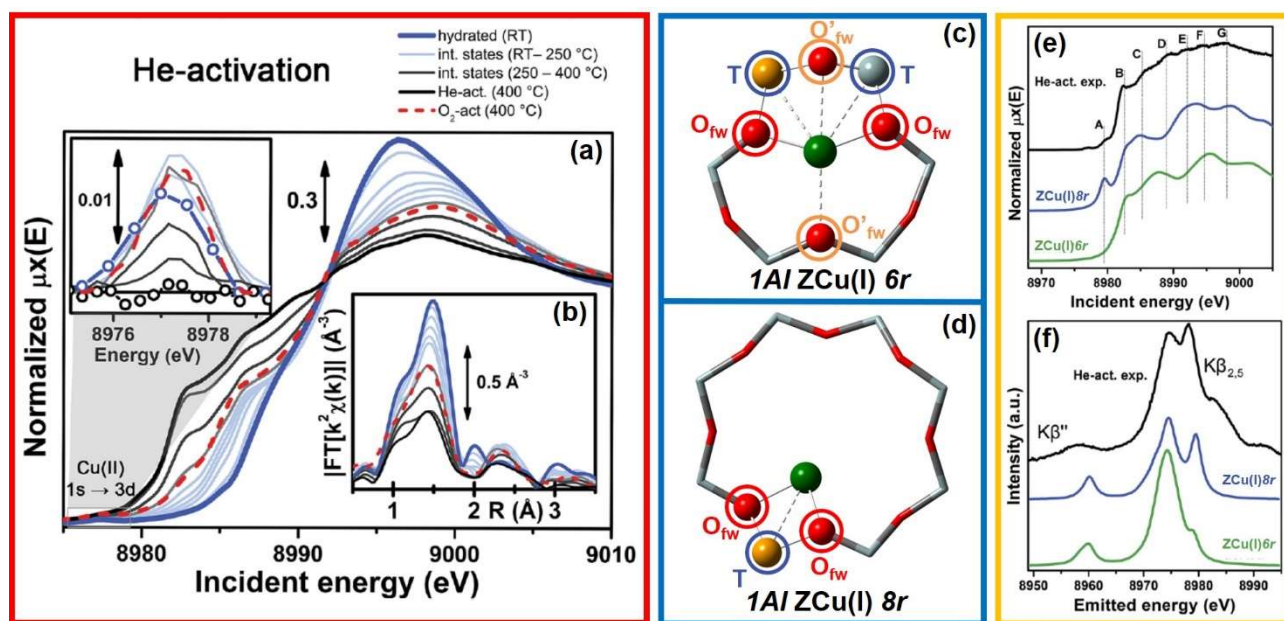

Fig. 7. Part (a): XANES spectra following the activation from room temperature (blue curve, hydrated material) to 400 °C (red curve, activated material) of Cu-SSZ-13 (Cu/Al=0.444, Si/Al=13.1) in inert He flow. The inset shows a magnification of the 1s→3d transition, typical of Cu(II) species and disappearing at high temperature. Part (b) as part (a) for the k^2-weighted FT of the EXAFS spectra. Parts (c,d): DFT model of the dominant Cu-sites in the He-activated material. Best EXAFS fit and related main individual components obtained using the model reported in part (c). Part (d): experimental HERFD XANES spectrum (black curve) and computed XANES spectra (colored curves) for the different optimized possible sites. Part (f): as part (e) for the valence to core XES spectra. Both HERFD XANES and XES simulations support the EXAFS results. Adapted by permission of the Royal Society of Chemistry (copyright 2015) from ref.[53]
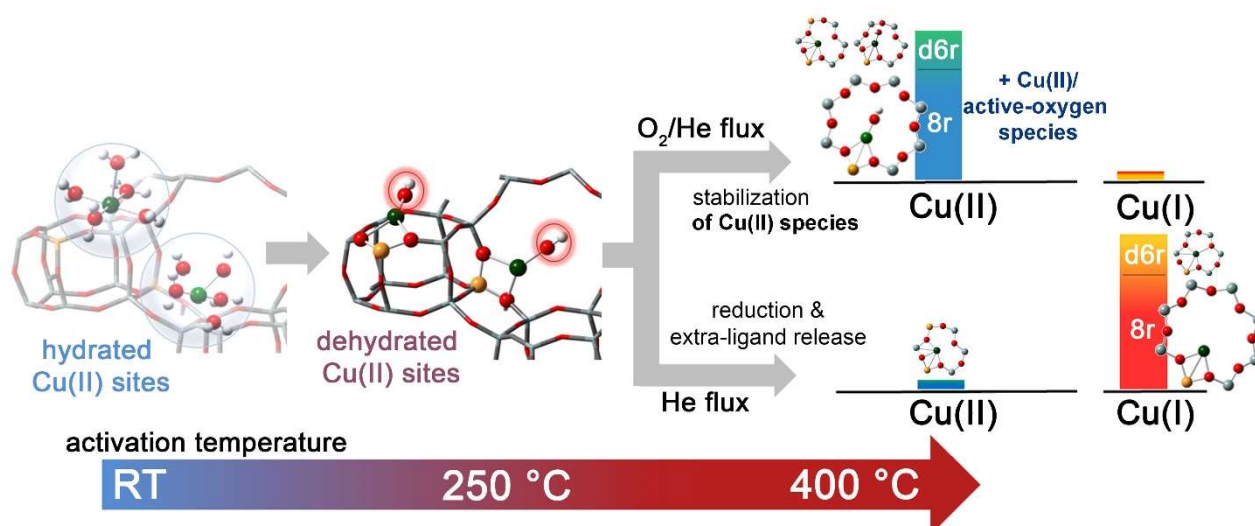
Fig. 8. Schematic representation of temperature/condition dependent Cu-speciation in Cu-SSZ-13 (Cu/Al=0.444 and Si/Al=13.1). O_2-activation resulted in a virtually 100 % Cu(II) sample, while the presence of a minor fraction (around 10%) of Cu(II) was detectable in the He-activated sample using HERFD XANES spectroscopy. The larger geometries depicted in the right side of the scheme are the dominant structural components identified by XAS, XES and FTIR in the Cu-SSZ-13 sample with this composition. As indicated in the scheme, based on the UV-Vis and Raman results discussed in Section 2.1.2 (Fig. 4), high-temperature thermal treatment in the presence of O_2 could also result in the formation of Cu(II)/active-oxygen species, see Fig. 5. Adapted by permission of the Royal Society of Chemistry (copyright 2015) from ref.[53]

Borfecchia et al.[53] have further tested this hypothesis by performing a set of DFT simulations of Cu ions in different locations of the framework and using the resulting structures as input for EXAFS fits and for the simulations of the high energy resolution fluorescence detected (HRFD) XANES and XES spectra, see parts (e) and (f) of Fig. 6 and Fig. 7. For the O_2-activated material, the best overall agreement with the experimental data was obtained for the models of Cu(II) in the 8r, in form of a Z[Cu(II)OH] complex, see Fig. 6c confirming the first assignment of the ν(OH) stretching mode at 3657 cm^{-1},[65] while in case of He-activation it was a bare Cu(I) cation hosted mainly in the 8r, with a minority occupancy of the 6r site, as summarized in the scheme reported in Fig. 8. This study was then extended in a successive work of the same group[59] to a set of six Cu-SSZ-13 samples characterized by different Si/Al And Cu/Al ratios, that will be discussed hereafter in Section 2.2.3, see Fig. 12.

2.1.4. Combined XANES/PXRD: highlighting the correlation between Cu(II) self-reduction and cation migration in the CHA framework. As discussed in the previous section, the in situ XAS/XES study by Borfecchia et al.[53] shed light on the evolution of the oxidation state and local environment of copper species along the two different activation procedures. Moreover, the support of DFT, allowed the use of the EXAFS spectra as an indirect tool to determine whether Cu species are located in the 8r or 6r, see Fig. 12. A direct determination of the copper location in the unit cell requires however diffraction techniques. In this regard, Andersen et al.[6] provided a detailed structural description of an O_2-activated Cu-SSZ-13 (Si/Al=15.5, Cu/Al=0.45) analyzing with iterative Rietveld analysis and maximum entropy method high-resolution synchrotron PXRD, finding that Cu cations occupied two crystallographic independent sites located in the 8r and in the 6r. The limitation of the first study by Andersen et al.[6] is however that information on the oxidation state of copper ions cannot be extracted from diffraction data.

To overcome this limitation, Andersen et al.[42] performed a new experiment on the Swiss-Norwegian beamline of the ESRF synchrotron that is equipped with two independent monochromators, allowing a rapid (about 30 s) plug and play switch between X-ray absorption and X-ray diffraction setups.[144-147] Thus both XAFS spectra and PXRD patterns (with a 2D detector) can be measured on exactly the same sample in almost the same conditions.

Using the two Cu sites determined in the previous experiment,[6] and constraining the sum of the refined Cu species to be equal to 1.08 atoms per unit cell (as determined by ICP elemental analysis) Andersen *et al.*[42] found that along the O_2-activation, there is a migration of Cu species from the *8r* into the *6r* site (black and red data, respectively in Fig. 9a) and that this phenomenon is accompanied by a partial reduction of Cu(II) into Cu(I) (violet and orange data in Fig. 9b). This reduction phenomenon occurs once virtually all water molecules have left the zeolite framework, as confirmed by the in dependent PXRD and XANES analyses, blue data in parts (a) and (b) of Fig. 9, respectively. The reduction of a fraction of Cu(II) into Cu(I), determined by linear combination analysis of the XANES data, is essential to explain how, at the end of the treatment, copper species can occupy the *6r* site with an occupancy almost twice as large as the maximum allowed for Cu(II) species on the basis of the Si/Al ratio of the investigated zeolite (15.5). The same experiment, repeated in He-atmosphere (Fig. 9c,d), resulted in a more pronounced migration of copper species from the *8r* into the *6r* site and in a total reduction of Cu(II) into Cu(I), regardless of which site is occupied.

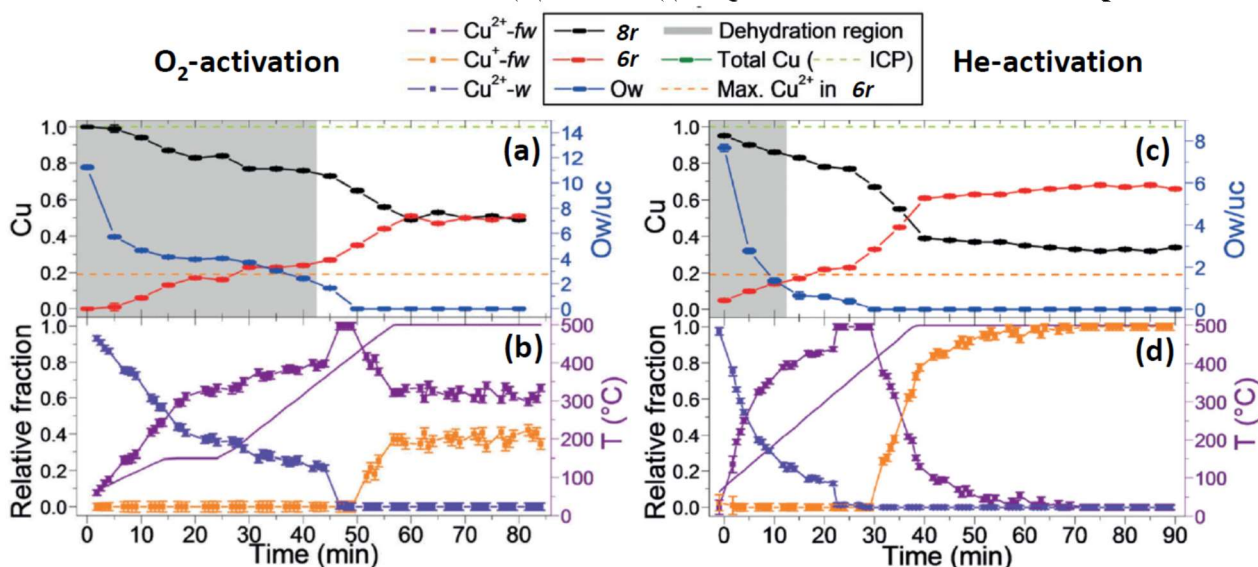Fig. 9. Part (a): Evolution of the Cu occupancies in the *8r* (black data) and *6r* (red data) sites during O_2-activation (10% O_2 in He) of Cu-CHA (Si/Al = 15.1; Cu/Al = 0.48) from the Rietveld refinement of the time-resolved synchrotron PXRD data. In all refinements, the sum of the occupancies of the two sites has been constrained to the value determined by chemical analysis (dashed vertical gray line). Also reported is the number of water molecules per unit cell optimized in the refinements (blue data). The horizontal dashed orange line represents the theoretical maximum amount of Cu(II) species that can be hosted in *6r* in a CHA framework with Si/Al = 15.5. Part (b): fraction of hydrated Cu(II) species (blue data) of Cu(II) species interacting with the zeolite framework (violet data) and of Cu(I) species interacting with the zeolite framework (orange data) as determined by the linear combination analysis of the XANES data collected almost simultaneously with the PXRD data. Parts (c) and (d): as parts (a) and (b) for the He-activation of the same sample.

Comparing the overall results of the IR experiments of CO and NO adsorption, (Section 2.1.1, Fig. 3) with the combined XANES/EXAFS/XES experiments (Section 2.1.3, Fig. 6, Fig. 7 and Fig. 8) and with the parallel PXRD/XANES study reviewed here above (Fig. 9), it emerges that all experiments are in semi-qualitative agreement and that some (minor) disagreement exists on the quantification of the fraction of Cu(I) and Cu(II) species obtained at the end of both O_2- and inert-activations. To better understand such discrepancies the next section extends the analysis of the complexity of the problem to two important variables that are the Si/Al and the Cu/Al ratios.

2.2. Composition-dependent Cu-speciation

2.2.1. Multiple cationic positions in Cu-CHA: insight and compositional trends from TPR.

As anticipated in the beginning of Section 2, the initial structural investigations on Cu-CHA zeolites[3, 93] claimed that Cu is located in a single cationic site, coordinated to three framework oxygen atoms (O$_{fw}$) just outside the *6r* plane. In particular, the study by Fickel *et al.*[93] was conducted on a Cu-SSZ-13 catalyst with Si/Al = 12 and Cu/Al = 0.35 by Rietveld refinement of temperature-dependent synchrotron XRD data. A subsequent report by Korhonen *et al.*[52] supported the previously proposed 'single-site' scenario for a Cu-SSZ-13 catalyst with Si/Al = 9 and Cu/Al = 0.18, based on *in situ* UV-

Vis and XAS data. As a consequence, the isolated Cu(II) species in *6r* identified by XRD were initially proposed as the active sites for NH_3-SCR.

This simple and elegant structural picture was however challenged by the TPR results reported by Peden and co-workers.[141] The authors performed H_2-TPR measurements on a series of Cu-exchanged SSZ-13 zeolites, with $Si/Al_2 = 12$ and exchange levels from 20% to 100%. In particular, H_2-TPR experiments performed in 2% H_2/Ar in the RT–600°C temperature range on O_2-calcinated catalysts evidenced only a single H_2 consumption peak at 340 °C for the 20% exchanged zeolite. Increasing the Cu-exchange level, an additional peak developed at 230 °C, the intensity of which increased proportionally to the Cu-loading, and was maximized at 100% Cu-exchange. As for the high-temperature peak at 340 °C, its intensity was observed to be stabilized at 40% exchange, remaining unchanged at higher Cu-loadings. These findings provided a direct proof of two different Cu(II) species/sites in SSZ-13, with Cu-loading-dependent distribution and markedly different redox barriers. In the same work, the authors also explored the effect of H_2O presence during TPR, working in 2%H_2/Ar+1% H_2O. Under these conditions, the two reduction peaks observed during 'dry' TPR would progressively shift towards each other as Cu-loading increased, coalescing finally to a single peak at 210 °C for the 100%-exchanged sample.

These findings, together with complementary evidence from FTIR spectroscopy of adsorbed CO and NO (see above the discussion of Fig. 3b,c), were interpreted with two types of Cu ions in Cu-SSZ-13: (i) Cu in highly coordinated and stable sites in the *6r*, proposed to be primarily occupied at low exchange level and associated with the high-temperature TPR peak; (ii) Cu in the large cages of the CHA framework responsible for the low-temperature H_2 consumption peak and favored at higher exchange levels. Interaction with H_2O, even in very small amounts, was suggested to cause migration of the Cu ions, driving Cu out from the *6r* site towards the large CHA cages, where it could be more easily reduced.

A subsequent study by the same research group[148] comprehensively addressed the impact of both Cu/Al and Si/Al ratios on the redox behaviour of Cu-SSZ-13 catalysts as probed by H_2-TPR. In this work, Gao *et al.* collected H_2-TPR data for a large set of samples, with Si/Al ratios of 6, 12 and 35 and several different Cu/Al ratios in the 0.06−0.44 range. Fig. 10 reports an overview of the results. The materials were analysed starting from their hydrated state ('hydrated' labels in Fig. 10) and after being pre-dehydrated in dry 5% O_2/He at 550 °C ('dehydrated' labels in Fig. 10).

The high-temperature H_2 consumption peak is favoured at low values of both Si/Al and Cu/Al ratios. It becomes almost undetectable for Si/Al = 35 catalysts, where the low-temperature peak dominates the TPR profile, irrespectively of the Cu-loading. For the hydrated catalysts a general enhancement of the low-temperature peak is observed. Notably, at high Cu/Al ratio, dehydrated samples exhibited a significant shift of the first reduction peak to lower temperature relative to the hydrated ones.

The authors also found that the total H_2 consumption for the two highest Cu loadings diminished for dehydrated samples with respect to the hydrated ones. This observation was interpreted with self-reduction of some Cu(II) already during dehydration step prior to TPR, even if the treatment was carried out in a 5% O_2 /He flow. Evidence for self-reduction of about 40% of the total Cu content during thermal treatment in diluted O_2 flow (10% O_2/He) at temperature > 450 °C was also reported by Andersen *et al.*,[42] see above Section 2.1. The integrated area of the TPR peaks for the dehydrated samples with Si/Al = 35 where connected with the highest self-reduction levels, showing a peculiar decrease of self-reduced Cu at increasing Cu-loading.
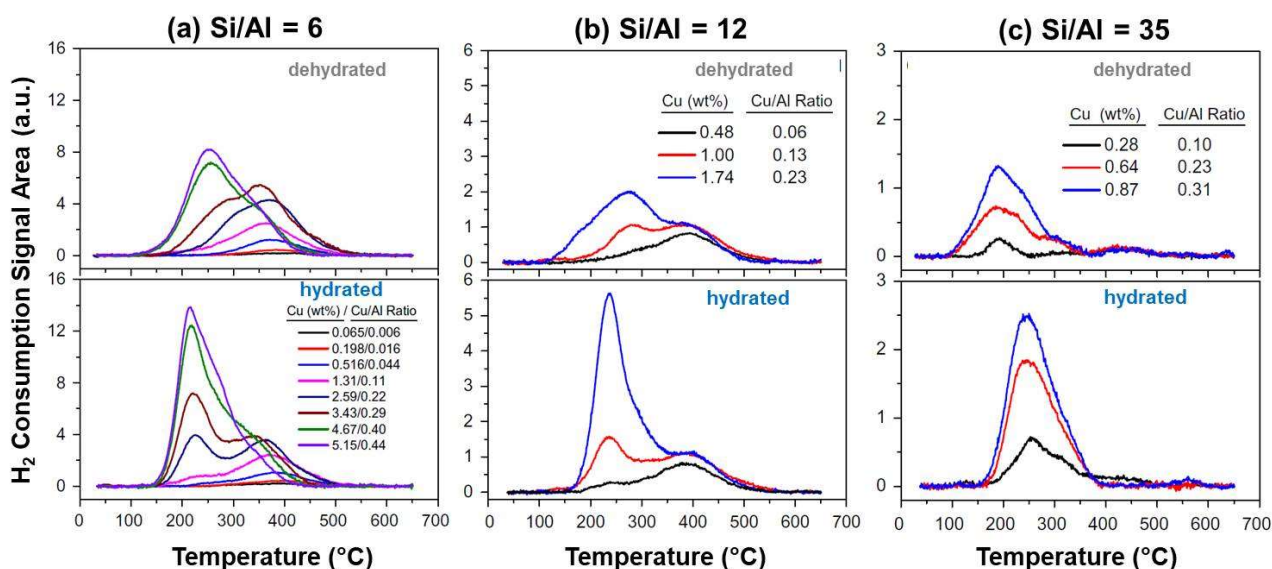
Fig. 10. H₂-TPR results for Cu-SSZ-13 samples with different Cu loadings for (a) Si/Al = 6, (b) Si/Al = 12 and (c) Si/Al = 35. Top panels report TPR for dehydrated samples while bottom panels show TPR for fully hydrated samples with the same composition. Adapted with permission from ref.[148]. Copyright 2015 Elsevier Inc.

It clearly appears that the redox-properties of the Cu-ions in Cu-SSZ-13 can be systematically tuned by modifying the compositional parameters of the material. The TPR results reviewed above point to two major Cu(II) species (or, possibly, classes of Cu(II) species). These include a redox-resistant component favoured at low Si/Al and Cu/Al values and a redox-active one, becoming more abundant at high Si/Al and Cu/Al ratios. Based on the TPR trends with composition, the redox-resistant component is consistent with bare Cu(II) species charge-balanced by two proximal Al atoms at T-sites in a *6r*, Z₂Cu(II), statistically more abundant in Al-rich frameworks, see above Eq. (1a) and related discussion. Highly stable and firmly coordinated to the framework, this site well matches the initial proposals formulated from XRD analysis. The assignment of the redox-active component, based on TPR, appears somehow more uncertain. Its composition-dependent H₂-TPR response strongly supports a Cu(II)species hosted at a *1Al* sites, where the charge balance is closed by extra-framework ligands. The Z[Cu(II)OH]⁺ complex extensively discussed in Section 2.1 represents a very plausible candidate. Nonetheless, the differences among hydrated and dehydrated conditions evidenced in Fig. 10 indicate a role of high-temperature treatment in O₂. According to Gao *et al.*[148] a reduction onset as low as 100 °C for materials pre-activated in O₂, suggests the presence of dimeric oxo-bridged Cu-species, or possibly other O₂-derived superoxo or peroxo moieties, undergoing facile reduction even at very low temperature. The formation of such types of species, already introduced in Section 2.1.2, will be further discussed in sub-section 2.2.4.

2.2.2. A compositional phase diagram for Cu-SSZ-13. The TPR results described above where paralleled by an impressive amount of characterization results on Cu-CHA materials at reference composition (typically Si/Al ~ 12–15, Cu/Al ~ 0.5, giving optimal performance in NH₃-SCR) under different activation conditions (see Section 2.1). In 2016, a milestone work from Schneider and co-workers[75] synergized theory and experiment to rationalize in a consistent picture the abundant literature that has appeared on the topic in the last years.
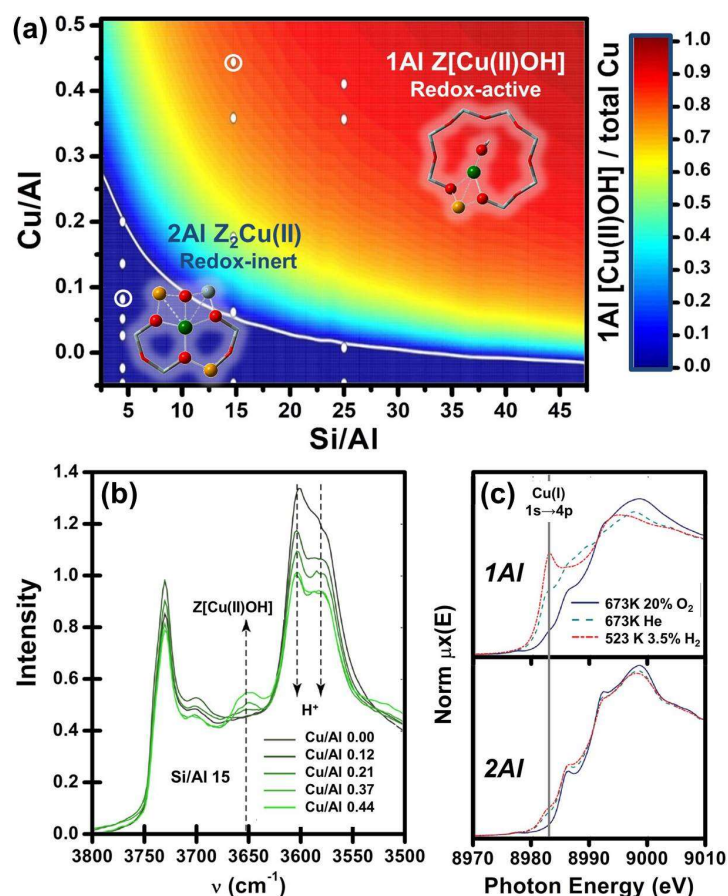
16

Fig. 11. (a) Theoretical compositional phase diagram for Cu-sites in O_2-activated Cu-SSZ-13. Color scale on the right indicates the predicted fraction of redox-active *1Al* Z[Cu(II)OH] species as a function of Cu/Al and Si/Al ratios. The white line demarcates the transition from *2Al* Z_2Cu(II)-only region to the mixed *2Al* Z_2Cu(II) / *1Al* Z[Cu(II)OH] region. Structural models of the two Cu-species are also reported (atom colour code: Cu, green; O, red; Si, grey, Al, orange; H, white). Full white dots indicates compositions of Cu-SSZ-13 samples synthetized and characterized by FTIR and acid sites titration by Paolucci *et al.* in the original work.[75] The two compositions selected as representative of Cu-species at *1Al* and *2Al* sites and further characterized by XAS, part (c), are highlighted by white circles. (b) FTIR spectra of Cu-SSZ-13 samples with Si/Al = 15 and variable Cu/Al ratio in the 0 − 0.44 range, collected at 200 °C after of O_2-activation at 400 °C. The dashed arrows indicate the increase of the fingerprint band assigned to *1Al* Z[Cu(II)OH] complexes and the simultaneous decrease of the Brønsted acid sites bands, as Cu/Al ratio increases. (c) Cu K-edge XANES spectra collected on the two samples representative of Cu-species at *1Al* and *2Al* sites (top and bottom panels, respectively) after treatment in 20% O_2 at 400 °C (solid blue lines), He at 400 °C (dashed teal lines), and in 3% H_2 at (dot-dash red lines). Adapted by permission of the American Chemical Society (copyright 2016) from ref.[75]

Firstly, the authors employed DFT to rank the stability of different Cu-species in the CHA framework. They found the free energy associated with Cu at *2Al* sites to be significantly lower than that for Cu near *1Al* at both 25 °C and 400 °C. In line with TPR findings described in Section 2.2.1 (Fig. 10), *2Al* exchange sites in *6r* are thus predicted to represent preferential locations for Cu(II) ions, over a wide interval of conditions. The Al distribution for a given Si/Al ratio in the framework was then determined by numerical simulations[149] imposing random Al siting subject to the Löwenstein's rule.[150] Based on the results of computational analysis, all the *2Al* sites available at a fixed Si/Al are assumed to be saturated, before Z[Cu(II)OH] species are formed at *1Al* sites. Under these hypotheses, the authors computed the compositional phase diagram for Cu-sites in O_2-activated Cu-SSZ-13, reported in Fig. 11a. It shows the fraction of Cu occurring as *1Al* Z[Cu(II)OH] as a function of Si/Al and Cu/Al ratios. Below the white line, *2Al* Z_2Cu(II) is predicted to be the only Cu-species present, while above the line the fraction of Z[Cu(II)OH] progressively increases, becoming largely dominant in the right top corner of the compositional plane. Bates *et al.*[151] previously computed the Cu/Al ratio required to saturate the available *2Al* sites in *6r* as a function of the Si/Al

ratio under similar assumptions. They predicted *2Al* saturation at Cu/Al ≈ 0.24, 0.09, and 0.05 for Si/Al = 5, 15 and 29, respectively.

Schneider and co-workers reported several experimental results to validate the theoretical diagram in Fig. 11a. They synthesized a large series of Cu-SSZ-13 catalysts with Si/Al = 5, 15, 25 and various Cu-loadings (full white dots in Fig. 11a). The samples were characterized by Brønsted acid sites titration as well as *in situ* FTIR (Fig. 11b) and XAS spectroscopy (Fig. 11c) for selected catalysts. Cu/H$^+$ exchange stoichiometries obtained quantifying the residual H$^+$ in the exchanged materials by NH$_3$-TPD, revealed that Cu ion exchange occurs in a sequential way: first as Z$_2$Cu(II) [Z$_2$H$_2$ + Cu(II)→ Z$_2$Cu(II) + 2H$^+$] up to saturation of available *2Al* sites and then as Z[Cu(II)OH] at *1Al* sites [ZH + Cu(II)H$_2$O→ Z[Cu(II)OH] + 2H$^+$]. Further spectroscopic evidence on this point came from the FTIR data shown in Fig. 11b. Here, the Z[Cu(II)OH] fingerprint band at ca. 3650 cm^{-1} (see also Section 2.1) remains undetected until a threshold in Cu-loading is reached, corresponding to Cu/Al = 0.21 for the investigated samples with Si/Al = 15. For Cu/Al > 0.21, a progressive increase in the 3650 cm^{-1} band intensity is observed. Complementary insights were obtained by monitoring the characteristic vibrations of Brønsted sites at 3605 and 3580 cm^{-1}.[63, 152] In particular, by comparing the integrated peak areas for these two bands in the Cu-exchanged and protonic zeolites, a 2:1 H$^+$/Cu ratio was found until Cu/Al = 0.12, while a 1:1 H$^+$/Cu was determined for Cu/Al ≥ 0.21.

In situ XAS finally allowed the authors to directly probe the redox behaviour and local coordination environment of Cu for two selected compositional points (white circles in Fig. 11a), representative of *1Al* and *2Al* Cu-species. Fig. 11c shows the Cu K-edge XANES spectra for the two catalysts collected after high-temperature treatment under oxidant (20% O$_2$/He) and reducing atmosphere (both He and diluted H$_2$). While treatment in oxygen results in a largely dominant Cu(II) oxidation state in both the samples, their response to reducing conditions is drastically different. The *2Al* sample only undergoes very minor modifications, preserving the characteristic Cu(II) XANES features even in H$_2$. Conversely, the *1Al* sample undergoes substantial reduction after treatment in both He (self-reduction process) and H$_2$. Corresponding EXAFS spectra collected for *1Al* and *2Al* samples in O$_2$ and He were in qualitative agreement with the model structures of Z[Cu(II)OH]/ZCu(I) (O$_2$/He) and Z$_2$Cu(II) (both O$_2$ and He), respectively.

2.2.3. Further spectroscopic validation, quantification and deviations from the ideal picture. Overall, the results reviewed in the previous section represent a qualitative fundamental contribution to our current understanding of composition-dependent Cu-speciation in Cu-SSZ-13. Redox-active Z[Cu(II)OH] and redox-inert Z$_2$Cu(II) species emerge as the two key players in the field, with the latter preferentially stabilized at low values of both Si/Al and Cu/Al ratios, due to statistical availability of suitable *2Al* docking sites and more favourable energetics. However, open questions remained on how these framework-interacting Cu-species are formed from the fully hydrated Cu(II) aquo complexes known to dominate in the as-prepared materials (see Section 2.1). Even more important, the need for a more quantitative evaluation of the experimental results was highly desirable since this was often hampered by the co-existence of several rather similar species.

Aiming at a comprehensive experimental exploration of the composition effects on Cu-speciation and (self-) reducibility in Cu-CHA, Martini *et al.*[59] monitored by *in situ* XANES the He-activation process from room temperature (RT) to 400 °C on a series of six Cu-SSZ-13 samples with Si/Al ratios in the 5–29 range and Cu/Al ratios from ∼ 0.1 to ∼ 0.6. Thermal treatment in inert atmosphere was preferred in order to achieve a better spectroscopic contrast between redox-active and redox-resistant Cu-sites, as well as to gain deeper insights in the self-reduction process. High-quality EXAFS spectra on the whole sample series were also collected upon stabilization at 400 °C in He.

Principal component analysis (PCA) of the *in situ* XANES dataset in Fig. 12a revealed the presence of five principal components (PCs). Thus, the authors applied a multivariate curve resolution (MCR) procedure, based on alternating least square (ALS) method[153-155] to extract chemically meaningful spectra (Fig. 12b) and concentration profiles (Fig. 12c) of the five 'pure' Cu-species highlighted by PCA, as a function of temperature and compositional parameters.

The theoretical XANES spectra obtained from MCR-ALS are in excellent agreement with previous XAS studies on Cu-SSZ-13.[53, 58, 75, 156.] Based on the spectroscopic fingerprints of each theoretical XANES component and the corresponding temperature-dependent concentration profiles, it was possible to reliably assign each pure spectrum to the Cu-species shown in Fig. 12d. The assignment was further corroborated by XANES simulations computed from the DFT-optimized geometries of the proposed Cu-species. Notably, the MCR spectra attributed to Z[Cu(II)OH] and Z_2Cu(II) (black and orange curves in Fig. 12b, respectively) are in perfect agreement with the XANES reported by Paolucci *et al.*[75] for O_2-treated catalysts representative of Cu at *1Al* and *2Al* sites, shown here in Fig. 11c.
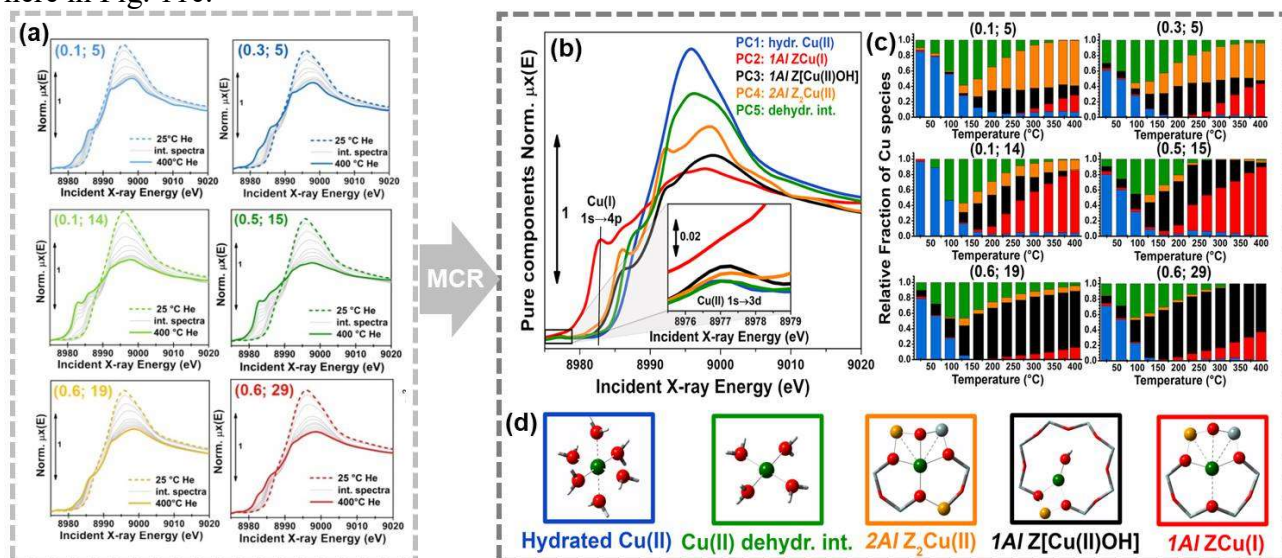

Fig. 12. (a) Experimental temperature-dependent *in situ* XANES spectra collected on six Cu-SSZ-13 samples with different composition (denoted by (Cu/Al; Si/Al) labels) during thermal treatment from 25 to 400 °C (heating rate: 5 °C/min) in 100 ml/min of pure He. Thick dashed lines: starting spectrum at RT; grey thin lines: intermediate states during thermal treatment, thick solid lines: final state at 400 °C. The global dataset includes 72 spectra. (b) Theoretical XANES spectra of the five pure components derived from MCR-ALS analysis. The inset reports a magnification of the pre-edge region in the theoretical spectra. (c) Bar plots reporting temperature-dependent concentration profiles of pure species for the six investigated compositional points. (d) Proposed assignment of the five pure components to specific Cu-species/sites formed in the catalyst as a function of composition and activation temperature. Atom colour code in the structures: Cu, green; H, white; O, red, Si, grey; Al, yellow. In parts b-d, the same colour code is used to indicate the identified pure Cu-species. Unpublished Figure, reporting data previously published in ref.[59].

These results demonstrated the potential of XAS spectroscopy combined with multivariate data modelling in tackling the structural complexity associated with Cu-speciation in Cu-CHA. Moreover, the study provided novel insights into the temperature/time-dependent dynamics yielding to framework interacting Cu-sites in the cages of the CHA zeolite during the dehydration process. In particular, the formation of framework-interacting Cu-species from the mobile Cu(II) aquo-complexes present at RT is observed to occur via a four-coordinated Cu(II) dehydration intermediate, peaking around 130 °C (green curve and bars in Fig. 12b,c). Then, Z[Cu(II)OH] and Z_2Cu(II) species progressively develop, with relative abundance determined by composition. Z[Cu(II)OH] peaks appear around 200 °C and thereafter progressively decrease, in favour of self-reduced ZCu(I) species. Conversely, Z_2Cu(II) sites, dominant at Si/Al = 5 and favored by low Cu/Al values, reach a steady population in the 200–300 °C range and remain stable until 400 °C. Cu-speciation at 400 °C can be described for all samples as a combination of redox-active Cu-species at *1Al* sites (in their oxidized, Z[Cu(II)OH], or reduced, ZCu(I), form) and redox-inert Z_2Cu(II) species at *2Al* sites in *6r*, as independently validated by DFT-assisted multi-component EXAFS fits in the original work.[59]

The quantitative knowledge of Cu-speciation enabled from MCR analysis of *in situ* XANES provided further spectroscopic support to the compositional phase diagram by Paolucci *et al.*[75] However, it also highlighted intriguing deviations from the ideal picture, herein examined in critical comparison with other recent results appeared in the literature.

2.2.3.1. Composition impact on self-reducibility and nature of ZCu(I) species. A first consideration concerns the redox behavior observed by Martini *et al.*[59] for Cu-SSZ-13 with Si/Al = 19 and 29. Not surprisingly, at such high Si/Al ratios, redox-resistant $Z_2Cu(II)$ species represent a minor contribution to Cu-speciation, becoming barely detectable at Si/Al = 29 (Fig. 12c). Although in these catalysts Cu-speciation is dominated by Z[Cu(II)OH] species, it appears that, at such high Si/Al values, self-reduction to ZCu(I) is hampered. These evidences suggest that proximity and spatial distribution of Z[Cu(II)OH] complexes and Brønsted sites within the CHA framework could represent a critical factor in the self-reduction mechanism. The global picture about the composition impact on self-reducibility in Cu-SSZ-13 for the key compositional points investigated by Martini *et al.*[59] is summarized in Fig. 13a. The bar plot reports the fractions of Cu-species evaluated from MCR-ALS analysis of the XANES spectra collected 400 °C in He, at the end of the thermal treatment.

At low Si/Al, redox-resistant $Z_2Cu(II)$ species dominates the speciation, while at high Si/Al self-reduction of Z[Cu(II)OH] only occurs to a limited extent. Consequently, the catalyst self-reducibility, quantified by the measured fraction of ZCu(I), reaches an optimum at intermediate Si/Al ~ 15, and it is overall promoted by high Cu/Al ratios.
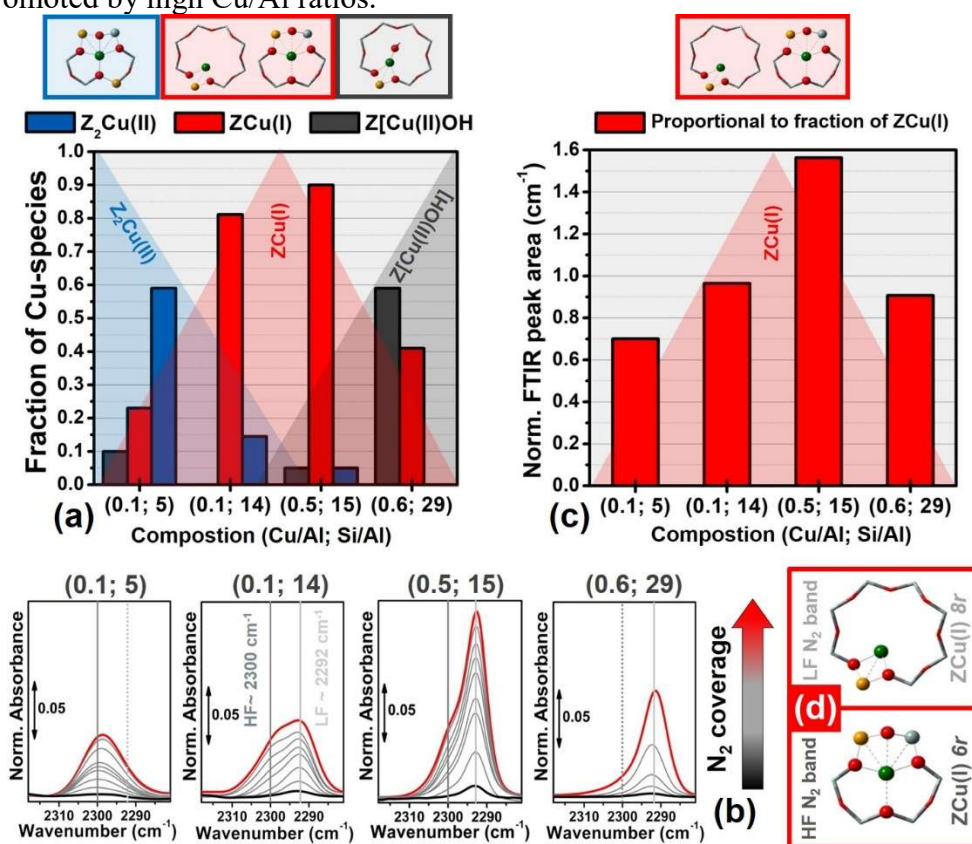
Fig. 13. (a) Bar plot summarizing Cu-speciation evaluated from MCR-ALS analysis of the *in situ* XANES spectra collected 400 °C in He for selected Cu-SSZ-13 samples with different composition, indicated by (Cu/Al; Si/Al) labels. (b) Low temperature (~ −160 °C) normalized IR spectra of N_2 dosed ad increasing equilibrium pressure (from 10^{-2} to 5 Torr; 1 Torr = 133.3 Pa) on the same set of samples considered in part (a), after thermal treatment in vacuum at 400 °C. Black, red and light grey curves refer to lowest, highest and intermediate N_2 coverage, respectively. Vertical lines indicate the two IR bands assigned to Cu(I)/N_2 adducts: low-frequency (LF) band at 2292 cm^{-1} in light grey; high-frequency (HF) band at 2300 cm^{-1} in grey. (c) Bar plots reporting the normalized areas of the N_2/Cu(I) IR bands measured at the highest coverage. (d) DFT-optimized models for *1Al* ZCu(I) in *8r* (top) and *6r* (bottom) connected with the LF and HF components detected in the IR spectra in part (b); atom color code: Cu, green; H, white; O, red; Si, grey; Al, yellow). Unpublished Figure, reporting results previously published in ref.[59].

Further insights into the abundance and the nature of ZCu(I) species were obtained by *in situ* IR spectroscopy of adsorbed N_2 on the same series of Cu-SSZ-13 samples. The N_2 probe molecule selectively forms Cu(I)/N_2 adducts, stable at liquid nitrogen temperature, ~ −160 °C.[45, 65] Although several precautions should be taken in the comparison with XAS results (different experimental conditions, *i.e.* thermal treatment in He gas flow *vs* vacuum and data collection at different

temperature; differences in the extinction coefficients for different IR bands), the integrated areas of the two bands assigned to Cu(I)/N$_2$ adducts (see Fig. 13b and discussion below), after appropriate normalization for the total Cu content in the samples, can be semi-quantitatively correlated with the fraction of ZCu(I) formed though self-reductive pathways. As shown in Fig. 13c, IR results qualitatively confirm the composition ↔ self-reducibility trend observed from XANES MCR analysis, with a maximum in ZCu(I) abundance at intermediate Si/Al.

The IR results reported in Fig. 13b also provided a further confirmation of two distinct ZCu(I) sites in Cu-SSZ-13, in agreement with the early report by Dĕdeček et al.[157] Indeed, being a weakly interacting probe, N$_2$ enables discrimination even between very similar adsorption sites.[62, 63, 158] These subtitle differentiation can be hardly obtained using more strongly interacting probe molecules such as CO[65] and NO,[65, 159] as well as using conventional XAS. In agreement with previous studies on a *vacuum* activated Cu-SSZ-13 sample with Cu/Al ~ 0.44 and Si/Al ~ 13,[65] the spectra exhibit two components: a (generally) predominant low-frequency (LF) band at 2292 cm^{-1} (light grey vertical lines in Fig. 13b) with a high-frequency (HF) shoulder at 2300 cm^{-1} (grey lines in Fig. 13b). In line with the recent quasi-simultaneous XANES/PXRD study by Andersen et al.,[42] (see Section 2.1), the two components were assigned by Martini et al. to ZCu(I) species in the *6r* (HF component) and *8r* (LF component), depicted in Fig. 13d.

In the context of this Section about composition-dependent Cu speciation, it is important to note that the relative intensities of the two Cu(I)/N$_2$ IR bands vary in the set of samples, indicating an influence of the compositional parameters on Cu(I) siting. In particular, at Si/Al = 5, the HF component appears dominant with respect to the LF one. Conversely, at Si/Al = 29, the LF band is largely more developed than the HF one. For the samples with Si/Al = 14, 15 both components are clearly visible but the LF band is significantly enhanced at high Cu/Al.

These evidences of a non-monotonous redox behaviour as a function of the Si/Al ratio were confirmed by Pappas et al.,[33] while investigating structure-activity relationship for the MTM conversion over Cu-SSZ-13 (see also Section 3.2). However, they seem in contrast with the previously discussed H$_2$-TPR results by Gao et al.[148] reporting efficient low-temperature reduction in Si/Al = 35 catalysts (Fig. 10c). Nonetheless one has to consider the different conditions – self-reduction in inert atmosphere and reduction by H$_2$ during TPR (which indeed resulted in different XANES spectra as reported by Paolucci et al.,[75] see Fig. 11c). Overall, the data shown in Fig. 13, might hint towards the participation of an adjacent Brønsted acid site in the self-reduction process of neighbouring Cu-sites, as well as towards cooperative routes involving proximal Z[Cu(II)OH] species. In any case the data demonstrates that the redox-behaviour in high Si/Al-ratio Cu-zeolites deserves further investigation, which hopefully results in a conclusive understanding of self-reduction mechanism in Cu-zeolites.

2.2.3.2. Saturation of 2Al sites and nature of Z$_2$Cu(II) species. A second consideration arises in connection with the hypothesis of *2Al* sites saturation. The high reducibility observed by Martini et al.[59] for the low-loading sample (Cu/Al = 0.1) with Si/Al = 14 contrasts with the *2Al* saturation scenario. Indeed, according to the compositional phase diagram in Fig. 11a[75] and the saturation threshold predicted by Bates et al.,[151] this composition should result into > 90% of redox-resistant Z$_2$Cu(II). Conversely, MCR analysis revealed that the Z$_2$Cu(II) contribution only reaches a maximum fraction of ~ 18% total Cu in the final state at 400 °C in He. From the concentration profiles reported in Fig. 12c, it is clear that there exists a preference in the stabilization of Z$_2$Cu(II) species at low Cu-loading: for the same Si/Al ratio, a lower Cu/Al results in a higher contribution from Cu at *2Al* sites. Nonetheless, these results do not support an ideal sequential exchange, first into *2Al* sites up to saturation and only after into *1Al* ones. The populations of Z$_2$Cu(II) and Z[Cu(II)OH] are rather observed to grow simultaneously as temperature increases.

Other recent reports also highlighted the possibility that Z[Cu(OH)] can be populated before saturation of the available *2Al* sites in *6r*.[90, 160] As pointed out in the recent review by Gao and Peden,[94] Z[Cu(OH)], although disfavored by thermodynamics, can plausibly be *kinetically* stabilized along

dehydration. In this respect, both composition and specific conditions (heating rate, activation temperature and dwell time, etc…) are envisaged to play a crucial role. Indeed, according to Luo *et al.*,[160] a kinetically stabilized, metastable state of the catalyst is expected to convert to a thermodynamically stable state, if the system is left to relax for a sufficient time at appropriate conditions. Indeed, recent works proved that during mild hydrothermal aging of state-of-the-art Cu-SSZ-13 catalysts for NH_3-SCR, a gradual migration Z[Cu(OH)] species occurs, accompanied by their conversion into Z_2Cu(II), while consuming a Brønsted acid site according to the reaction: $Z[Cu(II)OH] + ZH \rightarrow Z_2Cu(II) + H_2O$.[90, 160] Further experimental support to these considerations came from the *in situ* EPR results reported by Gao *et al.*[94, 161] for a Cu-SSZ-13 sample with Si/Al = 6 and Cu/Al = 0.032 during dehydration in dry N_2 (Fig. 14a). Based on the compositional characteristics and the previously mentioned thermodynamic arguments, in this sample Cu should exclusively be exchanged at *2Al* sites as Z_2Cu(II). Nevertheless, a pronounced loss of signal intensity is observed along the dehydration process, particularly evident at 150 °C (red curve in Fig. 14a). The transient loss of EPR signal at intermediate temperature during dehydration points to the transient stabilization of Z[Cu(II)OH] species, proposed to be EPR silent due to *pseudo* Jahn-Teller effect[86] (see also Section 2.1). At higher temperatures, the EPR intensity is observed to recover, resulting in the characteristic spectrum of EPR-active Z_2Cu(II) species at 250 °C.
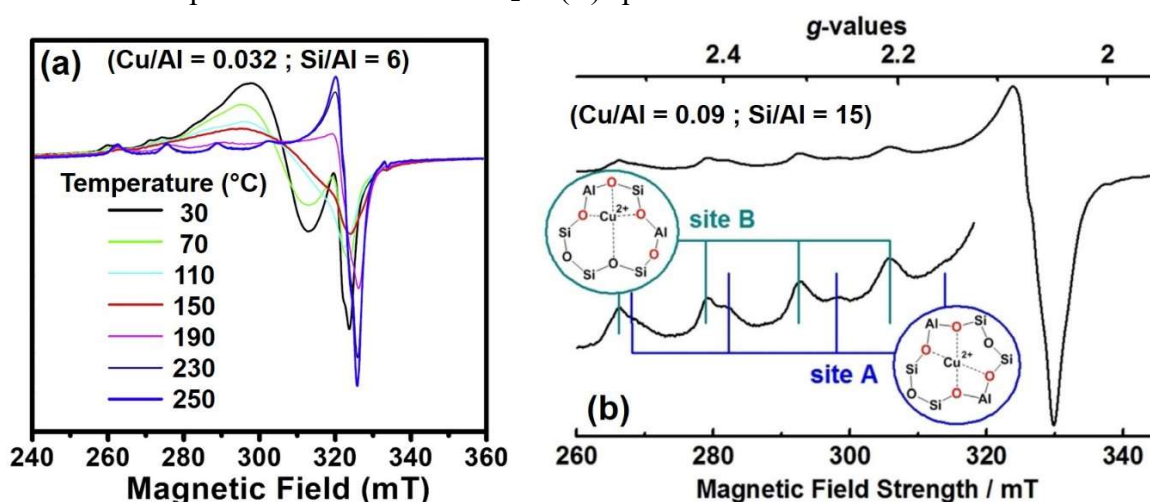

Fig. 14. (a) EPR spectra of a Cu-SSZ-13 sample (Cu/Al = 0.032; Si/Al = 6) during dehydration in N_2 from 30 °C to 250 °C. Adapted by permission of Elsevier (copyright 2014) from ref.[161] (b) EPR spectrum (measured at 200 °C) of a Cu-SSZ-13 sample (Cu/Al=0.09; Si/Al = 15) after dehydration at 250 °C in 10% O_2/He. The inset reports a magnification of the parallel region of the spectrum and the assignment of the feature to two different sites for Z_2Cu(II) species in *6r*, characterized by Al–Si–Al (site A) and Al–Si–Si–Al (site B) linkages. Reproduced by permission of Wiley-VCH (copyright 2018) from ref.[88]

Notably, EPR also directly proved that additional complexity exists in connection with Z_2Cu(II) species in the *6r* of the CHA framework. Subject to the Löwenstein's rule,[150] *6r*s with both –Al–Si–Al– and –Al–Si–Si–Al– linkages are possible. According to DFT models, these two configurations yield inequivalent Cu local environments (site B and site A in Fig. 14b, respectively). However, the structural and electronic similarity of the two Z_2Cu(II) sites, together with the averaged character of the technique, complicates their conclusive discrimination with XAS[53, 59]. In this respect, EPR provides the highest sensitivity. An example, from the recent study by Godiksen *et al.*,[88] is reported in Fig. 14b. The EPR spectrum collected on a Cu-SSZ-13 sample with Cu/Al = 0.09, Si/Al = 15 after dehydration at 250 °C in 10% O_2/He clearly shows two sets of signals in the parallel region, consistent with the Z_2Cu(II) structural models in *6r* with –Al–Si–Al– and –Al–Si–Si–Al– motifs.

Composition also appears to influence the relative population of sites A and B. In the EPR spectrum collected by Gao *et al.*[161] at 250 °C for a Cu-SSZ-13 sample with Si/Al = 6 and Cu/Al = 0.032 (in Fig. 14a, blue line), only the parallel hyperfine quadruplet assigned to site B is visible. The spectrum reported in Fig. 14b (Cu/Al = 0.09; Si/Al = 15) has been instead modelled with 72% and 20% total Cu in sites B and A, respectively. Moreover, for a Cu-SSZ-13 catalyst with Cu/Al = 0.44,

Si/Al = 13 the same authors reported a balanced contribution from sites A and B (9% total Cu for each site), after dehydration at 250 °C in 50% O_2/He. DFT calculations predicted a slightly more efficient stabilization of bare Cu(II) sites in *6r* with –Al–Si–Si–Al– linkages[75, 159] (site A in Fig. 14b). Indeed, in the detailed DFT/FTIR study by Zhang *et al.*,[159] the author distinguished two bands assigned to Z_2Cu(II)-NO adducts: a sharp band at 1948 cm^{-1} (very intense at Si/Al = 6 and 12, almost undetectable at Si/Al = 35) with an additional component at 1932 cm^{-1}. In view of the computational results, the latter was connected with Z_2Cu(II) species hosted in less energetically-favored *6r*s with –Al–Si–Al– linkages (site B). However, EPR results reviewed above seem to indicate that site B is instead the one to be preferentially populated at low Cu-loading. It is finally worth to mention that Godiksen *et al.* also evidenced a possible site-sensitive reactivity, connecting site A with a higher reactivity than site B towards oxidation in SCR-relevant mixtures.[88]

2.2.4. Composition impact on Cu(II) species other than Z[Cu(II)OH]. As discussed in Section 2.1.2, there are evidences for the formation of mono- and multi-nuclear Cu(II) species other than Z[Cu(II)OH] under high-temperature oxidative treatment of high-loading Cu-SSZ-13 materials with Si/Al ratio in the 13–20 range.[31, 33, 35, 65, 162, 163] In this respect, the most sensitive techniques are UV-Vis-NIR and Raman spectroscopy, whereas FTIR in the υ(OH) region can be employed indirectly to track the temperature-dependent dynamics of Z[Cu(II)OH][33] through its fingerprint band at ca. 3650 cm^{-1}.[38, 53, 65, 75, 129]

Here we provide a brief overview on a few reports where these techniques have been applied to Cu-SSZ-13 samples with different composition. Therein, we derive some considerations on the impact of composition on the possible stabilization of Cu-oxo species, as well as on the interpretation of the relevant spectroscopic results.

Bates *et al.*[151] used diffuse-reflectance (DR) UV-Vis-NIR spectroscopy to characterize, in their hydrated state, a series of Cu-SSZ-13 samples with Si/Al = 5 and Cu/Al ratios increasing from 0.02 to 0.35. Until Cu/Al = 0.2, the materials exhibited the characteristic UV-Vis spectrum of hydrated Cu(II) species, with broad and weak Cu(II) d–d transitions from 6000 to 17000 cm^{-1}, linearly growing in intensity with Cu-loading, a shoulder at 35000 and main feature at 45000 cm^{-1} assigned to ligand-to-metal charge transfer transitions from O ligands to Cu(II) d-orbitals.[65, 151] However, for Cu/Al = 0.35, the d–d transition intensity decreased with respect to the Cu/Al = 0.2 sample and shoulders at 20000 and 32000 cm^{-1} appeared in the spectrum, which were related to the presence of (SCR-inactive) Cu-oxide clusters formed in the as-prepared samples.

Moving from the hydrated to the activated state of the catalyst, a conclusive interpretation of the DR UV-Vis spectra in Cu-SSZ-13 is still missing, especially concerning the characteristic 'quadruplet' dominating the d–d transitions region (see Section 2.1.2).

Based on the abundant literature available on other Cu-zeolites, such as Cu-MFI and Cu-MOR,[73, 85, 164-167] the absorption bands occurring in the 25000−35000 cm^{-1} range for O_2-activated Cu-CHA should be related to the formation of redox-active Cu-oxo species other than Z[Cu(II)(OH)].

Some novel insights concerning this point can be obtained by the analysis of the DR UV-Vis spectra recently reported by Ipek *et al.*[31] for Cu-SSZ-13 treated at 450 °C in O_2 at three representative compositions, namely (Cu/Al = 0.39; Si/Al = 5); (Cu/Al = 0.4; Si/Al = 12); (Cu/Al = 0.18; Si/Al = 12). The spectra are shown in Fig. 15, together with pictures of the corresponding O_2-activated materials.
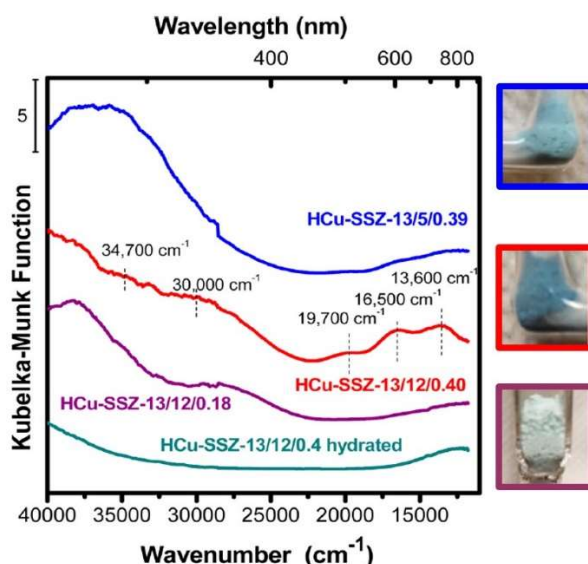
Fig. 15. (a) DR UV-Vis spectra of Cu-SSZ-13 samples with different composition after O_2 treatment at 450 °C. Blue line: (Cu/Al = 0.39; Si/Al = 5); red line: (Cu/Al = 0.4; Si/Al = 12); purple line (Cu/Al = 0.18; Si/Al = 12). The spectrum of the (Cu/Al = 0.4; Si/Al = 12) sample in its hydrated form is also reported for comparison (green line). The feature at 28500 cm^{-1} is an artifact caused by a lamp switch in the spectrometer. The pictures of the samples at 25 °C after 450 °C O_2 treatment are reported, within frames using the same colour code as for the corresponding spectra. Adapted by permission of the American Chemical Society (copyright 2017) from ref.[31]

A first observation relates to the dependence of the shoulders observed at 30000 and 34700 cm^{-1} on composition, especially Si/Al ratio. As shown in Fig. 15, these bands in the CT region are much more pronounced in the two Si/Al = 12 samples compared to the Si/Al = 5 sample. Notably, the latter has more than twice the Cu concentration of the high Cu-loading Si/Al = 12 material. Hence, it is clear that the formation of Cu-species giving rise to these spectral fingerprints is largely disfavoured in a Al rich framework, which should contain a larger fraction of redox-resistant $Z_2Cu(II)$ at *2Al* sites. Well-defined bands around 30000 cm^{-1} are also absent in UV-Vis spectra of O_2-activated Cu-SSZ-13 samples reported by Wulfers et al.[28](Cu/Al=0.35, Si/Al = 6) and by Korhonen et al. (Cu/Al = 0.18, Si/Al = 9); however, in the latter case the poor signal-to-noise ratio of the data in the CT region hampers a detailed analysis.

These results are consistent with the general picture outlined by Pappas et al.,[33] where Z[Cu(II)OH] complexes efficiently undergoing self-reduction are proposed as possible precursors to different Cu-oxo moieties (see also Section 2.1.2). These include trans-(μ-1,2-peroxo) dicopper(II) and mono(μ-oxo) dicopper(II) species, characterized by high stability in the CHA framework (chemical potential of the Cu atoms μ_{Cu} within 5 kJ/mol from the μ_{Cu} value computed for the most stable Z[Cu(II)OH] species, according to DFT calculation by Ipek et al.[31]). The characteristic Raman vibrations of these dimeric species were also identified in the (Cu/Al = 0.4; Si/Al = 12) sample described above[31] and in a different Cu-SSZ-13 material with comparable composition (Cu/Al = 0.5; Si/Al = 15).[33]

The comparison among the samples reported in Fig. 15 can also provide insightful indications about the origin of the spectral features occurring in the lower-energy portion of the UV-Vis spectrum. In particular, the bands at 13600, 16500, and 19700 cm^{-1} (belonging to the characteristic 'quadruplet' already described in Section 2.1.2) are well visible in the Cu/Al = 0.4; Si/Al = 12 sample, giving to this material a deep blue colour. Conversely, these bands can hardly be recognized in the other two Al-rich samples, which indeed show a paler blue color. The fact that, despite the higher Cu concentration, the quadruplet is significantly less developed in the Si/Al = 5 sample seems to contrast with its previous assignment to the EPR-active $Z_2Cu(II)$ species in *6r*.[86] Indeed, as noted before, this composition should be most favourable for $Z_2Cu(II)$ species among the investigated ones. In light of these and other evidences, the assignment of the Cu-SSZ-13 quadruplet still represents an open research question.

3. Structure reactivity correlation

3.1. Selective Catalytic Reduction of NO_x by Ammonia

The selective catalytic reduction of NO_x to N_2 by ammonia (NH_3-SCR) has played an important role in the abatement of NO_x emissions in the exhausts of diesel engines and power plants since the 1970's. To date, the preferred catalysts for stationary NH_3-SCR are based on supported vanadium oxides.[168-176] However, for mobile applications, the reaction conditions are highly dynamic and the strongly varying temperatures and gas flow rates of the lean-burned exhaust gases required a new type of catalyst that would combine a high activity at low temperatures (<300 °C) with hydrothermal stability at elevated temperatures (>500 °C).[177, 178] Over several decades many metal loaded zeolites where tested for diesel automotive applications,[179-184] but the commercialization of the NH_3-SCR technology based on zeolites had to wait until the discovery of the Cu-CHA system.[16-27] In the following we will summarize the current state of understanding of how the Cu-speciation in Cu-CHA relates to the catalytic performance in NH_3-SCR.

In the so-called *standard* NH_3-SCR, NO reacts with ammonia and oxygen to form nitrogen and water, according to the equation[24, 76, 77, 184, 185]

$$4\,NO + 4\,NH_3 + O_2 \rightarrow 4\,N_2 + 6\,H_2O \ . \tag{3}$$

As described in Section 2, the Cu-speciation in Cu-CHA is strongly dependent on the catalyst activation, composition, temperature and gas composition. Hence, it is likely that also the structures of the active Cu sites in SCR catalysts differ for different catalyst compositions and undergo dynamic changes during SCR operation.

When considering NH_3-SCR over Cu-CHA, it is important to highlight that the NO conversion typically shows a bimodal pattern, with a first maximum around 300 °C and a second maximum around 400 °C.[27, 161] The observed *dip* in conversion at around 350 °C has been proposed to be related to a change in the SCR mechanism. It is therefore interesting to consider the Cu speciation before and after the *dip*.

In order to experimentally establish structure reactivity correlations, *in-situ* and *operando* spectroscopic methods in the presence of reactant molecules at relevant reaction conditions, have proven to be a powerful tool. In particular, the reaction has been followed, as a function of the temperature, by *operando* X-ray absorption (in both XANES, Fig. 16a, and EXAFS, see Fig. 16b regions) and X-ray emission (Fig. 16a) spectroscopies.[39] The unique element and ligand sensitivity of the combined XAS/XES approach techniques allowed Lomachenko *et al.* to shed light on the evolution of the different Cu species inside the Cu-CHA catalyst 'in action' during *operando* NH_3-SCR experiments in the 150-400 °C range (Fig. 16d,e).
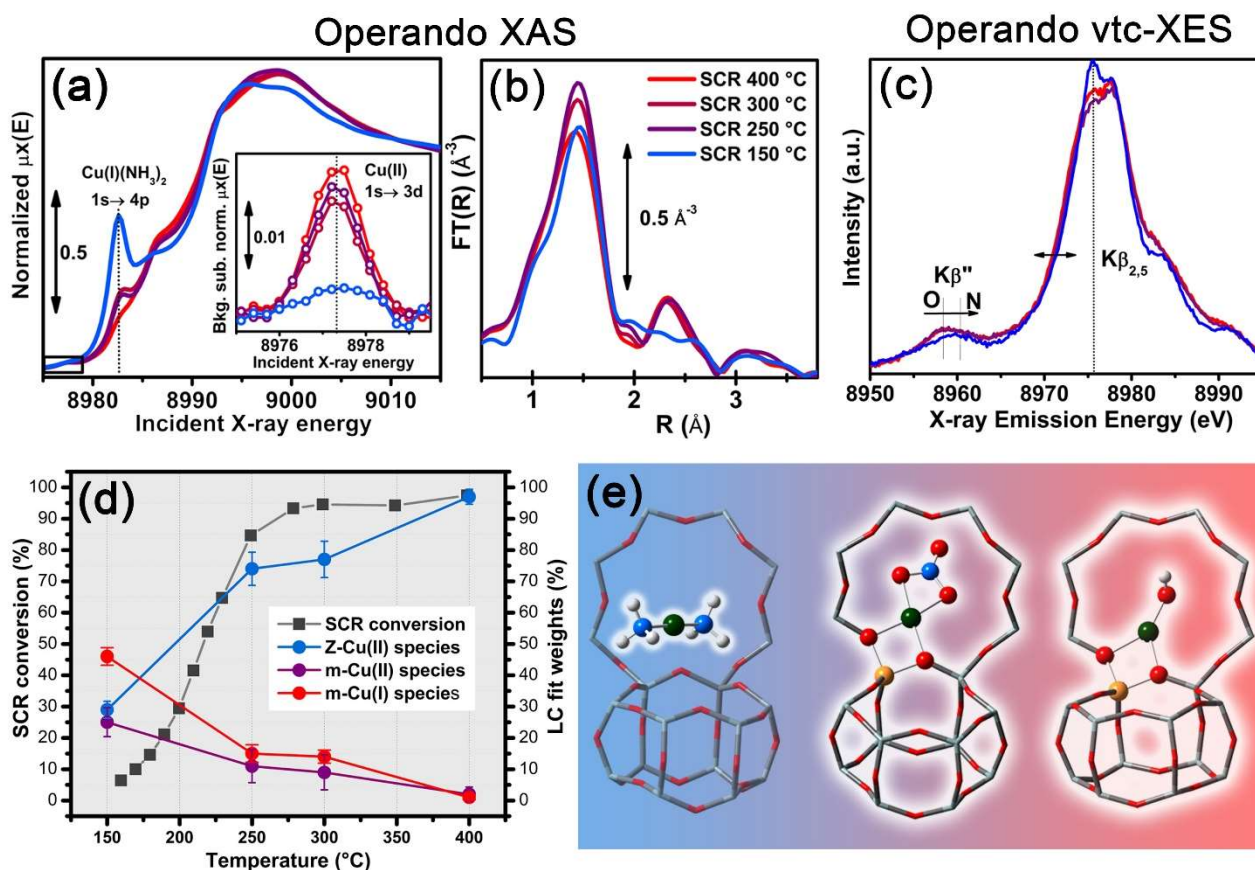
Fig. 16. Part (a): Cu K-edge XANES spectra collected during *operando* NH₃-SCR at different temperatures: 150, 250, 300 and 400 °C. The inset reports a magnification of the background-subtracted Cu(II) 1s → 3d pre-edge peaks (black boxes in the main panel). Part (b): as part (a) for the moduli of the, k^2-weighted, FT of the corresponding EXAFS spectra. Part (c): as part (a) for the (Kβ-main)-subtracted Kβ" and Kβ₂,₅ XES satellite peaks. Part (d): Cu-speciation during temperature-dependent SCR on Cu-CHA from LCF analysis of *operando* XANES spectra (colored circles, right axis) and NH₃-SCR conversion rate (black squares, left axis). Part (e): Structural snapshots of the dominant Cu-species for each probed temperature: mobile $[Cu(I)(NH_3)_2]^+$ complexes in the low-temperature range and framework-coordinated Cu(II) moieties in the high-temperature range (color code: Cu: green, O: red, Al: yellow, Si: gray, N: blue, H: white). Previously unpublished figure reporting spectra published in Ref.[40]

More in detail, by applying a linear combination fit (LCF) analysis of *operando* XANES, Fig. 16a, employing a series of well-characterized Cu-references it was possible to quantitatively estimate temperature-dependent Cu-speciation during SCR (Fig. 16e). The results were validated by complementary *operando* EXAFS (Fig. 16b) and valence-to-core-XES (Fig. 16c), which allows distinction between O- and N-ligation at the Cu-atom. *Operando* XAS/XES during SCR revealed a strong influence of reaction temperature on Cu-speciation. In the low-temperature range up to *ca.* 200 °C the catalyst framework hosts balanced populations of Cu(I)/Cu(II) sites, with a dominant presence of mobile, NH₃-solvated Cu-species. The formation of these mobile species had already been observed by Giordanino *et al.*[58] during low temperature interaction of Cu-CHA with gaseous NH₃ alone. In the 250-400 °C range, the local coordination of the metal ion changes: Cu loses part of the NH₃ ligands and is dominantly present as framework-coordinated Cu(II) species, with preferential O-ligation, accounting for ca. 70% to more than 90% of total Cu sites (XES in Fig. 16d). Importantly, the transition between low- and high-temperature Cu-speciation coincides with the slight dip in NO conversion at around 350 °C (Fig. 16d, black squares) and indicates that the NH₃ ligand loss and subsequent formation of a zeolite bound Cu-species induces the observed change in SCR kinetics and related mechanistic steps.

The experimental results obtained by Lomachenko *et al.*,[40] are in good agreement with the theoretically calculated phase diagrams for Cu-CHA at different compositions and reaction conditions, obtained by Paolucci *et al.*,[75] see Fig. 17.
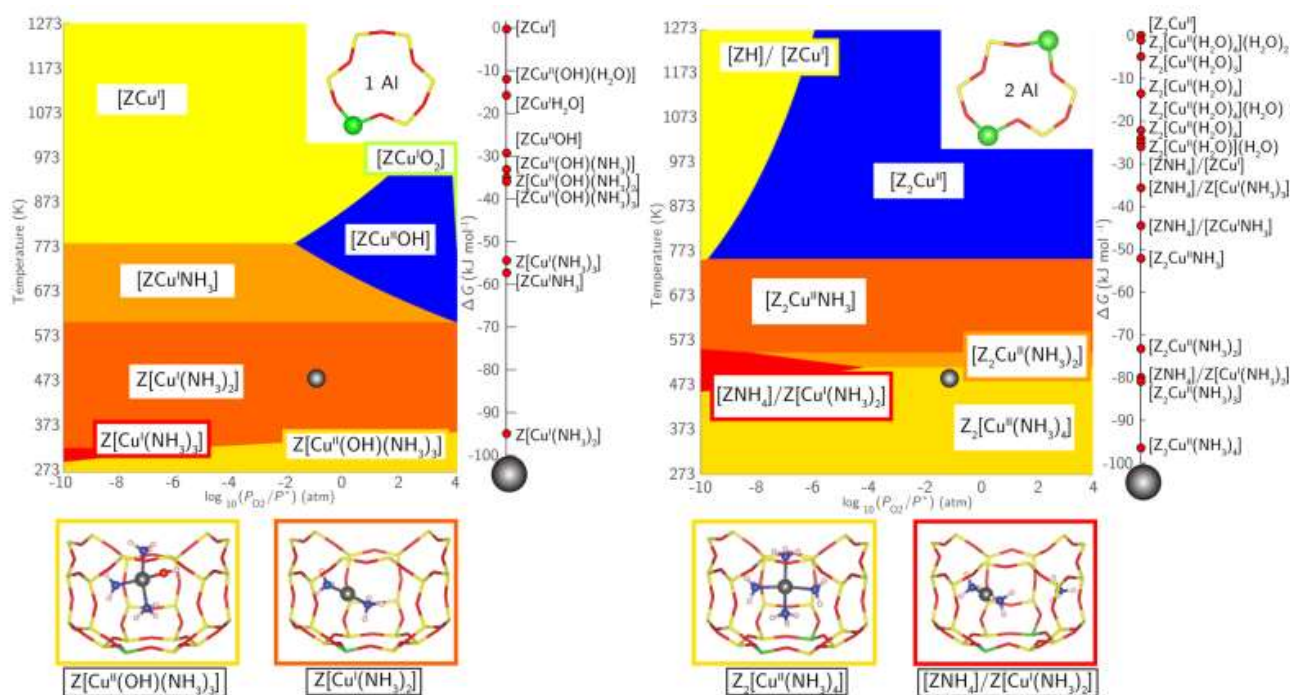
Fig. 17. Phase diagrams for *1Al* (left) and *2Al* (right) sites with varying temperature and oxygen equilibrium pressure (P_{O2}) at 300 ppm of NH_3 and 2% H_2O. Relative rankings for all species $\Delta G_{form} < 0$ at 473 K and 10% O_2 (chrome spheres on the phase diagrams) are given to the right of each phase diagram. The structures shown on the bottom are the most stable Cu(I) (red) and Cu(II) (golden) under these conditions. Adapted by permission of the American Chemical Society (copyright 2016) from ref.[75]

The theoretical phase diagrams in Fig. 17 illustrate in an impressive way the complex dynamics in Cu-speciation during the NH_3-SCR reaction.

Despite the tremendous research efforts of many academic and industrial groups around the world, and the growing number of proposed reaction mechanisms for the NH_3-SCR reaction (both at high and at low temperatures, see *e.g.* those reported in Fig. 18), a complete picture, comprising all the elementary steps is still missing.

One of the most puzzling questions for low temperature SCR remained to be the change in kinetics from quadratic to linear dependency and the decrease in the apparent O_2 reaction order from 0.8 to 0.3, both with increasing Cu density.[77, 161] Very recently, these experimental observations could be reconciled by a combination of steady-state and transient kinetic measurements, XAS, and first-principles calculations. Paolucci *et al.*[77] propose that at low temperature reaction conditions (~200 °C), the NH_3-solvated Cu(I) ions can travel through zeolite windows and form transient ion pairs that are able to activate oxygen via a Cu(I) → Cu(II) redox step (Fig. 18a).
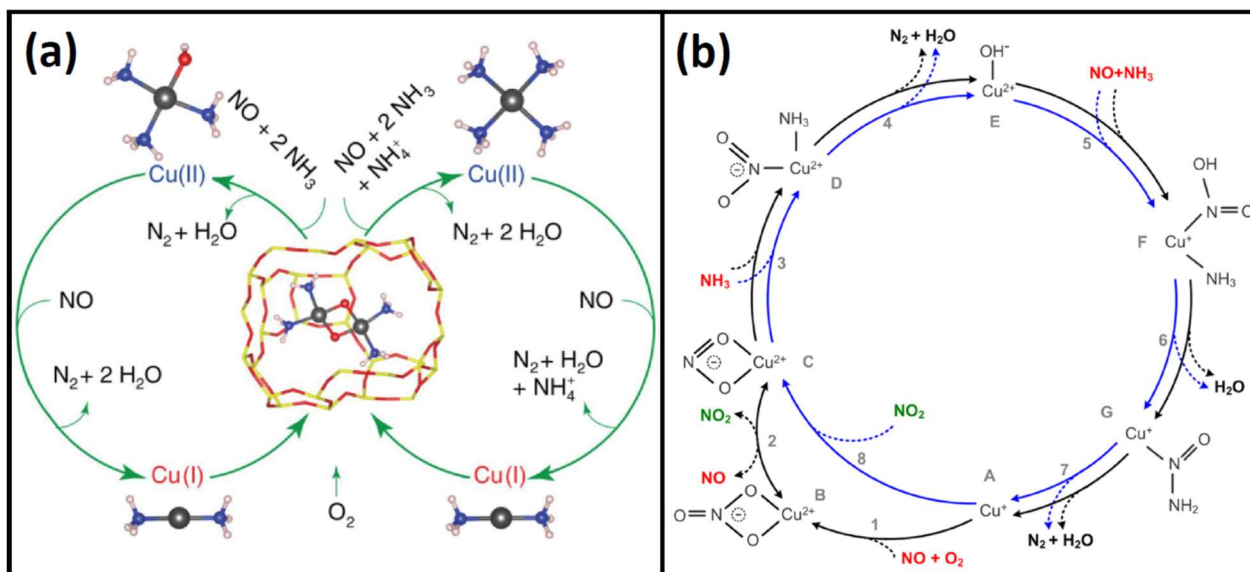
Fig. 18. Part (a): low-temperature SCR catalytic cycle proposed by Paolucci et al.,[77] reproduced by permission of the American Association for the Advancement of Science (copyright 2017) from ref.[77] Reduction steps proceed on site-isolated Cu(II) ions residing near one (left-hand cycle) or two (right-hand cycle) framework Al centres with constrained diffusion of Cu(I) ions into single cages and oxidation by O_2 (inner step). NH_4^+ is formed and consumed in the right-hand cycle to maintain stoichiometry and charge balance. Gray, Cu; yellow, Si; red, O; blue, N; and white, H. Part (b): SCR cycle proposed by Janssens et al.,[24] reproduced by permission of the American Chemical Society (copyright 2015) from ref.[24] The fast SCR cycle, Eq. (3), is represented in blue, and the NO activation cycle is represented in black. Reactants are indicated in red, reaction products are indicated in black, and the NO_2 intermediate is indicated in green. In the standard SCR reaction, the NO activation cycle, and fast SCR cycle, vide infra Eq. (4), run at equal rates; the stoichiometry of the standard SCR reaction is then found by adding these two cycles. The oxidation states of the Cu ions have been assigned according to the magnetic moment found in DFT: M(Cu(II)) > 0.45 and M(Cu(I)) < 0.1.

In a recent contribution, Marberger et al.[27] use transient methods followed by quick-scanning EXAFS and come to the conclusion that the rate-limiting step in low temperature NH_3-SCR is related to the re-oxidation of $[Cu(NH_3)_2]^+$ to $[Cu(NH_3)_4]^{2+}$, which at the same time is inhibited by the strong interaction of NH_3 with the Cu(I) complex. However, it should be pointed out that Marberger et al.[27] rely on data based on only one sample, i.e. at low Cu-loading. It has been shown previously that the SCR kinetics strongly depend on the Cu loading and in particular on the Cu/Al ratio.[20, 161]

While the formation and catalytic relevance of the mobile $[Cu(NH_3)_2]^+$ and $[Cu(NH_3)_4]^{2+}$ complexes in low temperature SCR seems to be now fairly well documented, the observation and significance of other reaction intermediates is still debated. One prominent example is the question concerning the role of the often-observed Cu-nitrates in the SCR reaction. Janssens et al. proposed a consistent catalytic cycle for the NH_3-SCR reaction over Cu-CHA, where Cu-nitrate formation plays an important role (Fig. 18b).[24] Their catalytic redox cycle is based on the observation that it is possible to separate the oxidation step from the reduction step and study the individual half-cycles by switching between NH_3+NO and NO+O_2 atmospheres. Staring from NO+O_2 (oxidative) conditions Cu(II)-nitrate species are formed, which then react in NH_3+NO (reductive) conditions to the solvated Cu(I)-NH_3 species (as described above). Switching back to NO+O_2 (oxidative) conditions, Cu(II)-nitrate species were re-formed (as identified by IR, EPR and XAS) proving a closed catalytic cycle.[24, 37] Janssens et al. proposed their mechanism originally as the simplest case for a SCR cycle, having only isolated Cu-ions. In their mechanism the nitrate intermediate combines with NO to generate Cu-nitrite and gaseous NO_2, which agrees well with the experimentally often observed transient formation of gaseous NO_2 when switching to oxidative conditions. The presence of NO_2 as an intermediate in the standard SCR cycle allows to "short-cut" the oxidation half-cycle and thereby establishes a link to the so-called fast SCR given as:[24]

$$NO + 2\ NH_3 + NO_2 \rightarrow 4\ N_2 + 3\ H_2O. \tag{4}$$

In contrast, Marberger *et al.* argue that at low temperatures nitrates appeared only after the reaction environment is far away from SCR conditions, and suggest that they are not involved in the SCR reaction cycle.[27] As we have just explained above, at high temperatures, Cu ions lose their NH_3 ligands and thereby also their mobility. They are then attached to the walls of the zeolite (at ion-exchange positions) and hence their possibility to dynamically form dimers (to activate oxygen) is greatly diminished. It is therefore conceivable that the nitrate route described by Janssens *et al.*, *i.e.* the NO activation via oxygen,[24] becomes a relevant step in the SCR reaction at higher temperatures (above 300 °C). More experiments, in particular at high temperatures, are required to fill out the remaining gaps in our understanding of the NH_3-SCR mechanism over Cu-CHA.

3.1.1 Modelling mobility and reaction-dependent restructuring of Cu-active sites. The recent discoveries in the context of low-temperature NH_3-SCR reviewed above emphasize how the concepts of mobility and reaction-dependent restructuring of Cu-sites needs to be properly addressed in theoretical modelling of redox catalysis over Cu-CHA. O_2-activation over transient Cu pairs formed from NH_3-solvated Cu ions (see Fig. 18a), which mobility is restricted by electrostatic tethering to charge-balancing framework Al sites in the framework is a paradigmatic example.[77]

Dealing with a catalytic function which is not entirely *homogeneous* (mobility of active sites governed by molecular diffusion), nor *heterogeneous* (immobile active sites), challenges the standard computational approaches employed by the catalysis community. In particular, routine calculations are commonly performed employing computed vibrations to estimate adsorbate entropies. However, from experiment it is clear that molecular adsorption under specific conditions mobilizes Cu sites to the extent that they behave in a pseudo-homogenous manner. The mobilized Cu-species will thus possess not just vibrational, but also significant translational and rotational degrees of freedom, rendering conventional static 0K DFT calculations inadequate. Under these conditions, molecular dynamics (MD) or similar approaches are required.

The milestone work by Paolucci et al.[77] presented before employed *ab initio* metadynamics for sampling of rare events to predict the mobility of $[Cu(NH_3)_2]^+$ species inside the CHA framework over time-scales inaccessible by standard *ab initio* MD. The authors computed the free energy profile (Fig. 19a, black line) using the Cu-Al coordination distance (Cu belonging to $[Cu(NH_3)_2]^+$, Al located at a framework T-site) as the collective variable, within a 72-T-site CHA supercell.

The free energy minimum is at a Cu-Al distance of 4.7 Å, reactant state (1) in Fig. 19a,b. It then increases with Cu–Al separation until 8 Å, when the Cu ion crosses an *8r* window between two cages, transition state (2) in Fig. 19a,b. Free energy is observed to decrease again as soon as the Cu ion enters into the adjacent cage (product state (3) in Fig. 19a,b), until the Cu-Al increases above 9 Å. Thus, metadynamics predicted a ~9 Å maximum diffusion distance for $[Cu(NH_3)_2]^+$ species, highly mobile but still constrained by electrostatic tethering to charge-balancing Al sites.
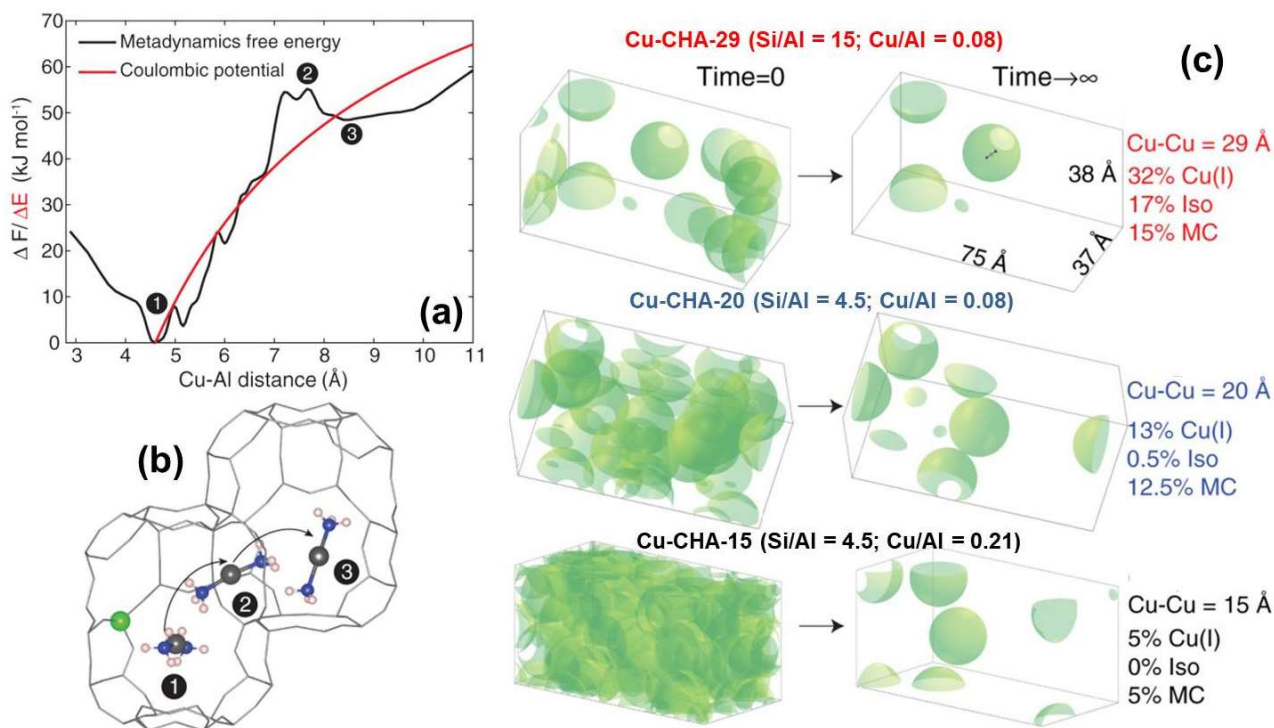
Fig. 19. (a) Free energy profile as a function of the Cu–Al distance (Cu ions belonging to mobile $[Cu(I)(NH_3)_2]^+$ species and charge-balancing Al atoms belonging to the CHA framework) computed for a 72-T-site CHA supercell by metadynamics (black line). The key steps along the profile are indicated in the figure, including: (1) reactant state - $[Cu(I)(NH_3)_2]^+$ in the same cage as Al; (2) transition state - $[Cu(I)(NH_3)_2]^+$ diffusion through an *8r* window; (3) product state - $[Cu(I)(NH_3)_2]^+$ in the neighbouring cage without Al. The energy profile computed from a point-charge electrostatic model is also reported as a red line for comparison. (b) $[Cu(I)(NH_3)_2]^+$ configurations at states (1) – (3) described in part (a); atom colour code: Cu, grey; Al, green; N, blue; H, white. (c) Snapshots taken from simulated initial (Time = 0) and final (Time → ∞) Cu(I) spatial distributions for three Cu-SSZ-13 sample with different composition, resulting in Cu–Cu separations of 29 Å (Cu-CHA-29, top panel), 20 Å (Cu-CHA-20, middle panel), and 15 Å (Cu-CHA-15, bottom panel). The limited diffusion volume accessible by Cu(I) ions are indicated by 9 Å radius green spheres. The simulation results reported on the right include the total fraction of unoxidized Cu(I), in good agreement with transient XAS results, as well as its decomposition into physically isolated (Iso) and functionally isolated (MC – 'Musical Chairs') components. Reproduced by permission of the American Association for the Advancement of Science (copyright 2017) from ref.[77]

Combining the metadynamics-based analysis of Cu-mobility with the necessity of the transient formation of Cu(I) pairs for O₂-activation, the authors were able to accurately model the fraction of unoxidized $[Cu(I)(NH_3)_2]^+$ experimentally detected in transient XAS experiments over three Cu-CHA catalysts with different composition, resulting in computed Cu–Cu separations of 29, 20, and 15 Å (Fig. 19c). The authors considered a CHA supercell with statistical Al distribution governed by the Löwenstein's rule[100] and Cu ions randomly associated with framework Al. The simulation was governed by two key rules: (i) each Cu(I) ion can access a limited diffusion volume (9 Å radius green spheres in Fig. 19c) and (ii) only Cu(I) ions with overlapping diffusion volumes can form an O₂-bridged Cu pair (structure depicted in the middle of Fig. 18a). The snapshot from the simulated final Cu spatial distribution (time → ∞ in Fig. 19c) captured the residual un-oxidized Cu(I) ions. These included either physically isolated (Iso) or functionally isolated ions (MC = Musical Chairs: sharing their diffusion volumes with Cu ions having more than one potential partner, and colloquially depicted as the losers in a *musical chairs* game).

The same research group has further addressed the problem of estimating of entropy contribution to adsorption free-energy for Cu sites in the SSZ-13 zeolites by reporting an *ab initio* Potentials of Mean Force (PMF)-based approach.[80] In contrast to strategies relying on the Quasi-Harmonic Approximation (QHA),[186, 187] previously applied to zeolite-based catalysts,[188] adsorption free energies obtained from a PMF avoid arbitrary assumptions about the dynamical degrees of freedom of the adsorbate-site complex.[189, 190] The method proposed by Li et al.[80] involves a separation of the

free energy into a desorption from the site to the cage and an extraction from the cage to an external reference state. It has been applied to the adsorption of representative small molecules at Cu sites in SSZ-13 (H_2O, NH_3, NO, CO). The resulting free energies are substantially more negative than those computed employing the harmonic approximation (HA), due to the significant mobility imparted to the Cu itself upon adsorption. In contrast, Nielsen et at.[191] investigated the adsorption of H_2O in protonic CHA, and found that a correction scheme leading to substantially less negative free energies of adsorption was required to reproduce experimental data.

The recent work by Chen et al.,[79] focusing on O_2-activation over $[Cu(I)(NH_3)_2]^+$ species and its role in the NH_3-SCR over Cu-CHA, also takes into account the entropy challenges connected with molecular adsorption at metal sites in zeolites. The authors highlight how, in the confined environment of the zeolite pores, molecules behave like a fluid phase, exhibiting significantly lower entropies than in the gas phase, in line with the work of Nielsen et al.[191] *Ab initio* constrained MD is employed to exemplify this effect, by calculating the free energy difference for NO adsorption to $[Cu(I)(NH_3)_2]^+$ from the fluid phase at 473 K.

Beside the iconic Cu mobilization phenomena observed under low-T NH_3-SCR conditions, finite temperature alone has been demonstrated to significantly impact the mobility of Cu in the CHA framework. Göltl et al.[192] showed how, even in the absence of strong 'solvating' ligands such as NH_3 or H_2O or adsorbates (e.g. NO and CO, often used as probe molecules in IR experiments, see Section 2.1.2) at 300 K bare Cu ions regularly change their coordination in the CHA framework. Through MD, the authors explored the most probable environments for both Cu(I) and Cu(II) cations, analysing their distribution as a function of Al siting in the zeolite lattice.

In this respect, Paolucci et al.[75] performed 298 K *ab initio* MD simulations (60 ps of equilibration followed by 90 ps of sampling) on the lowest free energy Cu-species at *1Al* and *2Al* sites representative of Cu-CHA in its hydrated and activated state. For framework-interacting Cu-species mobility is largely decreased with respect to Cu aquo-complexes, but bare Cu ions, especially in the +1 oxidation state, still show appreciable mobility around their most stable sites. From these results is it clear that thermal motion of the bare cations should be also considered in the interpretation of spectroscopic findings, e.g. by averaging over computed spectra at many configurations weighting for the residence time of the system in each of them.

In summary, the dynamic nature of Cu-ions in zeolites poses novel challenges for computational chemistry in catalysis. Adsorbates that restructure the active site but are not necessarily consumed during the catalysis, spatial distribution of mobile but electrostatically tethered active sites, mobility effects on the simulation of spectroscopic observables, are all areas that will need further exploration and methods development. The recent theoretical work mentioned above pave the way to future advances in the field.

3.2. Direct conversion of Methane into Methanol

In a 2005 key publication, Schoonheydt and co-workers demonstrated the use of Cu loaded zeolites (ZSM-5 and mordenite) for low temperature conversion of methane to methanol.[164] Later, several zeolite topologies, containing Cu, Fe, and Co have been investigated for this reaction, as recently summarized by van Bokhoven and co-workers.[193-195] Usually, the process is carried out in a three step manner comprising i) oxidation (most frequently with oxygen) at high temperature (450 °C is typical); ii) methane loading at substantially lower temperatures (~60-200 °C); iii) followed by methanol extraction, usually with steam, occasionally with liquid solvents. Thus, the reaction at hand is most often carried out using a chemical looping protocol. As methane and the oxidant are not mixed, the selectivity to methanol tends to be high (~90 %, prominent byproducts are CO and CO_2), whereas the yield expressed as moles of methanol per mole of metal is moderate. The production rate in real time is very low, due to the chemical looping principle comprising three lengthy steps.

A few examples of continuous, true catalytic processes have been reported for several Cu loaded zeolites, including SSZ-13, co-feeding methane with oxygen and steam at 210 °C.[196] Ipek and Lobo[30] reported the catalytic conversion of methane to methanol on Cu loaded SSZ-13 (and other zeolites)

using N_2O as oxidant. Invariably, the turn over frequencies or site time yields are very low, and adverse conversion/selectivity relationships have been reported, as one normally would expect when abandoning the chemical looping concept.[30]

The objective of this section can be expressed as follows. First, we wish the review the performance of CHA based materials in the stepwise selective oxidation of methane to methanol, focusing on the productivity per Cu atom. This will include the aluminosilicate (SSZ-13) and the very relevant isostructural silicoaluminophosphate analogue (SAPO-34). Second, it will be demonstrated how these productivities depend quite profoundly on the exact conditions employed. Third, a remark will be made on the extent to which the methanol productivity depends on the initial properties of the zeolite and the exact procedure by which Cu is introduced. Finally, as the overall objective of the present contribution is to describe structure-reactivity relationships for Cu-CHA, we will highlight the importance of carrying out characterization at exactly the same conditions as when measuring reactivity.

3.2.1. The performance of CHA based materials in the stepwise methane to methanol reaction.
Essentially, only a few papers have reported performance data for Cu loaded CHA materials in the selective oxidation of methane to methanol.[28, 30, 33-35] The published data are summarized in Table 1, together with compositional data, details on the testing protocol, as well as specifics on the preparation procedure. It appears customary to present productivities in either micromoles of methanol per gram of material or as the ratio between methanol and Cu, or both. The latter is a good descriptor for active Cu speciation, whereas from a process perspective, it is the production per mass of sample that is of primary interest. For convenience, both units are employed in Table 1 and Fig. 20.

It may be noted that the reaction is not perfectly selective. Dimethyl ether tends to be formed, as seen also for other zeolites.[167, 197, 198] Dimethyl ether, which is readily formed on acid sites from methanol dehydration, can be considered a desired product in this context. Unwanted by-products are CO and CO_2. In the limited context of CHA based materials, only Pappas et al.[33] specify products other than methanol. The selectivities to methanol and dimethyl ether range from ~50 % to above 90 %, but are usually above 85 %. The methane activation temperature seems to have a detrimental effect on selectivity; it should not be above 200 °C.[33]
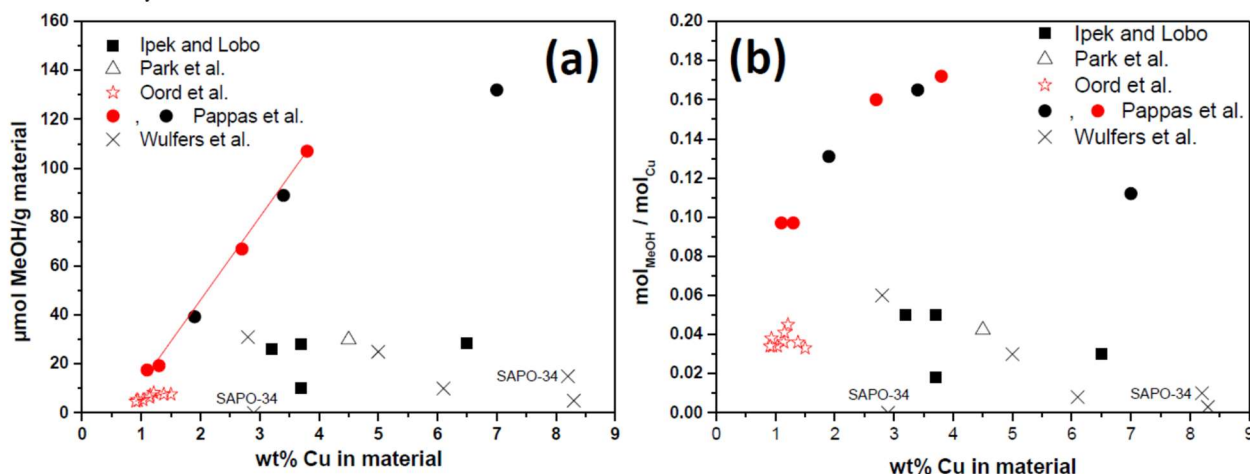
Fig. 20. Methanol productivities over Cu loaded CHA. Part (a): Productivities expressed per mass of material. Part (b): Productivities normalized to Cu loading. Red symbols represent subsets of data from refs.[33, 35] on catalysts prepared using the same zeolite support: for these two subsets, the results can be directly compared to the copper loading without any interferences related to the zeolite properties. The red line in part (a) connects data from one such consistent subsets. Exact reaction conditions can be found in Table 1. It should be noted that only Pappas et al.[33] specifies that dimethyl ether is considered among the products. Further, Pappas et al. have employed an optimized (and lengthy) reaction protocol. Previously unpublished figure summarizing data taken form Refs.[28, 30, 33-35]

The maximum productivity reported for CHA is 132 µmol/g or 0.112 mol_{MeOH}/mol_{Cu}, for the first reaction cycle for a sample with Si/Al = 5.2; Cu/Al = 0.49; Cu content 7.0 wt%.[33] This can be compared to values of 89 µmol/g or 0.23 mol_{MeOH}/mol_{Cu} for Cu-ZSM-5 (Si/Al = 14; Cu/Al = 0.67;

Cu content 4.2 wt%)[199] and 170 μmol/g or 0.33 mol_{MeOH}/mol_{Cu} (including both MeOH and DME) for Cu-mordenite (Si/Al = 7.2; Cu/Al = 0.27; Cu content 3.3 wt%).[167] Perusal of Fig. 20 reveals that the most productive sample (132 μmol/g)[33] is not the one that performs best when normalizing to Cu loading. This is rather the sample giving 107 μmol/g or 0.172 mol_{MeOH}/mol_{Cu} (Si/Al = 12; Cu/Al = 0.49; Cu content 3.8 wt%). Thus, having taken the trouble of converting the data for straightforward comparison, it becomes clear that the highest productivities reported for Cu loaded CHA, MFI, and MOR are strikingly similar, even when comparing per gram of material, per mass of Cu or per mole of Cu. Based on the data reported, SAPO-34 appears to perform poorly.

Table 1. Performance of Cu loaded CHA materials (SSZ-13 and SAPO-34) in the stepwise selective oxidation of methane to methanol. Information about the cation predominantly present in the parent material (sodium or proton), elemental composition and copper loading, details of the three steps of the reaction protocol, the means by which the products were detected and quantified, the productivities (normalized to both mass of material and Cu loading), the selectivity, and notes about the exact Cu introduction procedure are listed. Values in italics have been recalculated by us from the published data for completeness. Some of the here reported data are summarized in Fig. 20. Previously unpublished Table.

Zeolite	Si/Al or (Al+P)/Si	Cu/Al or Cu/Si	Cu (wt%)	Protocol	Detection principle	Productivity (µmol/g)		Productivity (mol_{MeOH}/mol_{Cu})		Selectivity	Preparation	Ref.
Na-SSZ-13	6	0.35 ± 0.07	5.0 [a]	i) 10 h in O_2 at 450 °C ii) 20 + 20 min in 7.5 kPa CH_4 at 60 and 200 °C iii) 5 h with N_2 saturated with water vapor at 200 °C	On-line GC and MS	28		0.03		Not reported	Liquid exchange of Na-form with copper(II)acetate	[28]
Na-SSZ-13	12	0.35 ± 0.06	2.8	As above	As above	31		0.06		As above	As above	[28]
Na-SAPO-34	5	0.17 ± 0.06	2.9	As above	As above	< 1		< 0.001		As above	As above	[28]
H-SAPO-34	6	0.6 ± 0.2	8.2	i) 10 h in N_2 at 650 °C; 15 h in O_2 at 450 °C ii) 20 + 20 min in 7.5 kPa CH_4 at 60 and 200 °C iii) 8 h with N_2 saturated with water vapor at 200 °C	As above	15		0.01		As above	High temperature gas-solid exchange of H-form with copper(I)chloride	[28]
H-SSZ-13	6	0.6 ± 0.3	8.3	As above	As above	5		0.003		As above	As above	[28]
H-SSZ-13	12	0.8 ± 0.3	6.1	As above	As above	10		0.008		As above	As above	[28]
H-SSZ-13	5	0.39	6.5	i) 7 h in O_2 at 450 °C ii) 20 min in neat CH_4 at 50 °C iii) N_2 saturated with water vapor at 200 °C	On-line GC and MS	28.5		0.03		Not reported	Liquid exchange of H-form with copper(II)acetate	[30]
H-SSZ-13	12	0.40	3.2	As above	As above	26		0.05		As above	As above	[30]
Na-SSZ-13	12	0.47	3.7	As above	As above	28.1		0.05		As above	Liquid exchange of Na-form with copper(II)acetate	[30]
Na-SSZ-13	12	0.47	3.7	i) 4 h in He at 450 °C ii) 20 min in neat CH_4 at 50 °C iii) N_2 saturated with water vapor at 200 °C	As above	10		0.018		As above	As above	[30]
Na-SSZ-13	15.8	0.84	4.5	i) 4 h in O_2 at 450 °C ii) 30 min in neat CH_4 at 200 °C iii) repeated stirring with deionized water for 24 h	GC-FID analysis of extracts	30.0		0.0424		Not reported	Liquid exchange of Na-form with copper(II)acetate	[34]
Na-SSZ-13	20	0.30	1.5	i) 2 h in O_2 at either 450 °C or 550 °C ii) 20 min in 38 kPa CH_4 at 60 °C, heating to 200 °C in 38 kPa CH_4 iii) N_2 saturated with water vapor at 200 °C for 110 min	On-line GC-FID	7.6		0.033		Not reported	Liquid exchange of Na-form with copper(II)acetate	[35]
Na-SSZ-13	20	0.28	1.38	As above	As above	7.6		0.036		As above	Liquid exchange of Na-form with copper(II)sulfate	[35]
Na-SSZ-13	20	0.23	1.15	As above	As above	7.2		0.041		As above	As above	[35]
Na-SSZ-13	20	0.24	1.21	As above	As above	8.2 [b]	9.0 [c]	0.045 [b]	0.049 [c]	As above	As above	[35]
H-SSZ-13	20	0.23	1.14	As above	As above	6.3 [b]	7.6 [c]	0.036 [b]	0.043 [c]	As above	Liquid exchange of H-form with copper(II)sulfate	[35]

Na-SSZ-13	20	*0.19*	0.95	As above	As above	4.9[b]	7.5[c]	0.034[b]	0.052[c]	As above	Liquid exchange of Na-form with copper(II)sulfate	[35]
Na-SSZ-13	20	*0.20*	1.03	As above	As above	5.3		0.034		As above	As above	[35]
Na-SSZ-13	20	*0.19*	0.93	As above	As above	5.4		0.038		As above	Liquid exchange of Na-form with copper(II)acetate	[35]
Na-SSZ-13	20	*0.18*	0.91	As above	As above	4.7		0.034		As above	Liquid exchange of Na-form with copper(II)sulfate	[35]
Na-SSZ-13	5.2	0.49	*7.0*	i) 8 h in O_2 at 500 °C ii) 6 h in neat CH_4 at 200 °C iii) He/Ne saturated with water vapor (saturator at 45 °C) at 200 °C for 110 min	GC-MS Both dimethyl ether and methanol considered products; CO and CO_2 as by-products.	132		0.112		87 % to MeOH and DME	Liquid exchange of H-form with copper(II)acetate	[33]
Na-SSZ-13	12.1	0.14	*1.1*	As above	As above	17.5		0.097		85 %	As above	[33]
Na-SSZ-13	12.1	0.16	*1.3*	As above	As above	19.3		0.097		85 %	As above	[33]
Na-SSZ-13	12.1	0.34	*2.7*	As above	As above	67		0.16		87 %	As above	[33]
Na-SSZ-13	12.1	0.49	*3.8*	As above	As above	107		0.172		87 %	As above	[33]
Na-SSZ-13	14.8	0.53	*3.4*	As above	As above	88.9		0.165		87 %	As above	[33]
Na-SSZ-13	28	0.52	*1.9*	As above	As above	39.3		0.131		86 %	As above	[33]

[a] Values in italics are calculated by us from published data
[b] Pre-treated in oxygen at 450 °C
[c] Pre-treated in oxygen at 550 °C

It is of interest to consider the productivity as a function of Cu loading. Oord et al.[35] and Pappas et al.[33] have investigated the effects of Cu loading for the same zeolite support for more than two data points (see Fig. 20a). It does appear that the productivity, when expressed per amount of material, can be positively correlated to Cu loading, in line with data reported for mordenite by Grundner et al.[167] However, the range that can be investigated is invariably limited. For Oord et al.[35] a slope of 0.035 is found when plotting the productivity (in units of $\mu mol_{MeOH}/g$ per $\mu mol_{Cu}/g$), whereas a substantially steeper relationship with a slope of 0.21 is found by Pappas et al.[33] Grundtner et al.[167] reported a slope of 0.33 $\mu mol_{MeOH}/g$ per $\mu mol_{Cu}/g$ for Cu-mordenite. The data from Oord et al.[35] do appear to pass through the origin, whereas the data from Pappas et al.[33] have a negative intercept. A non-zero intercept or a non-linear evolution of productivity might be linked to dynamic changes of the Cu speciation with differing loading, in line with the recent discoveries of Paolucci et al.[77] and Gao et al.[200] for selective catalytic reduction. However, much more work would be needed in order to verify if similar effects can play a role also for the methane oxidation reaction. Finally, when considering the productivities normalized to Cu loading (Fig. 20b), it is not straightforward to draw definitive conclusions.

3.2.2. The effects of reaction protocol and material preparation procedure. As indicated, the oxidation of methane to methanol is usually carried out in three steps. Clearly, the amount of methanol produced will depend on the exact conditions employed for each of these three steps, *i.e.* the temperature, the duration, and the partial pressure of reactive gas or atmosphere employed. Oord et al.[35] compared the effects of carrying out the high temperature oxidation step at either 450 or 550 °C (for 2 h in neat O_2). This increase resulted in improved productivities by as much as 10-50 %. Pappas et al.[33] performed a very detailed investigation of the effects of reaction protocol on productivity, and the results are reproduced in Fig. 21.
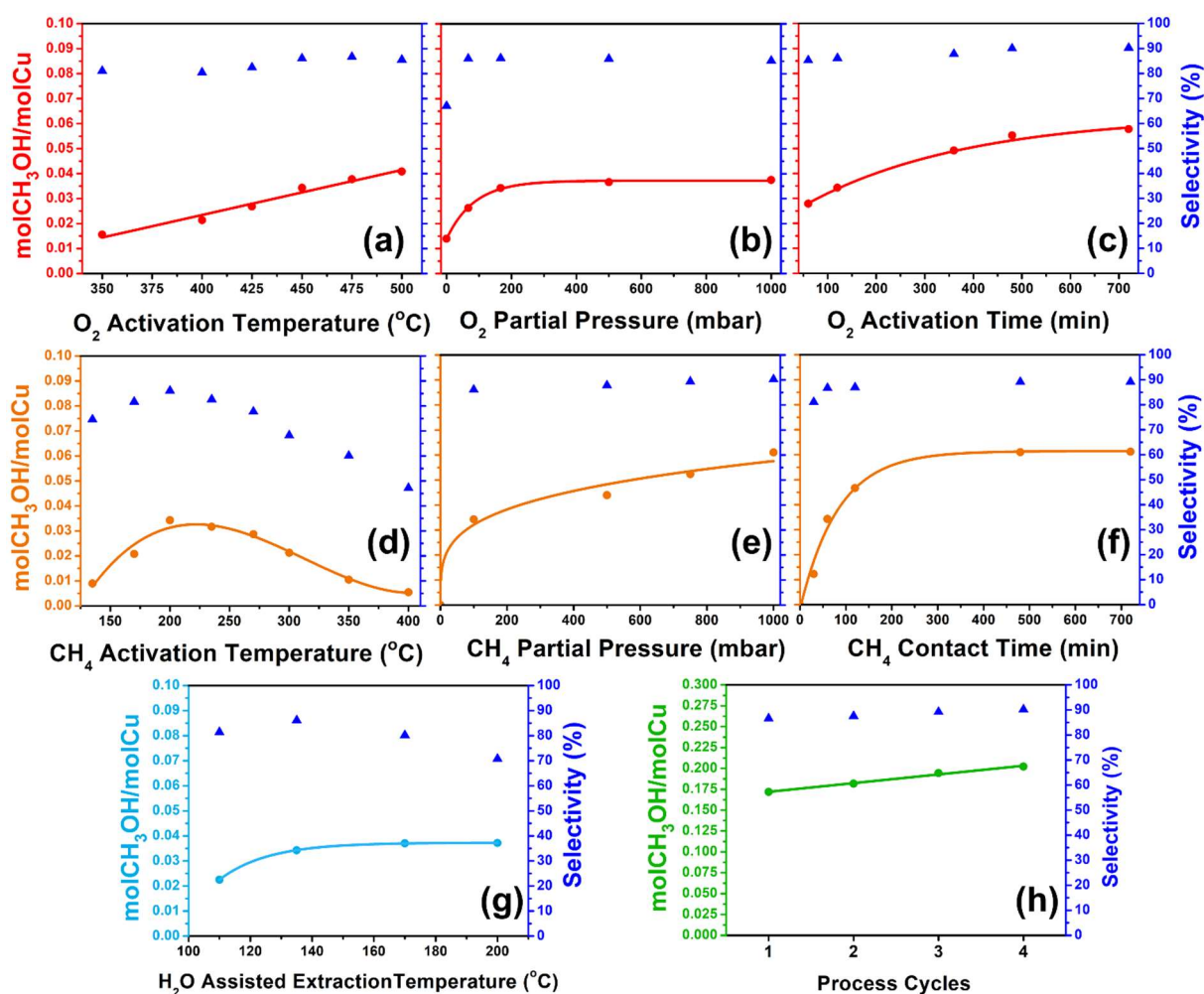
Fig. 21. The effects of various protocol parameters on the normalized methanol productivity (circles) and selectivities (triangles). General conditions applied: Panels (a-g): O_2 activation at 450 °C for 120 min in 187 mbar O_2, CH_4 loading at 60 min in 100 mbar CH_4 at 200 °C, H_2O assisted extraction in 10 % H_2O stream at 135 °C). Parameter variation: (a) O_2 activation temperature; (b) O_2 partial pressure; (c) O_2 activation time, (d) CH_4, loading temperature; (e) CH_4 partial pressure; (g) CH_4 contact time; (g) H_2O assisted extraction temperature. Panel (h) shows the effect of multiple cycles of the process at optimized conditions, *i.e.* O_2 activation at 500 °C for 480 min in 1000 mbar O_2, CH_4 loading for 360 min in 1000 mbar CH_4 at 200 °C, and online H_2O assisted extraction with a 10 % H_2O stream at 200 °C). Reproduced by permission of the American Chemical Society (copyright 2017) from ref.[33]

The methanol productivity is positively influenced by oxygen activation temperature, partial pressure, and time. The productivity is quite profoundly positively influenced by the methane partial pressure and time, whereas there is a clear optimum for the methane activation temperature. Temperatures above 200 °C rapidly leads to loss of selectivity and productivity. The temperature employed during steam extraction has only moderate effect on the selectivity, indicating that the two last steps could be executed isothermally. Panel (h) in Fig. 13 also conveys the point that the productivity cannot be expected to be stable during multiple reaction cycles.[33] These findings for Cu loaded CHA are to a large degree in line with data reported for other zeolites. In particular, the positive impact of elevated methane pressure is well documented.[195] Bozbag *et al.*[201] investigated the effects of multiple reaction cycles using Cu loaded mordenite, where the Cu was introduced either by liquid ion exchange or solid state ion exchange. When preparing the material using liquid ion exchange, it was found that the yield increased by at least 30 % for the second cycle and remained constant afterwards. For the material prepared via solid state ion exchange, a successive improvement with cycles was seem due to a gradual removal of chlorine. A warning was issued, stating that analyzing only one reaction cycle is not representative of the long-term performance.[201] Although not systematically explored for CHA, it is also well known that the material performance can change depending on the starting characteristics of the zeolite (Si/Al ratio) and the exact preparation

procedure, *e.g.* liquid ion exchange vs. solid state ion exchange, choice of Cu salt, pH during preparation, if Cu is introduced to the Na-form or H-form of the zeolite, etc.[167, 198, 201]

The concentration of methanol produced is fairly low, and the extraction time is considerable. See for example Figure 1 of ref.[28] and Figure 2 of ref.[35] Thus, the study of this reaction constitutes a considerable analytical challenge, and Table 1 lists also the means of product quantification employed in the various studies. Wulfers *et al.*[28] report that all productivities were reproducible within 5 µmol/g, whereas Oord *et al.*[35] report productivities with four digits. In our experience, the productivities are reproducible within 3 % for the same materials (5 replicate tests), and about 10 µmol/g when comparing two materials that were prepared to be identical. The reproducibility within a laboratory does therefore appear to be very good. However, no inter-laboratory comparisons have been reported, so there is no information available on the effects of errors or bias of a systematic nature. Fig. 20 does imply that quite different productivities are reported for seemingly similar materials when tested by different laboratories. However, it is clear that the methanol productivities are also highly dependent on material preparation procedure and the reaction protocol employed.

Altogether, this means that attempts to compare data reported by different laboratories could be associated with serious pitfalls. As some differences in the applied reaction conditions invariably are encountered, a compilation of data as presented in Fig. 20 becomes substantially less useful than one might desire. Using the data found by Wulfers *et al.*[28] as an example, it can be found that different oxygen activation times and product extraction times were used for materials prepared using gas-solid ion exchange and liquid ion exchange. The exact effects on the productivity are unknown. In this particular case, the objective was primarily to demonstrate activity, so the difference in protocol was immaterial. Nevertheless, the use of a plethora of reaction protocols does constitute a major obstacle for the establishment of fundamental insights. Moreover, this will have consequences when relating materials performance to characterization data in attempts to establish structure-function relationships. Even though *operando* characterization is desired, some adaptation of the experimental procedures are often needed, due to practical limitations or time constraints (*e.g.* when using synchrotron radiation). Taking our own work as an example, it was established (Fig. 20) that O_2 activation at 500 °C for 8 h in neat O_2 gave the highest methanol productivity. However, when doing *operando* XAS, activation was carried out by maintaining the sample at 500 °C in O_2 for 2 h (see Figure 3 of ref.[33] and Section 3.2.4 here after). The obvious consequence is that the concentration of active species or intermediates might not be the same during characterization as it is during reactivity measurements, again making it harder to establish structure-function relationships.

3.2.3. Other oxidants. It is known that the temperature alone can influence the redox chemistry of Cu in zeolites. Thus, the effects of activation in inert at high temperature (without oxidant) on methanol productivity has been widely investigated, and here reviewed in Section 2.1. Ipek *et al.*[31] found non-negligible methanol production when activating Cu loaded SSZ-13 (3.7 wt% Cu) in He at 450 °C. A productivity of 10 µmol/g or 0.018 mol_{MeOH}/mol_{Cu} was reported. Pappas *et al.*[33] found 4.7 µmol/g or 0.008 mol_{MeOH}/mol_{Cu} when activating in He at 500 °C (SSZ-13; Si/Al = 12; Cu/Al = 0.5; 3.9 wt% Cu); whereas Oord *et al.*[35] detected no methanol when activating in He (SSZ-13; Si/Al = 20; Cu/Al = 0.12; 0.95 wt% Cu). However, it is hard to envisage that the very minor productivities observed upon activation in inert represents anything beyond a curiosity.

However, other oxidants than oxygen/air have been investigated. Sheppard *et al.*[202] employed NO (and N_2O) as the oxidant for Cu loaded ZSM-5. When using NO, it was possible to operate isothermally, *i.e.* all three steps of the chemical looping were carried out at 150 °C, which has obvious advantages from a process perspective. However, the productivities were lower than those observed using O_2 activation at 500 °C. Sushkevich *et al.*[194] were able to demonstrate that the oxidation can be facilitated by a combination of steam treatment (extraction) at 200 °C followed by a thermal treatment in inert at 400 °C over Cu loaded mordenite. A key feature of this protocol is the loading of methane at high pressures (7 bar). A productivity of 0.204 mol_{MeOH}/mol_{Cu} was reported after several reaction cycles.[194]

Ipek and Lobo[30] also investigated the use of N_2O, and were able to run the oxidation reaction *catalytically*, *i.e.* not using chemical looping (for a number of zeolites, including SSZ-13; Si/Al = 12; Cu/Al = 0.4; 3.1 wt% Cu). The maximum rate of methanol production was 55 µmol/gh The catalytic reaction was carried out at 300 °C with 30.4 kPa of CH_4, 30.4 kPa of N_2O, 3.2 kPa of H_2O, and 37.3 kPa He. The methane conversion was 0.75 %, and the selectivity to methanol was 2.3 %; the main products were CO and CO_2.[30] Finally, Narsimham *et al.*[196] also reported a *catalytic* production of methanol, now using oxygen as the oxidant. A wide range of Cu loaded zeolite frameworks were investigated. The highest activity was reported for Cu loaded SSZ-13 (Si/Al = 13.8; Cu/Al = 0.50; 3.5 wt% Cu) at a value of 3.12 µmol/gh. The reaction temperature was 210 °C with 98.1 kPa of CH_4, 0.0025 kPa of O_2, and 3.2 kPa of H_2O.[196]

3.2.4. Spectroscopic insights into the MTM conversion over Cu-SSZ-13

Due to the relatively recent demonstration of MTM activity over Cu-CHA-based materials, the number of advanced characterization results reported in this context is still limited, especially if compared with the much more studied Cu-MOR and Cu-MFI zeolites.[34, 60, 72, 73, 143, 164, 165, 167, 194, 201, 203-206] Nonetheless, in the last two years, a few studies appeared[28, 31, 33, 35] employing XAS and UV-Vis-NIR spectroscopy under *in situ* and *operando* conditions to monitor the MTM reaction over Cu-CHA, aiming to identify the spectroscopic fingerprints of the methane-converting Cu-active sites in the CHA framework.

In the above-mentioned work by Pappas *et al.*,[33] beside the detailed investigation of the reaction parameters discussed in Section 3.2.2, the authors have combined laboratory activity measurements with *in situ*/*operando* XAS to explore the MTM conversion over Cu-SSZ-13 for a wide range of material compositions and reaction conditions, aiming at establishing structure-activity relationships (Fig. 22a-c).

In particular, the authors employed *operando* XAS to track the oxidation state and average coordination environment of the Cu ions in a Cu-SSZ-13 sample with Si/Al = 12, Cu/Al = 0.5 during each step of the process, including O_2-activation at 500 °C, cooling in O_2 to 200 °C, CH_4 loading at 200 °C and steam-assisted methanol extraction at 200 °C. XAS revealed tri-coordinated framework-interacting Cu(II) centers as the dominant species in the O_2-activated state at 500 °C, while cooling to 200 °C in O_2 promote an increase in the average first-shell Cu coordination number, tentatively associated with a temperature-induced modification in the oxygen binding mode in $Z[Cu(II)O_2{}^{\bullet}]$ superoxo moieites.[33] During methane loading, XANES linear combination fit indicated the Cu(II) to Cu(I) reduction for 27% of the Cu sites, in line with previous reports on Cu-MOR.[167, 205] During steam-assisted methanol extraction, the fraction of Cu(I) present in the system is observed to diminish to 14% together with the formation of 24% of mobile Cu(II) aquo complexes. It is thus clear that, also over Cu-CHA, the MTM process involves reversible redox chemistry at Cu sites.[33]

To obtain deeper insights in the nature of the active sites, Pappas *et al.*[33] also explored the impact of different pre-treatments by combining *in situ* XAS with activity measurements (Fig. 22a). High-temperature reaction with O_2, yielding the XAS signature of a tridentate, framework-interacting Cu(II) species, is again evidenced as a key requirement to form the methane-converting active sites. The impact of the composition (Cu/Al and Si/Al ratios) on the normalized productivity and its correlation with Cu-speciation was also investigated. Notably, a positive linear correlation was discovered between the normalized methanol productivity and the reducibility of the Cu centres under high-temperature treatment in He, as evaluated from XANES (Fig. 22a).[33] Here, for a quantitative determination of the fraction of ZCu(I) formed, the authors employed previous results from MCR analysis of the large composition-dependent XANES dataset[59] described in Section 2.2.3 (see in particular Fig. 12 and Fig. 13).

The authors rationalized the effect of composition on the normalized methanol productivity according to the scheme reported in Fig. 22c. High populations of bare *2Al* $Z_2Cu(II)$ sites, favored at low Si/Al ratios, inhibit the performance of the material: these redox-resistant species are completely inactive for the conversion. Z[Cu(II)OH] complexes are instead identified as possible precursors to

the active sites, though their ability to undergo self-reduction. This is optimal at intermediate Si/Al ratios, while, as pointed out in section 2.2.3.1, it becomes hampered at high Si/Al. As also supported by FTIR and Raman analysis of O_2-activated Cu-SSZ-13 (see section 2.1.2, see Fig. 4d,e), Z[Cu(II)OH] species are progressively depleted during high-temperature oxidative treatment, evolving towards different mono- and multimeric Cu(II)/active-oxygen species, among which the MTM active sites should be searched. Combining the temperature-dependent FTIR spectra reported in Fig. 4d with laboratory testing under *ad hoc* pre-treatment conditions, Pappas et al.[33] also showed how Z[Cu(II)OH] is unlikely to be directly involved in the MTM conversion. In particular, from FTIR is it clear that the intensity of the band fingerprinting Z[Cu(II)OH] is maximum at ca. 250 °C. However, if Cu-SSZ-13 is activated at such a low temperature and then subjected to the other steps of the MTM process, methanol productivity per Cu decreases drastically (below 0.01 mol CH_3OH/mol Cu *vs* ca. 0.08 mol CH_3OH/mol Cu obtained performing O_2 activation at 500 °C, while keeping all the other reaction parameters fixed, see Fig. S3 in the Supporting Information of ref.[33]).
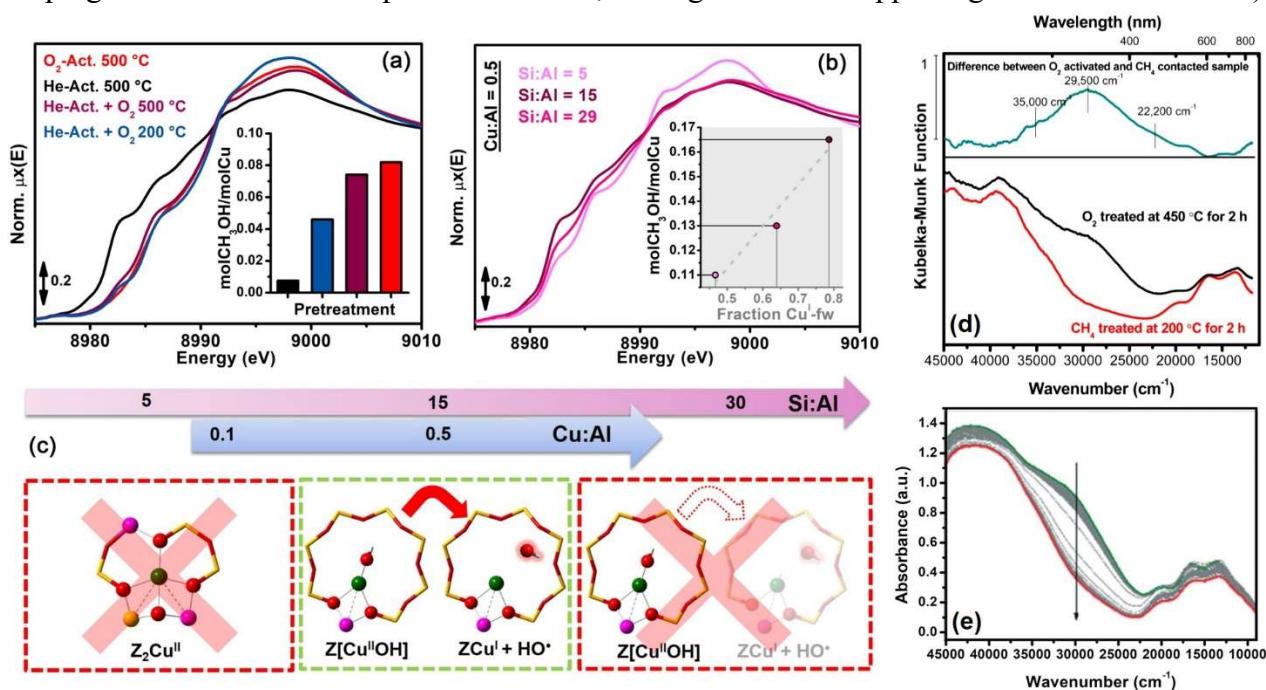

Fig. 22. Parts (a)-(b): *in situ* XANES spectra collected for: (a) Cu-SSZ-13 with Cu/Al = 0.5, Si/Al = 12 after different pre-treatments (inset: corresponding normalized CH_3OH productivities); (b) He-activated Cu-SSZ-13 with Cu/Al = 0.5 and Si/Al ratio of 5, 15 and 29 (inset: linear correlation between the normalized productivity and the fraction of ZCu(I) species in the He-activated state. Part (c): rationalization of the effect of composition on the productivity for the MTM conversion over Cu-SSZ-13. Part (d): *in situ* UV-Vis spectra collected on a Cu-SSZ-13 sample (Si/Al = 12, Cu/Al = 0.4) after O_2 treatment at 450 °C (black) followed by 2 h CH_4 treatment at 200 °C (red). The difference spectrum is shown in green in the top panel. Before the spectra were collected, the sample was cooled to room temperature. Note that small changes in sample position after each treatment render comparison of spectral intensities only qualitative. (e) *Operando* UV-Vis spectra of Cu-SSZ-13 (Si/Al = 20 and 1.21 Cu wt %, same sample investigated during O_2 and He-activation, see Fig. 4b,c) during methane addition from at 60 to 200 °C (68 min or 68 scans are shown), arrows indicate the time evolution, the green spectrum is the starting point of the experiment, while the red spectrum is the endpoint. Parts (a)-(c): unpublished figures reporting data published in ref.[33] Part (d): adapted by permission of the American Chemical Society (copyright 2017) from ref.[31] Part (e): adapted with permission of the Royal Chemical Society (copyright 2018) from ref.[35].

Additional insights into the nature of the active sites for MTM conversion over in Cu-SSZ-13 have been provided in the recent reports by Ipek *et al.*[31] and Oord *et al.*,[35] where the reactivity of O_2-activated Cu-SSZ-13 towards CH_4 has been monitored by UV-Vis spectroscopy. Ipek *et al.* worked under *in situ* conditions, reporting UV-Vis data for a Cu-SSZ-sample with Cu/Al = 0.4 and Si/Al = 12, O_2-treated at 450 °C for 2 h, and subsequently exposed to CH_4 at 200 °C for 2 h (Fig. 22d).[31] Oord *et al.* performed *operando* measurements monitoring the evolution of the UV-Vis spectrum of a Si/Al = 20, 1.21 Cu wt % Cu-SSZ-13 sample (pre-activated in O_2 at 450 °C, see Fig. 4b in section 2.1.2) during CH_4 addition from at 60 °C to 200 °C (Fig. 22e).[35]

In both cases, the CT band at ~ 29000 cm^{-1}, already discussed in sections 2.1.2 and 2.2.2, is well visible after high-temperature activation in O$_2$. Crucially, this band is observed to clearly decrease upon/after interaction with CH$_4$ (see the arrow in Fig. 22e), indicating that the Cu-species responsible of the 29000 cm^{-1} band are reacting with CH$_4$. Similar observations were previously reported for Cu-MOR and Cu-ZSM-5,[164, 165, 167] although in these cases the relevant CT bands, decreasing in the presence of CH$_4$, occur at different wavenumbers (31000 cm^{-1} for Cu-MOR[167] and 22 700 cm^{-1} for Cu-ZSM-5[164]). These lines of evidences corroborate that Cu(II) species associated with an activated-oxygen, giving rise to the characteristic CT band observed around ~ 29000 cm^{-1} in O$_2$-activated Cu-SSZ-13, could also represent possible active sites for the MTM conversion over this material. It is worth to note that, due to both the stepwise nature of the process, and the complexity in the speciation of Cu during O$_2$-activation and CH$_4$-loading steps, a distribution of Cu$_x$O$_y$ moieties that are responsible for methanol production is envisaged, rather than a single active site.

Globally, the recent spectroscopic results reviewed in this section mark a first step towards an improved understanding of methane activation over Cu-CHA-based systems, crucial to advance in the design of materials with an optimal density of active sites for the MTM reaction.

4. Industrial application

4.1. NH$_3$-SCR for diesel vehicle NO$_x$ emission control
The first NH$_3$-SCR systems for heavy-duty vehicles came on the market in 2005, and were based on V$_2$O$_5$/WO$_3$/TiO$_2$, similar to the already existing de-NO$_x$ catalyst used in stationary power stations. However, the highly dynamic conditions encountered in diesel vehicle emissions, early lead to the search for improved catalysts that could combine low temperature activity with high temperature stability. The potential of metal exchanged zeolites for such application was quickly identified, but despite significant research efforts for more than two decades, it was not until the discovery of the small pore Cu-CHA, that zeolite catalysts would have a breakthrough on the diesel vehicle market. Cu-CHA catalysts are very efficient and robust catalysts and able to meet the *EuroVI* requirements for removal of NO$_x$ from mobile diesel engine exhaust gases, also under real driving emissions (RDE).[207] They are therefore the preferred choice for modern NH$_3$-SCR technology in diesel vehicle applications in particular for engines with displacement >2 liters.

A modern commercial SCR emission control system for diesel engines comprises several key components (see top part of Fig. 23), such as a diesel oxidation catalyst (DOC), a diesel particulate filter (DPF), the SCR catalyst, and an ammonia slip catalyst (ASC). The effect of the individual components on the composition of the exhaust gas is shown schematically in the bottom part of Fig. 23.
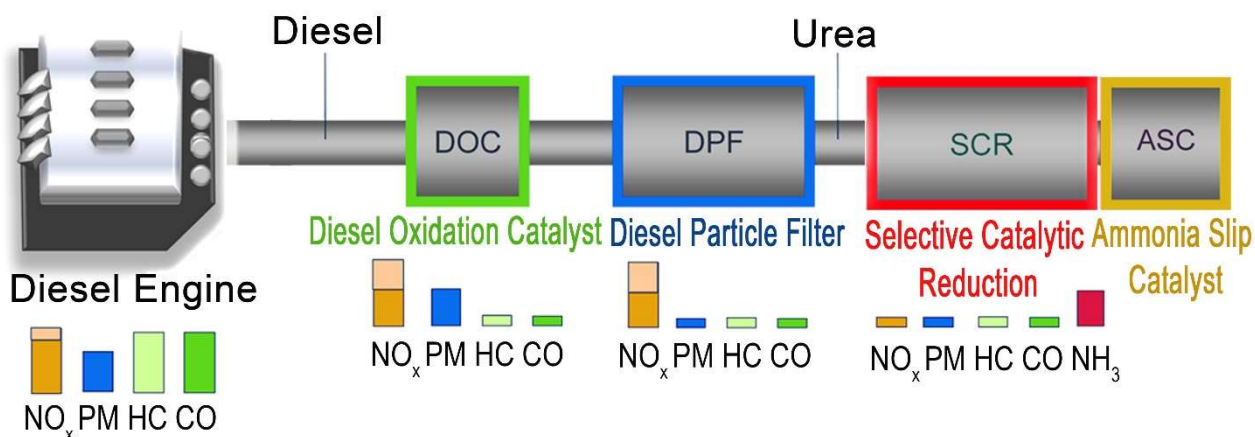
Fig. 23. Top: scheme of the different key components in a modern commercial SCR emission control system for diesel engines. Bottom: qualitative indication of the content of the different pollutants at the successive stages of the SCR emission control system.

In the DOC, hydrocarbons (HC) and CO are oxidized to CO_2. Some particulate matter (PM) and NO are oxidized as well. The heat produced in the DOC and the increased ratio of NO_2 to NO is beneficial for the effectiveness of the Cu-zeolite based SCR. The DPF effectively reduces the PM, but the trapped carbon particles need to be removed periodically by combustion, inducing very high temperature spikes which the downstream SCR catalyst needs to withstand. Just before the SCR component, urea is spray-dosed into the exhaust gas, where it decomposes to form NH_3 and CO_2. The urea dosing system is one of the most critical parts in the exhaust after-treatment system, since enough NH_3 needs to be added to convert all the NO_x, but a large excess should be avoided in order to reduce the NH_3 slip. In practice, a small excess of NH_3 is usually added which is handled by the ASC. The slip catalyst combines balanced amounts of an oxidation and a SCR component to oxidize part of the excess NH_3 to NO_x and the final mixture into H_2O and N_2.

More recent developments focus on intensification of the after-treatment system by combining DOC/DPF and SCR in a multifunctional catalytic body in order to improve the heat management and reduce the size/weight of the overall system.[208]

4.1.1. Market considerations. Despite the higher energy conversion efficiency of diesel versus gasoline engines, and the related potentially lower emissions of CO_2, diesel vehicles are still in the focus of the public debate.

This is mainly related to the inherent higher emissions of nitrogen oxides (NO_x) and PM for diesel engines compared to spark-ignition engines. The public debate was enlivened on the one hand by the fact that many of the diesel vehicles on our roads today are not equipped with the latest exhaust gas treatment technology and on the other hand by the deceptive practice of several car producers to reduce or circumvent the exhaust gas treatment under real driving conditions (as opposed to laboratory tests). Since the protection of air quality is however a priority to the European Commission (EC), stricter regulations and testing procedures are likely to be further implemented in the very near future. For example, and as a direct consequence of the so-called *Dieselgate*,[209] the EC introduced in September 2017 a modification of the *Euro 6* regulations, by a new test protocol for diesel passenger cars which mimics the RDE and uses portable emission measurement systems (PEMS). In November 2017, the EC proposed a revision of the "*Clean Vehicles Directive*" from 2009, which is expected to enter into force by September 2018.[210] The revised directive should deliver incentives to invest in fuel-efficient and low-emitting vehicles. Some regulations might even be adapted beforehand by individual states. This has recently happened in the case of the federal administrative court of Germany, which approved a ban on driving for diesel vehicles that are not conform with *Euro VI* standards, in case that the legal threshold values for NO_x and PM in the air are exceeded.[211] It is obviously very difficult to predict reliably the market for diesel vehicles in the short- and mid-term future. Clearly, the European vehicle market is moving towards zero emission and plug-in hybrid vehicles (based fully or partly on battery technology), but the share of these vehicles will probably not exceed 20% within the next two decades.[212] It is therefore expected that the short- and mid-term market (5-15 years ahead) for Cu-CHA catalysts is rapidly increasing due to the high demand.

4.2. Direct conversion of methane to methanol
Catalytic oxidations belong to the most important reactions in the current chemical industry, accounting for ~30% of the total world production in chemicals. One of the most challenging selective oxidation reactions is the one where methane is partially oxidized to methanol while at the same time avoiding complete oxidation to CO_2 and water. As all current routes for exploitation of methane rely on syngas as an intermediate, a low temperature activation and transformation of methane into methanol is commonly considered a dream reaction due to its enormous industrial potential. The direct conversion of MTM has attracted the attention of researchers in academia and industry for over

half a century and a multitude of homogeneous and heterogeneous catalytic systems have been explored. Despite significant advancement in selected cases,[213, 214] the inherent dilemma of not being able to achieve high conversion of methane and concurrent high methanol selectivity seems to persist in all cases.

As already mentioned in Section 3.2, the reaction over metal loaded zeolites, is currently carried out in a cyclic, *i.e.* non-catalytic way. It basically comprises three steps; i) oxidation; ii) methane loading; iii) steam assisted product release. Thus, these three steps involve different atmospheres, and also different temperatures. It is clear that such complex process operations cannot easily be realized on an industrial scale. This would, at the very minimum, involve non-standard (and expensive) engineering concepts such as employing a set of swing reactors cyclically exposed to different environments or circulating fluidized bed (CFB) technology.

On the other hand, the separation of the oxidation reaction (contact with gaseous oxygen) and the reaction of the substrate with an activated surface oxygen (in the absence of gaseous oxygen) might be the only feasible way of circumventing the above stated conversion-selectivity dilemma. In principle, one could envisage a CFB process similar to the rather recently developed technology known as chemical looping combustion (CLC), where a metal oxide is usually employed as oxygen carrier to combust a hydrocarbon fuel.[215]

At the lack of any process layout, not to mention process engineering data, but the one reported in the open literature where the reaction is performed stepwise in bench scale reactors, it is impossible to assess reliably the suitability of metal loaded zeolites for any kind of industrial process. In the following we therefore can only outline some general considerations for a chemical looping type of process.

The most important requirements for any oxygen carrier in a chemical looping process are a high oxygen capacity, fast up-take and release kinetics and both chemical and mechanical durability. The active oxygen capacity of metal loaded zeolites can be estimated from the best methanol yields reported in the literature. As mentioned in section 3.2, so far the highest productivity values for Cu-MOR and Cu-CHA samples are reported to be 170 and 132 $\mu mol_{MeOH}/g_{cat}$ (per cycle) respectively. The oxygen and methane up-take and methanol release kinetics have not been determined precisely, but the data from Pappas *et al.* (Fig. 21) indicates that oxygen activation is slow and the required methane contact time is high. Both parameters are therefore not in favor of a fast looping process and hence would negatively affect the overall productivity.

Moulijn *et al.*[216] have pointed out that for most processes encountered in oil refineries and chemical industry, the reaction rates are rarely less than 1 and seldom more than 10 $mol_{product}/m^3_{reactor}$ s. The catalytic productivity reported by Ipek and Lobo[30] of 55 $\mu mol/gh$ corresponds to 0.015 $mol_{product}/m^3_{reactor}$ s, assuming a reactor filling density of 1 g/cm^3. One can analyze the data reported for chemical looping in an analogous manner. For SSZ-13, the highest productivity reported so far is 132 $\mu mol/g$.[33] Aiming for a rate of 1 $mol_{product}/m^3_{reactor}$ s, one arrives at a target cycle time of ca. 2 min. One could imagine improvements in catalyst performance. Assuming a maximum Cu loading of 10 wt% and a maximum productivity of 0.5 mol_{MeOH}/mol_{Cu}, corresponding to a dimeric active site, a productivity close to 800 $\mu mol/g$ would be the maximum achievable. This would lead to a target cycle time of ca. 13 min, which one could compare to the total cycle time of ca. 20 h for the optimized protocol reported by Pappas *et al.*[33] Of course, many parameters such as very basic things like heat input and selectivities have not been considered here. However, these very simplified "back of the envelope" estimations do indicate that there is still some way to go.

It is clear that technology and catalyst development for a commercial MTM process are still in the fledgling stages. In addition, any new development will have to compete with one of the most mature processes in chemical industries, *i.e.* the syngas based large scale methanol synthesis. From a purely economic point of view it will therefore be difficult to justify the investment into a new technology. However, a driver for the development could be a changing legislation with respect to flaring of associated gas. So far, only legally non-binding agreements have been pursued, such as the "Zero

Routine Flaring by 2030" initiative, led by the world bank.[217] Compared to CO_2, methane is a much more powerful greenhouse gas and has a much shorter lifetime in the atmosphere. The possibility to selectively convert methane directly to higher value products, in particular for small scale applications, might therefore be a viable way to meet the short and long-term targets for climate change mitigation.

5. Conclusions and perspectives

The aim of this review was manifold: we wanted to provide the reader with a comprehensive overview on the structural complexity of Cu-CHA materials and show that despite this complexity it is possible to obtain a rather detailed picture of the Cu-speciation within the CHA topology by applying advanced characterization tools. The observed complexity can be rationalized by considering the interplay between chemical composition of the material and the chemical potential of the environment. Once one is equipped with this insight, it is possible to use the available functionalities of the material and obtain catalysts with unique properties. One of the most surprising observations is that the active state of the currently best low temperature NH_3-SCR catalyst is in fact so dynamic that it does not anymore fit into the classical definition of a heterogeneous catalyst, but should be considered a hybrid system, consisting of an active molecular entity that "lives in symbiosis" with an inorganic solid framework.

There are other prominent catalytic systems which show similar characteristics, like for example the industrial catalyst for sulfuric acid synthesis, which consists of a molecular molten active phase entrapped in a solid silica matrix.[218-220] That system exists as such for more than 60 years and is used to produce one of the largest bulk chemicals in the world and still we are far away from understanding the nature of its active sites.

When the reaction temperature is increased, the Cu-CHA system changes, as the mobile Cu-species lose their ligands and find docking sites at the internal walls of the zeolite framework. Now, the internal surface of the catalyst is covered with a range of less dynamic, but still highly active sites. Those sites are probably similar to the ones that are encountered in classical selective oxidation catalysts such as (mixed) oxides.

So, if we come back to the title of this review, we believe that Cu-CHA can indeed be considered a model system for applied redox catalysis. The activation of molecular oxygen is key to any selective oxidation reaction and the insight that we are able to obtain from the Cu-CHA system can be very useful to rationalize much more complex existing industrial systems. The ability to study in detail the fundamental steps of the redox-chemistry involved, might even allow to develop new concepts which are certainly needed to tackle some of the most urgent challenges related to energy conversion and climate change mitigation. The field is still new, further discoveries and improvements appear in the literature literally every month, and the underlying chemistry is fascinating.

Abbreviations

1Al Z	fraction of the zeolite framework characterized by only one Al in the proximity
2Al Z_2	fraction of the zeolite framework characterized by two Al in the proximity
4r	four-membered rings
6r	six-membered rings
8r	eight-membered rings
ALS	alternating least square
ASC	ammonia slip catalyst
CFB	circulating fluidized bed
CLC	chemical looping combustion
CHA	chabazite framework
CT	charge transfer
d6r	double six-membered ring
DFT	density functional theory

DOC	diesel oxidation catalyst
DPF	diesel particulate filter
DR	diffuse-reflectance
EC	European commission
EPR	election paramagnetic resonance
ESRF	European synchrotron radiation facility
EXAFS	X-ray absorption fine structure
FID	flame ionization detector
FTIR	Fourier-transform IR
FWHM	full width at half maximum
GC	gas chromatography
HA	harmonic approximation
HC	hydrocarbons
HERFD	high energy resolution fluorescence detected (XANES)
HF	high-frequency
ICP	inductively coupled plasma (mass spectrometry)
IR	infra-red
LCF	linear combination fit
LF	low-frequency
MAS NMR	magic angle spinning NMR
MCR	multivariate curve resolution
MD	molecular dynamics
MFI	ZSM-5 framework
MOR	mordenite framework
MS	mass spectrometry
MTM	methane to methanol
MTO	methanol into light olefins
NIR	near infra-red
NMR	nuclear magnetic resonance
PC	principal component
PCA	principal component analysis
P_{CO}	CO equilibrium pressure
PEMS	portable emission measurement systems
PMF	potentials of mean force
PMO	partial methane oxidation
P_{N2}	N_2 equilibrium pressure
P_{NO}	NO equilibrium pressure
PM	particulate matter
PXRD	powder X-ray diffraction
QHA	quasi harmonic approximation
RDE	real driving emissions
RT	room temperature
SAPO	silicon-aluminophosphate
SCR	selective catalytic reduction
TPR	temperature programmed desorption
UV-Vis	ultraviolet-visible
XANES	X-ray absorption near edge structure
XAS	X-ray absorption spectroscopy (both XANES and EXAFS)
XES	X-ray emission spectroscopy

Acknowledgements

References

1. L. S. Dent and J. V. Smith, *Nature*, 1958, **181**, 1794.
2. J. V. Smith, F. Rinaldi and L. S. D. Glasser, *Acta Cryst.*, 1963, **16**, 45.
3. J. J. Pluth, J. V. Smith and W. J. Mortier, *Mater. Res. Bull.*, 1977, **12**, 1001.
4. U.S. Patent US4544538 A, 1985.
5. B. M. Lok, C. A. Messina, R. L. Patton, R. T. Gajek, T. R. Cannan and E. M. Flanigen, *J. Am. Chem. Soc.*, 1984, **106**, 6092.
6. C. Andersen, M. Bremholm, P. Vennestrøm, A. Blichfeld, L. Lundegaard and I. B., *IUCrJ*, 2014, **1**, 382.
7. S. Bordiga, L. Regli, D. Cocina, C. Lamberti, M. Bjorgen and K. P. Lillerud, *J. Phys. Chem. B*, 2005, **109**, 2779.
8. S. Bordiga, L. Regli, C. Lamberti, A. Zecchina, M. Jorgen and K. P. Lillerud, *J. Phys. Chem. B*, 2005, **109**, 7724.
9. R. Martinez-Franco, M. Moliner, C. Franch, A. Kustov and A. Corma, *Appl. Catal. B-Environ.*, 2012, **127**, 273.
10. U. Olsbye, S. Svelle, M. Bjorgen, P. Beato, T. V. W. Janssens, F. Joensen, S. Bordiga and K. P. Lillerud, *Angew. Chem.-Int. Edit.*, 2012, **51**, 5810.
11. U. Olsbye, O. V. Saure, N. B. Muddada, S. Bordiga, C. Lamberti, M. H. Nilsen, K. P. Lillerud and S. Svelle, *Catal. Today*, 2011, **171**, 211.
12. A. Zecchina, S. Bordiga, J. G. Vitillo, G. Ricchiardi, C. Lamberti, G. Spoto, M. Bjorgen and K. P. Lillerud, *J. Am. Chem. Soc.*, 2005, **127**, 6361.
13. L. Regli, A. Zecchina, J. G. Vitillo, D. Cocina, G. Spoto, C. Lamberti, K. P. Lillerud, U. Olsbye and S. Bordiga, *Phys. Chem. Chem. Phys.*, 2005, **7**, 3197.
14. L. Regli, S. Bordiga, C. Busco, C. Prestipino, P. Ugliengo, A. Zecchina and C. Lamberti, *J. Am. Chem. Soc.*, 2007, **129**, 12131.
15. E. A. Eilertsen, S. Bordiga, C. Lamberti, A. Damin, F. Bonino, B. Arstad, S. Svelle, U. Olsbye and K. P. Lillerud, *ChemCatChem*, 2011, **3**, 1869.
16. J. H. Kwak, R. G. Tonkyn, D. H. Kim, J. Szanyi and C. H. F. Peden, *J. Catal.*, 2010, **275**, 187.
17. J. H. Kwak, D. Tran, S. D. Burton, J. Szanyi, J. H. Lee and C. H. F. Peden, *J. Catal.*, 2012, **287**, 203.
18. U. Deka, A. Juhin, E. A. Eilertsen, H. Emerich, M. A. Green, S. T. Korhonen, B. M. Weckhuysen and A. M. Beale, *J. Phys. Chem. C*, 2012, **116**, 4809.
19. J. Xue, X. Wang, G. Qi, J. Wang, M. Shen and W. Li, *J. Catal.*, 2013, **297**, 56.
20. F. Gao, E. D. Walter, E. M. Karp, J. Luo, R. G. Tonkyn, J. H. Kwak, J. Szanyi and C. H. F. Peden, *J. Catal.*, 2013, **300**, 20.
21. U. Deka, I. Lezcano-Gonzalez, B. M. Weckhuysen and A. M. Beale, *ACS Catal.*, 2013, **3**, 413.
22. D. E. Doronkin, M. Casapu, T. Gunter, O. Muller, R. Frahm and J. D. Grunwaldt, *J. Phys. Chem. C*, 2014, **118**, 10204.
23. A. M. Beale, F. Gao, I. Lezcano-Gonzalez, C. H. F. Peden and J. Szanyi, *Chem. Soc. Rev.*, 2015, **44**, 7371.
24. T. V. W. Janssens, H. Falsig, L. F. Lundegaard, P. N. R. Vennestrøm, S. B. Rasmussen, P. G. Moses, F. Giordanino, E. Borfecchia, K. A. Lomachenko, C. Lamberti, S. Bordiga, A. Godiksen, S. Mossin and P. Beato, *ACS Catal.*, 2015, **5**, 2832.
25. J. C. Wang, Z. L. Peng, Y. Chen, W. R. Bao, L. P. Chang and G. Feng, *Chem. Eng. J.*, 2015, **263**, 9.

26. M. Moreno-Gonzalez, A. E. Palomares, M. Chiesa, M. Boronat, E. Giamello and T. Blasco, *ACS Catal.*, 2017, **7**, 3501.
27. A. Marberger, A. W. Petrov, P. Steiger, M. Elsener, O. Krocher, M. Nachtegaal and D. Ferri, *Nat. Catal.*, 2018, **1**, 221.
28. M. J. Wulfers, S. Teketel, B. Ipek and R. F. Lobo, *Chem. Commun.*, 2015, **51**, 4447.
29. A. R. Kulkarni, Z. J. Zhao, S. Siahrostami, J. K. Norskov and F. Studt, *ACS Catal.*, 2016, **6**, 6531.
30. B. Ipek and R. F. Lobo, *Chem. Commun.*, 2016, **52**, 13401.
31. B. Ipek, M. J. Wulfers, H. Kim, F. Goltl, I. Hermans, J. P. Smith, K. S. Booksh, C. M. Brown and R. F. Lobo, *ACS Catal.*, 2017, **7**, 4291.
32. M. H. Mahyuddin, A. Staykov, Y. Shiota, M. Miyanishi and K. Yoshizawa, *ACS Catal.*, 2017, **7**, 3741.
33. D. K. Pappas, E. Borfecchia, M. Dyballa, I. A. Pankin, K. A. Lomachenko, A. Martini, M. Signorile, S. Teketel, B. Arstad, G. Berlier, C. Lamberti, S. Bordiga, U. Olsbye, K. P. Lillerud, S. Svelle and P. Beato, *J. Am. Chem. Soc.*, 2017, **139**, 14961.
34. M. B. Park, S. H. Ahn, A. Mansouri, M. Ranocchiari and J. A. van Bokhoven, *ChemCatChem*, 2017, **9**, 3705.
35. R. Oord, J. E. Schmidt and B. M. Weckhuysen, *Catal. Sci. Technol.*, 2018, **8**, 1028.
36. C. Paolucci, A. A. Verma, S. A. Bates, V. F. Kispersky, J. T. Miller, R. Gounder, W. N. Delgass, F. H. Ribeiro and W. F. Schneider, *Angew. Chem.-Int. Edit.*, 2014, **53**, 11828.
37. C. Tyrsted, E. Borfecchia, G. Berlier, K. A. Lomachenko, C. Lamberti, S. Bordiga, P. N. R. Vennestrom, T. V. W. Janssens, H. Falsig, P. Beato and A. Puig-Molina, *Catal. Sci. Technol.*, 2016, **6**, 8314.
38. J. H. Kwak, T. Varga, C. H. F. Peden, F. Gao, J. C. Hanson and J. Szanyi, *J. Catal.*, 2014, **314**, 83.
39. K. A. Lomachenko, E. Borfecchia, C. Negri, G. Berlier, C. Lamberti, P. Beato, H. Falsig and S. Bordiga, *J. Am. Chem. Soc.*, 2016, **138**, 12025.
40. K. A. Lomachenko, E. Borfecchia, S. Bordiga, A. V. Soldatov, P. Beato and C. Lamberti, *J. Phys.: Conf. Ser.*, 2016, **712**, 012041.
41. M. Thommes, K. Kaneko, A. V. Neimark, J. P. Olivier, F. Rodriguez-Reinoso, J. Rouquerol and K. S. W. Sing, *Pure Appl. Chem.*, 2015, **87**, 1051.
42. C. W. Andersen, E. Borfecchia, M. Bremholm, M. R. V. Jorgensen, P. N. R. Vennestrom, C. Lamberti, L. F. Lundegaard and B. B. Iversen, *Angew. Chem.-Int. Edit.*, 2017, **56**, 10367.
43. S. Bordiga, E. Groppo, G. Agostini, J. A. van Bokhoven and C. Lamberti, *Chem. Rev.*, 2013, **113**, 1736.
44. J. A. van Bokhoven and C. Lamberti, eds., *X-Ray Absorption and X-ray Emission Spectroscopy: Theory and Application*, John Wiley & Sons, Chichester (UK), 2016.
45. C. Lamberti, S. Bordiga, M. Salvalaggio, G. Spoto, A. Zecchina, F. Geobaldo, G. Vlaic and M. Bellatreccia, *J. Phys. Chem. B*, 1997, **101**, 344.
46. A. Zecchina, S. Bordiga, G. T. Palomino, D. Scarano, C. Lamberti and M. Salvalaggio, *J. Phys. Chem. B*, 1999, **103**, 3833.
47. Y. Kuroda, A. Itadani, R. Kumashiro, T. Fujimoto and M. Nagao, *Phys. Chem. Chem.Phys.*, 2004, **6**, 2534.
48. C. Lamberti, G. Spoto, D. Scarano, C. Pazé, M. Salvalaggio, S. Bordiga, A. Zecchina, G. T. Palomino and F. Dacapito, *Chem. Phys. Lett.*, 1997, **269**, 500.
49. C. Lamberti, S. Bordiga, A. Zecchina, M. Salvalaggio, F. Geobaldo and C. O. Arean, *J. Chem. Soc.-Faraday Trans.*, 1998, **94**, 1519.
50. C. Lamberti, G. T. Palomino, S. Bordiga, G. Berlier, F. D'Acapito and A. Zecchina, *Angew. Chem.-Int. Edit.*, 2000, **39**, 2138.
51. C. Prestipino, L. Capello, F. D'Acapito and C. Lamberti, *Phys. Chem. Chem. Phys.*, 2005, **7**, 1743.
52. S. T. Korhonen, D. W. Fickel, R. F. Lobo, B. M. Weckhuysen and A. M. Beale, *Chem. Commun.*, 2011, **47**, 800.
53. E. Borfecchia, K. A. Lomachenko, F. Giordanino, H. Falsig, P. Beato, A. V. Soldatov, S. Bordiga and C. Lamberti, *Chem. Sci.*, 2015, **6**, 548.
54. M. Anpo, M. Matsuoka, Y. Shioya, H. Yamashita, E. Giamello, C. Morterra, M. Che, H. H. Patterson, S. Webber, S. Ouellette and M. A. Fox, *J. Phys. Chem.*, 1994, **98**, 5744.
55. C. Garino, E. Borfecchia, R. Gobetto, L. Salassa, J. A. van Bokhoven and C. Lamberti, *Coord. Chem. Rev.*, 2014, **277–278** 130.
56. J. Singh, C. Lamberti and J. A. van Bokhoven, *Chem. Soc. Rev.*, 2010, **39**, 4754.
57. E. I. Solomon, D. E. Heppner, E. M. Johnston, J. W. Ginsbach, J. Cirera, M. Qayyum, M. T. Kieber-Emmons, C. H. Kjaergaard, R. G. Hadt and L. Tian, *Chem. Rev.*, 2014, **114**, 3659.
58. F. Giordanino, E. Borfecchia, K. A. Lomachenko, A. Lazzarini, G. Agostini, E. Gallo, A. V. Soldatov, P. Beato, S. Bordiga and C. Lamberti, *J. Phys. Chem. Lett.*, 2014, **5**, 1552.
59. A. Martini, E. Borfecchia, K. A. Lomachenko, I. A. Pankin, C. Negri, G. Berlier, P. Beato, H. Falsig, S. Bordiga and C. Lamberti, *Chem. Sci.*, 2017, **8**, 6836.
60. J. A. van Bokhoven and C. Lamberti, in *XAFS Techniques for Catalysts, Nanomaterials, and Surfaces*, eds. Y. Yasuhiro Iwasawa, K. Asakura and M. Tada, Springer, Switzerland, 2017, ch. 20, pp. 299.
61. C. Lamberti, E. Groppo, G. Spoto, S. Bordiga and A. Zecchina, *Adv. Catal.*, 2007, **51**, 1.
62. A. Vimont, F. Thibault-Starzyk and M. Daturi, *Chem. Soc. Rev.*, 2010, **39**, 4928.
63. S. Bordiga, C. Lamberti, F. Bonino, A. Travert and F. Thibault-Starzyk, *Chem. Soc. Rev.*, 2015, **44**, 7262.

64. C. Lamberti, A. Zecchina, E. Groppo and S. Bordiga, *Chem. Soc. Rev.*, 2010, **39**, 4951.
65. F. Giordanino, P. N. R. Vennestrom, L. F. Lundegaard, F. N. Stappen, S. L. Mossin, P. Beato, S. Bordiga and C. Lamberti, *Dalton Trans.*, 2013, **42**, 12741.
66. G. Spoto, E. Gribov, S. Bordiga, C. Lamberti, G. Ricchiardi, D. Scarano and A. Zecchina, *Chem. Comm.*, 2004, **23**, 2768.
67. S. Bordiga, C. Pazé, G. Berlier, D. Scarano, G. Spoto, A. Zecchina and C. Lamberti, *Catal. Today*, 2001, **70**, 91.
68. G. Ricchiardi, A. Damin, S. Bordiga, C. Lamberti, G. Spano, F. Rivetti and A. Zecchina, *J. Am. Chem. Soc.*, 2001, **123**, 11409.
69. S. Bordiga, A. Damin, F. Bonino, G. Ricchiardi, C. Lamberti and A. Zecchina, *Angew. Chem.-Int. Edit.*, 2002, **41**, 4734.
70. S. Bordiga, A. Damin, F. Bonino, G. Ricchiardi, A. Zecchina, R. Tagliapietra and C. Lamberti, *Phys. Chem. Chem. Phys.*, 2003, **5**, 4390.
71. A. Damin, F. Bonino, S. Bordiga, E. Groppo, C. Lamberti and A. Zecchina, *ChemPhysChem*, 2006, **7**, 342.
72. J. S. Woertink, P. J. Smeets, M. H. Groothaert, M. A. Vance, B. F. Sels, R. A. Schoonheydt and E. I. Solomon, *P. Natl. Acad. Sci. USA.*, 2009, **106**, 18908.
73. P. J. Smeets, R. G. Hadt, J. S. Woertink, P. Vanelderen, R. A. Schoonheydt, B. F. Sels and E. I. Solomon, *J. Am. Chem. Soc.*, 2010, **132**, 14736.
74. E. Borfecchia, A. Amedjkouh, M. Dyballa, D. K. Pappas, G. Berlier, V. G. H. Eijsink, Å. R. Kjendseth, C. Lamberti, K. L. Lillerud, S. Svelle, S. Bordiga, M. Sørlie and U. Olsbye, *ACS Catal.*, submitted.
75. C. Paolucci, A. A. Parekh, I. Khurana, J. R. Di Iorio, H. Li, J. D. Albarracin Caballero, A. J. Shih, T. Anggara, W. N. Delgass, J. T. Miller, F. H. Ribeiro, R. Gounder and W. F. Schneider, *J. Am. Chem. Soc.*, 2016, **138**, 6028.
76. C. Paolucci, J. R. Di Iorio, F. H. Ribeiro, R. Gounder and W. F. Schneider, in *Advances in Catalysis*, ed. C. Song, Academic Press, 2016, vol. 59, pp. 1.
77. C. Paolucci, I. Khurana, A. A. Parekh, S. C. Li, A. J. Shih, H. Li, J. R. Di Iorio, J. D. Albarracin-Caballero, A. Yezerets, J. T. Miller, W. N. Delgass, F. H. Ribeiro, W. F. Schneider and R. Gounder, *Science*, 2017, **357**, 898.
78. H. Falsig, P. N. R. Vennestrøm, P. G. Moses and T. V. W. Janssens, *Top. Catal.*, 2016, **59**, 861.
79. L. Chen, H. Falsig, T. V. W. Janssens and H. Gronbeck, *J. Catal.*, 2018, **358**, 179.
80. H. Li, C. Paolucci and W. F. Schneider, *J. Chem. Theory Comput.*, 2018, **14**, 929.
81. E. Giamello, D. Murphy, G. Magnacca, C. Morterra, Y. Shioya, T. Nomura and M. Anpo, *J. Catal.*, 1992, **136**, 510.
82. M. Lo Jacono, G. Fierro, R. Dragone, X. B. Feng, J. dItri and W. K. Hall, *J. Phys. Chem. B*, 1997, **101**, 1979.
83. G. T. Palomino, P. Fisicaro, S. Bordiga, A. Zecchina, E. Giamello and C. Lamberti, *J. Phys. Chem. B*, 2000, **104**, 4064.
84. F. Xamena, P. Fisicaro, G. Berlier, A. Zecchina, G. T. Palomino, C. Prestipino, S. Bordiga, E. Giamello and C. Lamberti, *J. Phys. Chem. B*, 2003, **107**, 7036.
85. P. J. Smeets, J. S. Woertink, B. F. Sels, E. I. Solomon and R. A. Schoonheydt, *Inorg. Chem.*, 2010, **49**, 3573.
86. A. Godiksen, F. N. Stappen, P. N. R. Vennestrom, F. Giordanino, S. B. Rasmussen, L. F. Lundegaard and S. Mossin, *J. Phys. Chem. C*, 2014, **118**, 23126.
87. A. Godiksen, P. Vennestrom, S. Rasmussen and S. Mossin, *Top. Catal.*, 2017, **60**, 13.
88. A. Godiksen, O. L. Isaksen, S. B. Rasmussen, P. N. R. Vennestrom and S. Mossin, *ChemCatChem*, 2018, **10**, 366.
89. Z. Sojka, M. Che and E. Giamello, *J. Phys. Chem. B*, 1997, **101**, 4831.
90. J. Song, Y. L. Wang, E. D. Walter, N. M. Washton, D. H. Mei, L. Kovarik, M. H. Engelhard, S. Prodinger, Y. Wang, C. H. F. Peden and F. Gao, *ACS Catal.*, 2017, **7**, 8214.
91. Z. C. Zhao, R. Yu, R. R. Zhao, C. Shi, H. Gies, F. S. Xiao, D. De Vos, T. Yokoi, X. H. Bao, U. Kolb, M. Feyen, R. McGuire, S. Maurer, A. Moini, U. Muller and W. P. Zhang, *Appl. Catal. B-Environ.*, 2017, **217**, 421.
92. M. Moreno-Gonzalez, B. Hueso, M. Boronat, T. Blasco and A. Corma, *J. Phys. Chem. Lett.*, 2015, **6**, 1011.
93. D. W. Fickel, J. M. Fedeyko and R. F. Lobo, *J. Phys. Chem. C*, 2010, **114**, 1633.
94. F. Gao and C. H. F. Peden, *Catalysts* 2018, **8**, 140.
95. J. R. Di Iorio and R. Gounder, *Chem. Mat.*, 2016, **28**, 2236.
96. J. Dedecek, V. Balgova, V. Pashkova, P. Klein and B. Wichterlova, *Chem. Mat.*, 2012, **24**, 3231.
97. J. Dedecek, Z. Sobalik and B. Wichterlova, *Catal. Rev.: Sci. Eng.*, 2012, **54**, 135.
98. J. Dedecek, D. Kaucky, B. Wichterlova and O. Gonsiorova, *Phys. Chem. Chem. Phys.*, 2002, **4**, 5406.
99. J. R. Di Iorio, C. T. Nimlos and R. Gounder, *ACS Catal.*, 2017, **7**, 6663.
100. W. Löwenstein, *Am. Mineral.*, 1954, **39**, 92.
101. J. M. Thomas, *Chem.-Eur. J.*, 1997, **3**, 1557.
102. M. Iwamoto, H. Yahiro, Y. Torikai, T. Yoshioka and N. Mizuno, *Chem. Lett.*, 1990, 1967.
103. Y. J. Li and W. K. Hall, *J. Phys. Chem.*, 1990, **94**, 6145.
104. M. Iwamoto, H. Yahiro, K. Tanda, N. Mizuno, Y. Mine and S. Kagawa, *J. Phys. Chem.*, 1991, **95**, 3727.
105. Y. J. Li and W. K. Hall, *J. Catal.*, 1991, **129**, 202.
106. S. Sato, Y. Yoshihiro, H. Yahiro, N. Mizuno and M. Iwamoto, *Appl. Catal.*, 1991, **70**, L1.
107. M. Iwamoto, H. Yahiro, N. Mizuno, W. X. Zhang, Y. Mine, H. Furukawa and S. Kagawa, *J. Phys. Chem.*, 1992, **96**, 9360.
108. M. Shelef, *Chem. Rev.*, 1995, **95**, 209.

109. G. Spoto, A. Zecchina, S. Bordiga, G. Ricchiardi, G. Martra, G. Leofanti and G. Petrini, *Appl. Catal. B-Environ.*, 1994, **3**, 151.
110. G. T. Palomino, S. Bordiga, A. Zecchina, G. L. Marra and C. Lamberti, *J. Phys. Chem. B*, 2000, **104**, 8641.
111. V. Bolis, S. Maggiorini, L. Meda, F. D'Acapito, G. T. Palomino, S. Bordiga and C. Lamberti, *J. Chem. Phys.*, 2000, **113**, 9248.
112. C. Prestipino, G. Berlier, F. Xamena, G. Spoto, S. Bordiga, A. Zecchina, G. T. Palomino, T. Yamamoto and C. Lamberti, *Chem. Phys. Lett.*, 2002, **363**, 389.
113. Y. Kuroda, K. Yagi, N. Horiguchi, Y. Yoshikawa, R. Kumashiro and M. Nagao, *Phys. Chem. Chem. Phys.*, 2003, **5**, 3318.
114. Z. Li, K. C. Xie and R. C. T. Slade, *Appl. Catal. A-Gen.*, 2001, **209**, 107.
115. Y. H. Zhang, I. J. Drake, D. N. Briggs and A. T. Bell, *J. Catal.*, 2006, **244**, 219.
116. Y. H. Zhang, I. J. Drake and A. T. Bell, *Chem. Mater.*, 2006, **18**, 2347.
117. J. Sárkány, J. d'Itri and W. H. Sachtler, *Catal. Lett.*, 1992, **16**, 241.
118. J. Valyon and W. K. Hall, *J. Phys. Chem.*, 1993, **97**, 7054.
119. S. C. Larsen, A. Aylor, A. T. Bell and J. A. Reimer, *J. Phys. Chem.*, 1994, **98**, 11533.
120. Y. Kuroda, Y. Yoshikawa, S. Konno, H. Hamano, H. Maeda, R. Kumashiro and M. Nagao, *J. Phys. Chem.*, 1995, **99**, 10621.
121. H. J. Jong, W. K. Hall and J. L. d'Itri, *J. Phys. Chem.*, 1996, **100**, 9416.
122. D. Nachtigallova, P. Nachtigall and J. Sauer, *Phys. Chem. Chem. Phys.*, 2001, **3**, 1552.
123. T. Cheung, S. K. Bhargava, M. Hobday and K. Foger, *J. Catal.*, 1996, **158**, 301.
124. H. J. Jang, W. K. Hall and J. dItri, *J. Phys. Chem.*, 1996, **100**, 9416.
125. J. Szanyi, J. H. Kwak, H. Zhu and C. H. F. Peden, *Phys. Chem. Chem. Phys.* , 2013, **15**, 2368.
126. A. Zecchina, S. Bordiga, G. Spoto, L. Marchese, G. Petrini, G. Leofanti and M. Padovan, *J. Phys. Chem.*, 1992, **96**, 4991.
127. A. Zecchina, S. Bordiga, G. Spoto, D. Scarano, G. Petrini, G. Leofanti, M. Padovan and C. O. Arean, *J. Chem. Soc.-Faraday Trans.*, 1992, **88**, 2959.
128. S. Bordiga, I. Roggero, P. Ugliengo, A. Zecchina, V. Bolis, G. Artioli, R. Buzzoni, G. Marra, F. Rivetti, G. Spano and C. Lamberti, *J. Chem. Soc., Dalton Trans.*, 2000, 3921.
129. I. Lezcano-Gonzalez, U. Deka, B. Arstad, A. Van Yperen-De Deyne, K. Hemelsoet, M. Waroquier, V. Van Speybroeck, B. M. Weckhuysen and A. M. Beale, *Phys. Chem. Chem. Phys.*, 2014, **16**, 1639.
130. A. Zecchina, D. Scarano, S. Bordiga, G. Spoto and C. Lamberti, *Adv. Catal.*, 2001, **46**, 265.
131. K. I. Hadjiivanov and G. N. Vayssilov, *Adv. Catal.*, 2002, **47**, 307.
132. V. Bolis, A. Barbaglia, S. Bordiga, C. Lamberti and A. Zecchina, *J. Phys. Chem. B*, 2004, **108**, 9970.
133. A. Zecchina, S. Bordiga, M. Salvalaggio, G. Spoto, D. Scarano and C. Lamberti, *J. Catal.*, 1998, **173**, 540.
134. G. T. Palomino, E. Giamello, P. Fisicaro, S. Bordiga, C. Lamberti and A. Zecchina, *Stud. Surf. Sci. Catal.*, 2000, **130**, 2915.
135. S. Bordiga, D. Scarano, G. Spoto, A. Zecchina, C. Lamberti and C. O. Arean, *Vib. Spectrosc.*, 1993, **5**, 69.
136. S. Bordiga, E. Escalona Platero, C. Otero Areán, C. Lamberti and A. Zecchina, *J. Catal.*, 1992, **137**, 179.
137. C. Lamberti, C. Morterra, S. Bordiga, G. Cerrato and D. Scarano, *Vib. Spectrosc.*, 1993, **4**, 273.
138. C. Prestipino, L. Regli, J. G. Vitillo, F. Bonino, A. Damin, C. Lamberti, A. Zecchina, P. L. Solari, K. O. Kongshaug and S. Bordiga, *Chem. Mater.*, 2006, **18**, 1337.
139. F. X. Llabrés i Xamena, P. Fisicaro, G. Berlier, A. Zecchina, G. T. Palomino, C. Prestipino, S. Bordiga, E. Giamello and C. Lamberti, *J. Phys. Chem. B*, 2003, **107**, 7036.
140. G. Leofanti, A. Marsella, B. Cremaschi, M. Garilli, A. Zecchina, G. Spoto, S. Bordiga, P. Fisicaro, G. Berlier, C. Prestipino, G. Casali and C. Lamberti, *J. Catal.*, 2001, **202**, 279.
141. J. H. Kwak, H. Y. Zhu, J. H. Lee, C. H. F. Peden and J. Szanyi, *Chem. Comm.*, 2012, **48**, 4758.
142. E. I. Solomon, J. W. Ginsbach, D. E. Heppner, M. T. Kieber-Emmons, C. H. Kjaergaard, P. J. Smeets, L. Tian and J. S. Woertink, *Faraday Discuss.*, 2011, **148**, 11.
143. P. Vanelderen, R. G. Hadt, P. J. Smeets, E. I. Solomon, R. A. Schoonheydt and B. F. Sels, *J. Catal.*, 2011, **284**, 157.
144. W. van Beek, O. V. Safonova, G. Wiker and H. Emerich, *Phase Transit.*, 2011, **84**, 726.
145. P. M. Abdala, O. V. Safonova, G. Wiker, W. van Beek, H. Emerich, J. A. van Bokhoven, J. Sa, J. Szlachetko and M. Nachtegaal, *Chimia*, 2012, **66**, 699.
146. A. L. Bugaev, A. A. Guda, K. A. Lomachenko, V. V. Shapovalov, A. Lazzarini, J. G. Vitillo, L. A. Bugaev, E. Groppo, R. Pellegrini, A. V. Soldatov, J. A. van Bokhoven and C. Lamberti, *J. Phys. Chem. C*, 2017, **121**, 18202.
147. A. L. Bugaev, A. A. Guda, K. A. Lomachenko, E. G. Kamyshova, M. A. Soldatov, G. Kaur, S. Oien-Odegaard, L. Braglia, A. Lazzarini, M. Manzoli, S. Bordiga, U. Olsbye, K. P. Lillerud, A. V. Soldatov and C. Lamberti, *Faraday Discuss.*, 2018, doi: 10.1039/C7FD00224F.
148. F. Gao, N. M. Washton, Y. L. Wang, M. Kollar, J. Szanyi and C. H. F. Peden, *J. Catal.*, 2015, **331**, 25.
149. B. R. Goodman, K. C. Hass, W. F. Schneider and J. B. Adams, *Catal. Lett.*, 2000, **68**, 85.
150. W. Loewenstein, *Am. Mineral.*, 1954, **39**, 92.
151. S. A. Bates, A. A. Verma, C. Paolucci, A. A. Parekh, T. Anggara, A. Yezerets, W. F. Schneider, J. T. Miller, W. N. Delgass and F. H. Ribeiro, *J. Catal.*, 2014, **312**, 87.

152. M. Sierka and J. Sauer, *J. Phys. Chem. B*, 2001, **105**, 1603.
153. J. Jaumot, R. Gargallo, A. de Juan and R. Tauler, *Chemometrics Intell. Lab. Syst.*, 2005, **76**, 101.
154. A. de Juan, J. Jaumot and R. A. Tauler, *Anal. Methods*, 2014, **6**, 4964.
155. J. Jaumot, A. de Juan and R. Tauler, *Chemometr. Intell. Lab.*, 2015, **140**, 1.
156. J. S. McEwen, T. Anggara, W. F. Schneider, V. F. Kispersky, J. T. Miller, W. N. Delgass and F. H. Ribeiro, *Catal. Today*, 2012, **184**, 129.
157. J. Děděček, B. Wichterlova and P. Kubat, *Micr. Mesop. Mater.*, 1999, **32**, 63.
158. G. Busca, *Phys. Chem. Chem. Phys.*, 1999, **1**, 723.
159. R. Q. Zhang, J. S. McEwen, M. Kollar, F. Gao, Y. L. Wang, J. Szanyi and C. H. F. Peden, *ACS Catal.*, 2014, **4**, 4093.
160. J. Y. Luo, F. Gao, K. Kamasamudram, N. Currier, C. H. F. Peden and A. Yezerets, *J. Catal.*, 2017, **348**, 291.
161. F. Gao, E. D. Walter, M. Kollar, Y. Wang, J. Szanyi and C. H. F. Peden, *J. Catal.*, 2014, **319**, 1.
162. Q. Guo, F. Fan, D. A. J. M. Ligthart, G. Li, Z. Feng, E. J. M. Hensen and C. Li, *ChemCatChem*, 2014, **6**, 634.
163. A. Martini, E. Alladio and E. Borfecchia, *Top. Catal.*, accepted.
164. M. H. Groothaert, P. J. Smeets, B. F. Sels, P. A. Jacobs and R. A. Schoonheydt, *J. Am. Chem. Soc.*, 2005, **127**, 1394.
165. P. J. Smeets, M. H. Groothaert and R. A. Schoonheydt, *Catal. Today*, 2005, **110**, 303.
166. P. Vanelderen, J. Vancauwenbergh, B. F. Sels and R. A. Schoonheydt, *Coord. Chem. Rev.*, 2013, **257**, 483.
167. S. Grundner, M. A. C. Markovits, G. Li, M. Tromp, E. A. Pidko, E. J. M. Hensen, A. Jentys, M. Sanchez-Sanchez and J. A. Lercher, *Nat. Commun.*, 2015, **6**.
168. M. Inomata, A. Miyamoto and Y. Murakami, *J. Catal.*, 1980, **62**, 140.
169. G. T. Went, L. J. Leu, R. R. Rosin and A. T. Bell, *J. Catal.*, 1992, **134**, 492.
170. N. Y. Topsoe, *Science*, 1994, **265**, 1217.
171. N. Y. Topsoe, J. A. Dumesic and H. Topsoe, *J. Catal.*, 1995, **151**, 241.
172. N. Y. Topsoe, H. Topsoe and J. A. Dumesic, *J. Catal.*, 1995, **151**, 226.
173. G. Busca, L. Lietti, G. Ramis and F. Berti, *Appl. Catal. B-Environ.*, 1998, **18**, 1.
174. B. M. Weckhuysen and D. E. Keller, *Catal. Today*, 2003, **78**, 25.
175. M. Calatayud, B. Mguig and C. Minot, *Surf. Sci. Rep.*, 2004, **55**, 169.
176. P. Granger and V. I. Parvulescu, *Chem. Rev.*, 2011, **111**, 3155.
177. M. Koebel, M. Elsener and M. Kleemann, *Catal. Today*, 2000, **59**, 335.
178. P. L. T. Gabrielsson, *Top. Catal.*, 2004, **28**, 177.
179. K. Rahkamaa-Tolonen, T. Maunula, M. Lomma, M. Huuhtanen and R. L. Keiski, *Catal. Today*, 2005, **100**, 217.
180. A. Zecchina, M. Rivallan, G. Berlier, C. Lamberti and G. Ricchiardi, *Phys. Chem. Chem. Phys.*, 2007, **9**, 3483.
181. M. Moliner, C. Franch, E. Palomares, M. Grill and A. Corma, *Chem. Commun.*, 2012, **48**, 8264.
182. J. Li, H. Chang, L. Ma, J. Hao and R. T. Yang, *Catal. Today*, 2011, **175**, 147.
183. M. Stanciulescu, G. Caravaggio, A. Dobri, J. Moir, R. Burich, J. P. Charland and P. Bulsink, *Appl. Catal. B: Environ.*, 2012, **123-124**, 229.
184. R. D. Zhang, N. Liu, Z. G. Lei and B. H. Chen, *Chem. Rev.*, 2016, **116**, 3658.
185. S. Brandenberger, O. Krocher, A. Tissler and R. Althoff, *Catal. Rev.*, 2008, **50**, 492.
186. J. Carlsson and J. Aqvist, *J. Phys. Chem. B*, 2005, **109**, 6448.
187. I. Andricioaei and M. Karplus, *J. Chem. Phys.*, 2001, **115**, 6289.
188. K. Alexopoulos, M. S. Lee, Y. Liu, Y. C. Zhi, Y. S. Liu, M. F. Reyniers, G. B. Marin, V. A. Glezakou, R. Rousseau and J. A. Lercher, *J. Phys. Chem. C*, 2016, **120**, 7172.
189. D. Frenkel and B. Smit, in *Understanding Molecular Simulation (Second Edition)*, eds. D. Frenkel and B. Smit, Academic Press, San Diego, 2002, pp. 167.
190. C. J. Cramer, *Essentials of Computational Chemistry: Theories and Models, 2nd Ed.*, John Wiley and Sons,, Chichester, 2004.
191. M. Nielsen, R. Y. Brogaard, H. Falsig, P. Beato, O. Swang and S. Svelle, *ACS Catal.*, 2015, **5**, 7131.
192. F. Göltl, P. Sautet and I. Hermans, *Catal. Today*, 2016, **267**, 41.
193. M. Ravi, M. Ranocchiari and J. A. van Bokhoven, *Angew. Chem.-Int. Edit.*, 2017, **56**, 16464.
194. V. L. Sushkevich, D. Palagin, M. Ranocchiari and J. A. van Bokhoven, *Science*, 2017, **356**, 523.
195. P. Tomkins, M. Ranocchiari and J. A. van Bokhoven, *Accounts Chem. Res.*, 2017, **50**, 418.
196. K. Narsimhan, K. Iyoki, K. Dinh and Y. Roman-Leshkov, *ACS Central Sci.*, 2016, **2**, 424.
197. S. Grundner, W. Luo, M. Sanchez-Sanchez and J. A. Lercher, *Chem. Commun.*, 2016, **52**, 2553.
198. H. V. Le, S. Parishan, A. Sagaltchik, C. Gobel, C. Schlesiger, W. Malzer, A. Trunschke, R. Schomacker and A. Thomas, *ACS Catal.*, 2017, **7**, 1403.
199. M. A. C. Markovits, A. Jentys, M. Tromp, M. Sanchez-Sanchez and J. A. Lercher, *Top. Catal.*, 2016, **59**, 1554.
200. F. Gao, D. Mei, Y. Wang, J. Szanyi and C. H. F. Peden, *J. Am. Chem. Soc.*, 2017, **139**, 4935.
201. S. E. Bozbag, E. M. C. Alayon, J. Pechacek, M. Nachtegaal, M. Ranocchiari and J. A. van Bokhoven, *Catal. Sci. Technol.*, 2016, **6**, 5011.
202. T. Sheppard, C. D. Hamill, A. Goguet, D. W. Rooney and J. M. Thompson, *Chem. Commun.*, 2014, **50**, 11053.
203. P. Vanelderen, P. J. Smeets, R. G. Hadt, J. S. Woertink, R. A. Schoonheydt, B. F. Sels and E. I. Solomon, *Abstr. Pap. Am. Chem. Soc.*, 2011, **242**.

204. E. M. Alayon, M. Nachtegaal, M. Ranocchiari and J. A. van Bokhoven, *Chem. Comm.*, 2012, **48**, 404.

205. E. M. C. Alayon, M. Nachtegaal, A. Bodi and J. A. van Bokhoven, *ACS Catal.*, 2014, **4**, 16.

206. E. M. C. Alayon, M. Nachtegaal, A. Bodi, M. Ranocchiari and J. A. van Bokhoven, *Phys. Chem. Chem. Phys.*, 2015, **17**, 7681.

207. V. Franco, F. P. Sánchez, J. German and P. Mock, *"Real-World Exhaust Emissions from Modern Diesel Cars. White paper from October ICCT*, International Council on Clean Transportation (ICCT), Beijing, 2014 Downloadable at: https://www.theicct.org/publications/real-world-exhaust-emissions-modern-diesel-cars.

208. A. Kufferath, M. Krüger, D. Dirk Naber, E. Mailänder and R. Maier, *The Path to a Negligible NO_2 Immission Contribution from the Diesel Powertrain*, presented at the 39th international Motor Symposium, Vienna April 26-27, 2018. Manuscript downloadable at http://www.autonews.com/article/20180426/BLOG06/180429820/for-bosch-diesel-claim-technical-details-to-come.

209. M. Horn, C. Grundler and P. Brooks, *(witnesses), Hearing on "Volkswagen's Emissions Cheating Allegations: Initial Questions". U.S House of Representatives Committee on Energy and Commerce*, October 6, 2015, downloadable at : https://docs.house.gov/meetings/IF/IF02/20151008/104046/HHRG.

210. *EU Clean Vehicles Directive*, downloadable at https://ec.europa.eu/transport/themes/urban/vehicles/directive_en.

211. *Press release of the Federal Administrative Court of Germany from February, 22, 2018, (in German)*, accessible at http://www.bverwg.de/pm/2018/9.

212. in *High Level Group GEAR 2030 report on automotive competitiveness and sustainability (downloadable at: https://ec.europa.eu/growth/content/high-level-group-gear-2030-report-on-automotive-competitiveness-and-sustainability_de)*, 18/10/2017.

213. R. A. Periana, D. J. Taube, S. Gamble, H. Taube, T. Satoh and H. Fujii, *Science*, 1998, **280**, 560.

214. R. Palkovits, C. von Malotki, M. Baumgarten, K. Mullen, C. Baltes, M. Antonietti, P. Kuhn, J. Weber, A. Thomas and F. Schuth, *ChemSusChem*, 2010, **3**, 277.

215. A. Lyngfelt and B. Leckner, *Appl. Energy*, 2015, **157**, 475.

216. J. A. Moulijn, M. Makkee and A. E. Van Diepen, *Chemical Process Technology, 2nd Ed.*, John Wiley, Hoboken, 2013.

217. The world bank, *Zero Routine Flaring by 2030*, available at: http://www.worldbank.org/en/programs/zero.

218. H. Livbjerg, K. F. Jensen and J. Villadsen, *J. Catal.*, 1976, **45**, 216.

219. B. S. Balzhinimaev, A. A. Ivanov, O. B. Lapina, V. M. Mastikhin and K. I. Zamaraev, *Faraday Discuss.*, 1989, **87**, 133.

220. F. Cavalca, P. Beato, J. Hyldtoft, K. Christensen and S. Helveg, *J. Phys. Chem. C*, 2017, **121**, 3350.